

# **A new approach to stellar image correction for atmospherically degraded images**

Thesis submitted for the Degree of Doctor of Philosophy  
In the Faculty of Engineering

Bangalore University

By

V. Chinnappan

Guides

Dr. A. K. Saxena  
Dean, Faculty of Sciences (Engineering)  
Indian Institute of Astrophysics

And

Dr. A. Sreenivasan  
Former Principal, BMS College of Engineering  
Bangalore

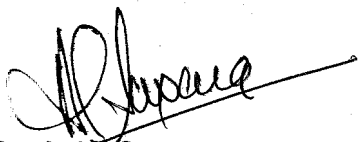
Bangalore University  
August, 2006

# DECLARATION

The matter contained in this thesis is the result of the investigations carried out by Mr. V. Chinnappan at the Department of Electronics, Bangalore University, Bangalore-1 and at Indian institute of Astrophysics, Bangalore-34 under our guidance and supervision.

This work has not been submitted for the award of any degree, diploma, associateship, fellowship, etc. of any university or other Institute.

Guides



Dr. A. K. Saxena  
Dean, Faculty of Sciences (Engineering),  
Indian Institute of Astrophysics,  
Koramangala  
Bangalore – 34.

**Dr. A.K. Saxena**  
**Dean Engineering**  
**Indian Institute of Astrophysics**  
**(Ministry of Science & Technology)**  
**Govt. of India**  
**Bangalore - 560 034**

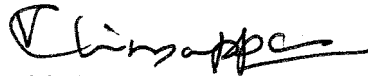


Dr. A. Sreenivasan  
Former Principal,  
BMS college of  
Engineering,  
YELLAMMA DASAPPA  
INSTITUTE OF TECHNOLOGY  
KANAKAPURA ROAD  
BANGALORE-560 062

## DECLARATION

I, hereby declare that the matter contained in this thesis is the result of the investigations carried out by me at Indian institute of Astrophysics, Bangalore-34 and at the Department of Electronics, Bangalore University, Bangalore-1 under the guidance and supervision of Dr. A. K. Saxena, Dean, Faculty of Engineering, Indian Institute of Astrophysics, Bangalore and Dr. A. Sreenivasan, Former Principal, BMS college of Engineering, Bangalore.

This work has not been submitted for the award of any degree, diploma, associateship, fellowship, etc. of any university or other Institute



V. Chinnappan

Principal Scientific Officer  
Indian Institute of Astrophysics  
Bangalore-34

## ABSTRACT

Atmospheric turbulence is the main cause of image degradation and poor resolution at the focal plane of a perfectly made optical telescope. It is necessary to make corrective measures to improve the optical wave-front, thus, get improved resolution from the telescopes. This research work is an effort to understand the degradations caused by atmospheric turbulence, build an appropriate wave-front sensor to measure the errors in the wave-front and correct the wave-front in real time for our 2.34 M Vainu Bappu Telescope (VBT) at Vainu Bappu Observatory, Kavalur, keeping the cost as one of the main factors.

To estimate the atmospheric degradation on astronomical images, Fried's parameter,  $r_0$  was measured with a new experimental method using speckle interferometer at VBT. Based on this measurement, essential parameters for correction were arrived. The costs involved in a real time correction experiments are very high and hence, alternative low cost methods were developed. Avalanche photodiodes-based wave-front sensors are being used as sensor of choice for their low noise and high speed of operation. Recent research has confirmed that specially designed CCDs can achieve the same performance at a fraction of cost. One drawback of CCD is its serial readout architecture, limiting the speed of operation. New imaging detectors based on CMOS imagers have random access architecture that is more suitable for high frame rate video image acquisition. The single chip digital camera is very compact, consumes very little power and tolerates high light input. This research effort has characterized and built a wave-front sensor using CMOS imager as the detector and this data was used to correct the wave-front using low cost adaptive mirrors that are currently available. A wave-front sensor using Shack-Hartmann (SH) lenslet array and the CMOS imager was designed, fabricated and tested for this purpose. Custom software for high speed image acquisition was developed as the software came with the sensor did not have real time capability. Experiments with the CMOS imager revealed that the speed of acquisition of images from the device is fast enough for real time correction experiments. It is noticed that the data output from the device was noisy due to diffraction effect and poor fill factor,

electronic and thermal noise; therefore conventional algorithms used in wave-front sensing could not be used in this case. The generally used quad-cell algorithm needs precise alignment of imager and lenslet array. Therefore, new algorithms were developed for the CMOS imager to compute the centroids in a noisy data of lenslet images. The algorithm essentially searches for circular objects with optimizing parameters as input. This approach has eliminated one of the key requirements of Shack- Hartmann wave-front sensor that the maximum deflection of the lenslet array should be within the sub-aperture of the lenslet array. Wave-front errors were computed in terms of Zernike polynomials. For easy visualization, using the Zernike polynomials obtained, a three dimensional display of the wave-front is computed and shown in the monitor. CCDs, being an efficient detector at low light levels, investigations were also carried out with Andor Low Light Level CCD camera.

For wave-front control, a three actuator tip-tilt mirror platform with piezoelectric actuators and an adaptive mirror fabricated with the newly emerging technology of MEMS (Micro-electro-mechanical systems) were used as wave-front compensators. The cost of MEMS mirrors is a fraction of the cost of the adaptive mirrors made with other technologies. These mirrors were developed only recently; suitable test methods to characterize them were necessary. The mechanical properties of the mirror were first theoretically investigated using Finite Element Analysis. A new non-contact type testing method to find out the shape of the mirror for different actuator voltage configurations of the adaptive mirror was developed. The in-house developed, newly built, Long Trace Profilometer (LTP) was employed for experimental calibration of adaptive mirrors. It is found that the LTP based measurements were more accurate and provided more realistic results. The wave-front sensor data acquisition, processing and computation of control voltages required for adaptive mirror are computationally intensive jobs and require custom made parallel hardware based on array of digital signal processing hardware and software. Here, the approach has been to employ a low cost PC as a computational and control element and to find out whether the low cost hardware satisfies the requirement. PCI bus based interface

card having 40 channels of digital to analog converters was developed for this purpose.

Based on the wave-front sensor outputs and the characteristics of the control mirrors measured with the other experimental methods, correction of the wave-front was achieved by controlling 37 actuators of the adaptive mirror and 3 actuators of the tip-tilt mirror. The results of the experiments have shown that the piezo-electric actuator based tip-tilt mirror has hysteresis while the deformable mirror does not have that. A relation between Zernike coefficients and actuator voltages were derived from the experimental data and the hysteresis effect noticed is removed. Using the newly developed wave-front sensor measurement data and using the adaptive mirrors, aberrated wave-front is corrected. It is found that an aberrated image having 6.4 pixel FWHM can be sharpened to have 3.5 pixel FWHM and the peak intensity has increased from 5610 counts to 36500 counts.

To summarize, this thesis presents a new method of seeing measurement to characterize the atmospheric turbulence; design, construction and evaluation of a new low cost CMOS imager based wave-front sensor and comparisons between CMOS and CCD based systems; a new method of characterizing low cost MEMS based adaptive mirrors; better approach for handling CMOS and CCD based Shack-Hartmann wave-front sensor data and control of tip-tilt and deformable mirror closed loop wave-front error correction system.

Finally, using these newly developed cost effective hardware and software tools with other inputs from this study, a complete solution for stellar image correction has been demonstrated through a specially built laboratory setup for the purpose.

## ACKNOWLEDGEMENTS

The thesis work was carried out as a research and development work at the Electronics and Photonics Laboratories of Indian Institute of Astrophysics. I would like to thank the Director and other Institute authorities for giving me permission and financial support to carry out this work.

Many people have directly and indirectly contributed to the success of this work. First of all I would like to thank my guide Dr A. K. Saxena, Dean, Faculty of Engineering Sciences, Indian Institute of Astrophysics (IIA), for all the help and support he has provided. He has permitted me to use all the facilities and Instruments available at the Photonics laboratories. He has closely monitored all my experimental work and offered timely suggestions and new ideas.

I would like to thank my University guide, Dr A. Sreenivasan, Former Principal, BMS College of Engineering, Bangalore for all the encouragement and timely advice he has provided. In spite of his busy schedule, he has always spent his precious time whenever required.

I would like to thank the Chairman, Electronics Department, Bangalore University for all the help I have received from the Department. All the staff at Ph.D. (Engineering) division, Bangalore University were very helpful whenever I approached them for any help or clarification.

Special thanks to Dr S. K. Saha of IIA, co-observer at VBT for speckle observations, for useful discussions. I would like to thank Mr. J. P. Lancelot, Photonics division, for all the help and useful discussions. He has read the manuscript many times offering suggestions. My special thanks to Mr. V. Gopinath and his associates of Photonics division for installation and alignment of telescope and other optical components for experiments in the laboratory. He has also fabricated many mechanical mounts for optical components. Thanks to Mr. Samson, Mr. Mallappa and other workshop staff who have fabricated mounts for achromats and other optical components initially at a short notice and to Mr. P. K. Mahesh and Mr. D. K. Subramanian for CAD support. Thanks also to all my colleagues at Electronics Laboratory specially Mr. M. R. Somasekar and Mr. Velayudan Kutty for making and

testing the PCBs. I thank Mr. Ismail Jabilullah, Mr. Elangovan, Ms Celine Joseph, Mr. Kanagaraj and Thiagarajan for Xeroxing and binding the thesis.

Finally I would like to thank my wife Mary Elizabeth for all her encouragement and help.

# Contents

## **1 Introduction to image formation using optical telescopes**

- 1.1 Introduction to optical telescopes
- 1.2 Brief history
- 1.3 Stellar imaging
- 1.4 Thesis synopsis

## **2 Image degradation through atmosphere**

- 2.1 Introduction
- 2.2 Turbulence theories and the resolution of the telescopes
- 2.3 Contribution of atmospheric layers to the seeing
- 2.4 Measurement of seeing contribution due to different atmospheric layers
- 2.5 Results of Seeing measurement using speckle interferometry method
- 2.6 Typical parameters of the telescope for which online correction is being worked out and the determination of degradation factor.

## **3 Methods for image improvement**

- 3.1 Introduction
- 3.2 Active optics
- 3.3 Adaptive optics
  - 3.3.1 Greenwood frequency
  - 3.3.2 Isoplanatic patch
  - 3.3.3 Strehl ratio and Marechal criterion
- 3.4 Wave-front representation with Zernike polynomials
  - 3.4.1 Visualization of Zernike polynomials
  - 3.4.2 Zernike polynomials for annular pupil

- 4 Schematic design, identification and evaluation of sub-systems for an atmospheric image correction system**
- 4.1 Introduction to atmospheric image correction system
- 4.2 Adaptive optics system blocks
- 4.3 Wave-front sensing, Different approaches
  - 4.3.1 Shack-Hartmann technique
    - 4.3.1.1 Centroid computations
    - 4.3.1.2 The quad-cell approach
  - 4.3.2 Curvature sensing
  - 4.3.3 Lateral shearing interferometer based techniques
    - 4.3.3.1 In-house developed interferometer based on Babinet compensator
    - 4.3.3.2 Estimation of measurement accuracy
  - 4.3.4 Interferometric Hartmann wave-front sensor
  - 4.3.5 Neural network based phase estimator
  - 4.3.6 Pyramid sensor
- 4.4 Wave-front error computation from Slope data
  - 4.4.1 Polynomial fitting
- 4.5 On the choice of a suitable detector and its parameter for wave-front sensing
  - 4.5.1 CCD based imaging system
  - 4.5.2 Evaluation and selection of CCD camera for wave-front sensor
    - 4.5.2.1 Custom built CCDs
    - 4.5.2.2 Scientific grade, cooled CCDs
    - 4.5.2.3 Intensified, Peltier cooled CCD system
    - 4.5.2.4 Low light level CCD camera
    - 4.5.2.5 Video rate cameras and frame grabbers
  - 4.5.3 CMOS based imaging system
  - 4.5.4 APD based imaging system
- 4.6 Camera control computer and wave-front computation and display computer
- 4.7 On the choice of Tip-tilt and deformable mirror systems for wave-front error compensation

- 4.8 Suitability of low cost components
- 4.9 Closed loop time requirements
- 4.10 Control computer for adaptive mirrors
- 4.11 AO system for online wave-front error measurement system and correction system for VBT

## **5 Optical design and selection of components for wave-front measurement and closed loop correction system for VBT**

- 5.1 Introduction
- 5.2 Optical design for closed loop error measurement and correction system for VBT
- 5.3 Theoretical requirement of a wave-front error measurement and correction system for VBT
- 5.4 Recommendations of system parameters for wave-front sensing and on-line correction system for VBT
- 5.5 Identification of sub-systems for a real time correction system
  - 5.5.1 Lenslet array and precision optical components
  - 5.5.2 Selection of camera system
  - 5.5.3 Selection of deformable mirror system
  - 5.5.4 Selection of tip-tilt mirror system
  - 5.5.5 Computer system

## **6 Design, construction and testing of Wave-front sensor system**

- 6.1 Schematic of Shack-Hartmann lenslet array based wave-front sensor
- 6.2 Tilt mirror system
  - 6.2.1 Power amplifier for Piezoelectric actuators
- 6.3 Computer system
  - 6.3.1 PCI based signal generation card
- 6.4 Testing of the new wave-front sensor using CMOS imager as the detector

- 6.4.1 Summary of the new wave-front sensor using CMOS imager as a detector
- 6.5 Testing of the new wave-front sensor using Low Light Level CCD as the detector
  - 6.5.1 Summary of the new wave-front sensor using LLLCCD as a detector
- 6.6 Algorithms and software development
  - 6.6.1 Zernike polynomial representation in Cartesian coordinates
  - 6.6.2 Computation of Zernike polynomials using lenslet array images
- 6.7 Limitations and accuracy of wave-front error determination
  
- 7 Characterization of tip-tilt mirror and MEMS based adaptive mirror**
  - 7.1 Piezoelectric actuator based tip-tilt mirror system
  - 7.2 Deformable mirror system types
  - 7.3 Deformable membrane mirror characterization
    - 7.3.1 Finite Element Analysis of the membrane mirror
      - 7.3.1.1 Physical properties of membrane mirror
      - 7.3.1.2 Control voltage matrix
    - 7.3.2 Brief introduction to inhouse developed Long Trace Profilometer
      - 7.3.2.1 Test setup for membrane deformable mirror with LTP
    - 7.3.3 Test results of MEMS based 37 channel membrane mirror with LTP
    - 7.3.4 Testing of deformable mirror using interferometer
  - 7.4 Results and discussion of various test methods
  
- 8 Control aspects of tip-tilt and deformable mirrors**
  - 8.1 Important parameters for control
  - 8.2 Control algorithms for tip-tilt mirror
    - 8.2.1 Electronic controller configuration
  - 8.3 Control algorithms for deformable mirror
  - 8.4 Adopted control scheme for deformable mirror

## **9 Closed loop wave-front correction – Laboratory experiments and results**

### 9.1 The experimental setup for calibration

#### 9.1.1 Details of electronic control

#### 9.1.2 Software and algorithms

### 9.2 Determination of control voltages for tip-tilt mirror

### 9.3 Determination of control voltages for membrane deformable mirror

### 9.4 Tilt and deformable mirror correction results

### 9.5 Discussion of the results

## **10 Summary and Remarks**

## **References**

## **Appendix A Flow Chart of the program**

## **Appendix B Data sheet of deformable mirror**

# Chapter 1

## Introduction to image formation using optical telescopes

### 1.1 Introduction to optical telescopes

Modern optical telescopes are high precision instruments that employ latest technology available for its manufacture, testing and deployment at very clear, dust free sites best suited for astronomical observations. The telescope structure is designed and fabricated to point at sub arc-second size, very faint light sources in the sky. As the wavelength of interest is down to 300 nanometers, the precision required for optical fabrication and testing is a demanding task. As the telescope is required to point and track very faint light sources, accurate closed loop motor control systems using computers, feed back devices with fast response is a must. Hence to get good images of the stars through the telescope, best design practices involving mechanical, electrical, optical and thermal engineering methods are required. Even then, the performance of the telescope can deteriorate due to its enclosure which has only one or two degrees of temperature difference with its surroundings. Apart from this, the images taken by all earth based big optical telescopes, even if they are perfectly made, cannot achieve their theoretical resolution because of the distortion created by the earth's atmosphere. The degradation in resolution is tens of times or more for big telescopes. This degradation is called as "seeing effect". As the seeing severely limits the resolution of ground-based optical telescopes, there is an urgent need to devise methods and incorporate them in the telescope so that the full potential of the telescope can be achieved. The current research effort is an attempt to explore and device new methods for the improvement of the resolution by employing best of the possible technologies available today keeping low cost criteria as the main consideration.

## 1.2 Brief history

It is a well known fact that the power of the telescope is proportional to the primary collecting area divided by the solid angle formed by the image, thus a 2.5 m telescope with 0.5 arc-second size image is equivalent in performance to a 5-m telescope with 1 arc-second image [1]. Many factors contribute to the widening of star image. Atmospheric turbulence has long been recognized as one of the most significant factors for broadening the image, limiting the performance of optical imaging systems like telescopes, laser beam projection systems and optical communication systems. Theoretically, the resolving power of a telescope (R) improves by the inverse of its aperture size (D) for a particular wavelength ( $\lambda$ ).

The actual resolving power of the big telescopes of today, the 10 m class of telescopes, even if they are optically perfect, cannot achieve a resolution better than the resolution of 10 to 20 cm diameter telescope, because of the atmosphere. This fact was observed even by the first users of optical telescope like Newton. He said, "If the Theory of making Telescopes could at length be fully brought into Practice, yet there would be certain Bounds beyond which telescopes could not perform. For the Air through which we look upon the Stars, is in a perpetual Tremor; Long Telescopes may cause Objects to appear brighter and larger than short ones can do, but they cannot be so formed as to take away that confusion of the Rays which arises from the Tremors of the atmosphere. The only Remedy is a most serene and quiet Air, such as may perhaps be found on the tops of the highest Mountains above the grosser Clouds" (2).

The first astronomer who was perturbed by the poor star image seen through a big telescope was Babcock. After seeing the image through the 200-inch Hale telescope, he wrote "The seriousness of this (seeing) is evident when one realizes that ideally the 200-inch Hale telescope is capable of giving diffraction images of stars about 1/40 of a second of arc in diameter, yet the size of the "seeing image" produced is in the range 1/3 second to perhaps 5 or 10 seconds."(3). Babcock was the first to give a schematic idea as how to

compensate for the bad seeing. Due to technological limitations, his idea could not be realized in practice for a long time.

Astronomers of subsequent times were desperately trying to improve upon the observations of stars with ever increasing clarity by avoiding the blurriness in the image and with highest possible contrast so that they can see faint features of the extended sources clearly. Instead of real-time approach that depends on the current technology development, off-line methods with post-processing techniques such as speckle interferometry and the associated software were successfully developed to get highly resolved images.

Military reconnaissance has similar requirements of the images taken of earth-orbiting satellites. Most of the technology for real-time image improvement techniques were developed by U.S. military programs and were not available to the outside world. However, the end of the so-called “cold war” has made them to declassify all the development done by them.

One obvious solution to remove the effect of atmosphere is to put the telescope above the earth’s atmosphere. Effort in this direction has culminated in putting a 2.5 m telescope in space, the orbiting Hubble’s Space Telescope (HST). But this is a very costly and technologically challenging task.

Not only in Astronomy, there are other fields where the atmospheric turbulence creates problems. For electronic communication people, the goal is to utilize the high data throughput potential of free space optical signal propagation. The optical signal traveling in the turbulent atmosphere has the same degradation as experienced by the optical wave-front from the distant stars (4). Hence real-time beam steering and control of the transmitter and receiver becomes essential for good communication between two points.

Apart from Astronomy and communication, Ophthalmologists are employing this type of image resolution improvement methods for detailed study of the retina of human eye (5).

Developments in the field of newly emerging Micro-electro-mechanical systems (MEMS) has enabled one or two firms in the world, to develop low cost

adaptive mirrors based on MEMS that can be used for real-time control for correction of aberrated wave-fronts (6).

Application of proven Complementary Metal Oxide Semiconductor (CMOS) technology for imaging camera system design and development instead of Charge Coupled Devices (CCD) has increased the speed of image acquisition and reduced the cost of the camera system. Availability of high speed desktop personal computers have reduced the need for arrays of special purpose processors like Digital Signal Processors (DSP) using which earlier systems were implemented. The cost of new general purpose electronic hardware, like Personal Computers (PC) and the related interface circuit is coming down. As the efforts to understand fully the nature of turbulence is still going on, the latest results from these investigations may help to design a cost effective system. All these developments are propelling individuals to carry on research with limited budgets to solve the age-old problem of turbulence and its impact on imaging systems, which until now are handled by big teams of researchers.

### 1.3 Stellar imaging

Stars are so far away that their angular sizes as seen from earth are almost like a theoretical point in the sky. Let us consider an ideal telescope that does not have any optical aberrations due to manufacturing or due to misalignment of the optical system and that is kept in an ideal place free of atmospheric turbulence. The diffraction pattern produced by a circular aperture is an Airy pattern with an intense central maximum and a number of secondary maxima of considerably lower intensity. Hence, diffraction limited image of a star will appear as a bright central lobe and surrounded by rings each decreasing in amplitude with increasing radius from the center. The first dark ring is at an angular distance of  $1.22 \frac{\lambda}{D}$  from the center.

$$\text{Resolution of an ideal telescope} = 1.22 \frac{\lambda}{D} \quad (1.1)$$

Where  $\lambda$  is the wavelength of observation and  $D$  is the aperture of the telescope. If the telescope is not ideal, then one cannot see the Airy's pattern, the resolution would be degraded even more. The width of the point spread function (PSF) is a measure of the resolution. The other resolution criteria used are

- (i) FWHM - Full Width at Half Maximum of the radial intensity distribution
- (ii) Strehl Ratio - Ratio of central intensity of aberrated image to that of the diffraction limited image. The maximum value of strehl ratio is 1 if the aberrated image is as good as the diffraction limited image.
- (iii) Encircled Energy - The PSF integral over the circle of radius  $\beta$  is called the encircled energy. If all light energy is concentrated in a very small circle, then the light intensity will be more, and hence, faint objects can be easily seen. The effect of atmosphere is to spreads the image to a larger size.

$$\text{Resolution of telescope with atmosphere } R_A = 1.22 \frac{\lambda}{r_o} \quad (1.2)$$

where  $r_o$  is a characteristic parameter of atmosphere called Fried's parameter and its value ranges from 0.1 to 0.2 meter. For a 4 m diameter telescope, diffraction-limited stellar image size is 0.06 arc-second at 500 nm wavelength. But as shown in section 1.1, Babcock had seen the size of the image vary from 1/3 of an arc second to 5 to 10 arc seconds for the same size telescope in an observatory. So for an aberration-free telescope, the image size is typically increased by 50 times and higher. This degradation in image is caused by the earth's atmosphere.

Astronomers use the parameter  $\mathcal{E}_{fwhm}$  (full width at half maximum) which is the angular diameter of a star image at the focus of telescope as an indicator of seeing. It is given by

$$\mathcal{E}_{fwhm} = 0.98 \frac{\lambda}{r_o} \quad (1.3)$$

The monochromatic image of a point source is the point spread function (PSF). The intensity distribution in the focal plane in the case of quasi-monochromatic incoherent source can be described by the following equation:

$$c(x,y) = o(x,y) * p(x,y) \quad (1.4)$$

where  $c(x,y)$  is the image in spatial coordinates,  $o(x,y)$  is the object intensity distribution and  $p(x,y)$  is the telescope – atmosphere point spread function; the symbol  $*$  denotes convolution. Off line image improvement methods try to obtain good images by deconvolution process using the point spread function.

Present work aims at providing a low cost approach for optical image correction in a closed loop adaptive optics system for atmospherically degraded images.

#### **1.4 Thesis synopsis**

The main body of the thesis consists of theoretical and practical investigations about the effects of atmospheric turbulence on astronomical imaging systems, quantifying the turbulence by experiments, identifying and implementing a wave-front error measurement system using high speed cameras and developing new algorithms for wave-front error computation, quantifying the errors using functions like Zernike polynomials, and identifying and implementing a wave-front correction system using mirrors which can be electronically controlled to have the desired shapes so that the optical path differences created by the mirrors can effectively eliminate the optical path errors in the in-coming wave-front. A brief summary of the above investigations are chapter wise detailed.

- Chapter 1 gives a very short Introduction to image formation using an optical telescope
- Chapter 2 gives a brief introduction to atmospheric turbulence theory, effects of turbulence on imaging systems and seeing variations with atmospheric parameters and their measurement.
- Chapter 3 gives details about some of the methods used for image improvement
- Chapter 4 describes the various schemes of a wave-front error measurement system, their merits and de-merits, algorithm for wave-front error

computation, speed against accuracy trade off, identifying and selecting low cost, high performance imaging camera, electronically controllable low cost mirrors and introduction to their controls.

- Chapter 5 deals with the Optical system design of wave-front measurement and closed loop correction system for 2.34M Vainu Bappu Telescope (VBT). ZEMAX optical design package is used to find out the maximum tilts required out of tilt mirrors and the depth of surface required out of deformable mirrors. Based on these inputs suitable adaptive optics components are chosen.
- Chapter 6 deals with the construction and testing of a Shack-Hartmann lenslet array based wave-front sensor. Results of CMOS imager based wave-front sensor and a cooled low light level CCD camera based sensors are given. It also explains design and fabrication of electronic sub-systems. Advantages and disadvantages of both camera systems are highlighted. Failure of conventional algorithm for noisy environment and the development of new algorithms developed to work with poor signal to noise ratio images are shown. Investigation of noise performance, new algorithms for data reduction and results for a standard test beam produced by a tilt mirror system are given.
- Chapter 7 gives details about the test methods developed to characterize the adaptive mirrors. Investigation using theoretical method like Finite element analysis and experimental methods developed by us are outlined and compared.
- Chapter 8 gives introduction to control of adaptive mirrors and electronic control units.
- Chapter 9 explains about the experimental setup for wave-front sensing and wave-front error correction system. The experimental results match with theoretical performance very closely, thus proving that the new methods and algorithms developed for the wave-front error measurement and correction system has worked satisfactorily. The failure of the system to correct the errors occasionally is investigated and remedial actions suggested.
- Chapter 10 gives summary of the results followed by remarks.

## Chapter 2

### Image degradation through atmosphere

#### 2.1 Introduction

Starlight, which travels many light years, encounters the earth's atmosphere at the end of its travel. For a very simplified view, it can be assumed that there are many patches of uniform temperature regions (cells) of 10 to 20 cm diameter size between a source like a star and the telescope as shown pictorially in fig 4.1. Each cell acts like an independent small telescope in front of a big telescope. The image formed by the big telescope is the collection of many spots produced by each of the small telescope. Hence all ground-based telescopes cannot produce good images with the resolution they are capable of as given by eqn.1.1. The random refractive-index inhomogeneities in the atmosphere, associated with turbulence, distort the characteristics of light traveling through the atmosphere and thereby limit the resolution with which an object can be viewed through the atmosphere. The limitation is due to warping of the isophase surfaces and intensity variations across the wave-front, which prevents all portion of the lens from "working together" (7). In severe cases of seeing, the appearance of the image at the telescope is described as "boiling". Through interference effects, complicated patterns of phase produced by seeing on larger apertures generate a diffraction pattern that is broken into many bright granules, or speckles, having random appearance (8). The average size of the uniform temperature cells can be correlated to the Fried's parameter  $r_0$  and the resolution of the telescope is given by eqn. 1.2

This  $r_0$  can be imagined as the telescope diameter that would produce a diffraction spot of the same size as that produced by the atmospheric turbulence on a point source observed with an infinite mirror.

## 2.2 Turbulence theories and the resolution of the telescope

According to Kolmogorov-Obukhov model of atmospheric turbulence (9), fully developed turbulence represents a collection of eddies with various scales, from the largest outer-scale  $L_0$  eddies down to the smallest, inner-scale ( $l$ ) eddies. The phase structure function for the mean square differential phase error between points separated by a distance  $r$  is given by

$$D_q = 6.88 \left( \frac{r}{r_0} \right)^{\frac{5}{3}} \quad (2.1)$$

where  $r_0$  is the Fried's parameter and denotes seeing quality. This expression is valid for separation within the inertial range of turbulence,  $l \ll r \ll L_0$  where  $l$  and  $L_0$  are inner and outer scale of turbulence. For fully developed turbulence, in the lower atmosphere, the inner scale is of the order of 1 cm.  $L_0$  in the upper atmosphere is probably in the range of 10 – 100 m. The finite inner scale of turbulence has no effect on the actual image motions; the finite outer scale can have noticeable effect on image motion. Larger values of  $L_0$  indicate larger image motion. Coulman et al. (10) found that variation of the  $L_0$  with altitude could be fitted by a simple empirical relation:

$$L_0(z) = \frac{4}{1 + \frac{(z - 8500)^2}{2500}} \quad (2.2)$$

where both  $L_0(z)$  and the altitude  $z$  are expressed in meters.

Many observers have measured image distortion and motion that is smaller than what the theory predicts. Experiments using long-baseline interferometers have also produced evidence of small  $L_0$  (11). According to some observers, the value of  $L_0$  is in the range of 20 to 40 cm, which is much lower than the values predicted by Kolmogorov theory. This has prompted Stewart McKechnie (12) to propose an alternative theory of turbulence which was strongly disputed by Tatarskii et al. (13) who claim that conventional theory can explain the fine quality images observed by Christu (14). It has been customary to build large telescopes to less than diffraction limited standards. Instead of the

telescope's inherent ability to focus light into, say, 0.03", the diffraction limit of a 5 m telescope at visible wavelength, it is considered acceptable if the telescope can focus most of the light into an image patch a few tenths of an arc-sec across due to the mechanical fabrication difficulties. It is possible however, as noted by McKechnie, that the low quality of telescope's mechanical structure and optics also contribute significantly to the poor quality of the images (15).

### **2.3 Contribution of Atmospheric layers to the seeing**

Atmospheric turbulence limits the angular resolution of a large telescope and causes random motion of diffraction-limited image formed by a small telescope. The sun heats the earth surface during daytime and as the night progresses; the absorbed heat is released in the atmosphere. The change in temperature variation is high near the ground and it falls off as one goes high vertically from the surface. The image degradation, also known as seeing is caused at five distinct places. They are the free atmosphere (>1 km), the boundary layer (<1km) the surface layer (a few tens of meters from ground), inside the telescope building, known as dome seeing, and at the primary mirror and its surroundings. Over the years, astronomers found good observatory sites to install their telescopes by measuring the seeing contribution given by the different layers of atmosphere. Rene Racine (16) has found the typical night-time refractive index structure constant  $C_n^2$  profile above Mauna Kea is due to a relatively stable underlying background of turbulence, which contributes a seeing spread of ~0.3", upon which are often superposed one or two dominant turbulent layers. The seeing is a property of atmosphere, independent of telescope size. For longer infrared wavelengths, where the seeing improves with increased wavelength, increased telescope size can bring improved resolution. The atmospheric turbulence at a particular place depends on the topography of the local place, surface composition of earth, height, dust level in the atmosphere, temperature gradient, wind velocity etc. Temperature inhomogeneities that are generated in turbulence layers are responsible for local variations in the

refractive index, which perturbs the otherwise homogeneous propagation of incident light wave. The parameter which gives a measure of the optical turbulence intensity related to the in-homogeneities is the refractive index structure constant  $C_n^2(h)$  (17). From this parameter, seeing parameter can be calculated by using the following equation

$$r_o = (16.7\lambda^{-2} \int C_n^2(h) d(h)^{\frac{3}{5}}), \quad (2.3)$$

and the seeing disk width can be computed using

$$\varepsilon_{fwhm} = 5.25\lambda^{-\frac{1}{5}} (\int C_n^2(h) d(h)^{\frac{3}{5}}) \quad (2.4)$$

The spread in the image size owing to seeing varies as  $\lambda^{1/5}$ , the seeing errors being smaller at longer wavelengths. A ten-fold increase of  $\lambda$  would reduce the seeing by a factor of 0.63. This is a very low rate of change compared with the variation of image size due to diffraction. The image spread due to seeing and diffraction is the sum of these effects; the seeing spreads light from every point of the diffraction image. The effect of atmosphere can be thought of contribution from dominant layers spread vertically upwards. Each turbulent layer contributes to the degradation of the image according its intensity.

## 2.4 Measurement of seeing contribution due to different atmospheric layers

Different methods are used to measure the vertical refractive index profile. For the surface layer, micro-thermal measurements are made. Micro variation of temperature at a known horizontal separation like 1 m is measured by thermal sensors mounted on a mast one above the other with a suitable vertical separation. By measuring the minute difference in temperature between the horizontal sensors and their variation with height,  $C_n^2$  profile can be computed. Micro-thermal measurement of surface layer seeing at a Himalayan mountain range of India was reported by Pant et.al., (18) and the contribution of this layer above 13 m is 0.32". Significant contribution for bad seeing can come from heights less than this. J.Vernin et. al, measured the surface layer contribution

alone at a height of 12 m to be 0.08" (19) which is almost negligible. Hence the telescope should be installed at a sufficient height from ground to avoid contribution from the surface layer.

For measuring the contribution of boundary layer and free atmosphere, the micro-thermal tower can be placed in a balloon and the microstructure of the thermal field can be measured during its free flight ascent. J.Vernin et. al, measured the seeing using balloons and found the contribution of boundary layer to be 0.5" and that of the free atmosphere to be 0.4" .

R.D.Marks et.al, (20) measured the contribution of seeing due to different layers on the high Antarctic plateau. The contribution of surface layer was more but the contribution of free atmosphere was 0.23 to 0.26". For a good telescope site such as Mauna Kea, the seeing is mainly due to upper atmosphere variations as observed by J.C.Christu. Fionn (21) formulated schemes to predict the seeing using an automated meteorological station, micro-thermal sensors and differential image motion monitors. They have proposed an Astronomical Weather Station site monitor (22) as an interface between the observer and the terrestrial observatory environment.

The  $C_n^2$  profile reported by Martin (23) shows a gradual increase at about 1 km height and a sharp abrupt change at an altitude of about 10 to 11 km. Hence, seeing produced by this layer may be more dominant.

The conclusion from the above discussion is that the contribution of the atmospheric layer at 8 to 12 km height, which is part of the free atmosphere, is an important contributor for seeing since its magnitude is about 0.3" to 0.5" at visual wave length. The boundary layer contribution is almost nil and the surface layer contribution depends on the height from the earth's surface which can be easily overcome by placing the telescope to clear the minimum required height. As the free atmosphere seeing contribution cannot be avoided, site selection for

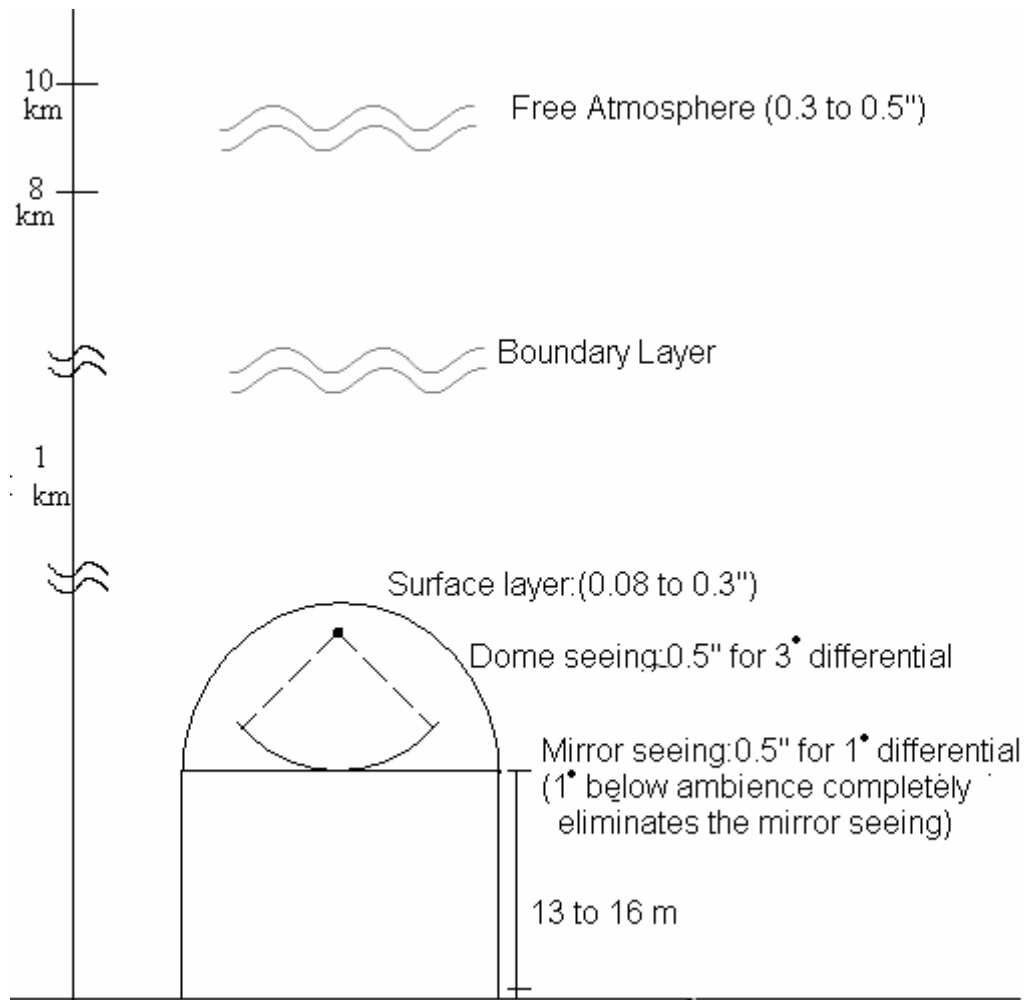


*Fig. 2.1 Five different layers at which seeing is getting affected. The contribution from the surface layer, mirror and dome seeing is under the control of the observatory while contribution from free atmosphere cannot be avoided.*

telescope has to measure the contribution of this layer and a best site can be selected based on the lowest value of free atmosphere contribution.

The contributions from dome and the mirror should be kept as small as possible by following good thermal engineering principles. One classical example of dome seeing improvement in the recent past was in Anglo-Australian Telescope (AAT), Australia. The important principle employed here is to have the same temperature inside the dome as it is outside. Dome venting fans were

installed (24) which removed the difference in temperature between outside and inside the dome. I had the opportunity of witnessing myself the improvement in seeing sitting in the console room of AAT; within minutes of the operation of those huge fans; seeing improved considerably. In Vainu Bappu Telescope (VBT) operated by Indian Institute of Astrophysics, Bangalore, inside to outside temperature variation in the dome was found to be about 3 deg. C and remedial measures were taken to reduce this difference (25).

Mirror seeing is the most dominant contributor for bad seeing at ground level. A temperature difference of 1 deg. C between primary mirror surface and its surrounding contributes about 0.5" seeing. It is found that cooling the primary mirror 1 deg below the ambient temperature eliminated the contribution of the mirror seeing (26). The apparent size of the stars as viewed from earth is only a few tens of milli arc seconds but the atmosphere spreads the image to about half of an arc second. Theoretical resolution of bigger telescopes is also in tens of milli arc-seconds but the true potential of the telescope cannot be utilized because of the atmosphere. Hence, there is a need to measure the contribution of atmosphere at the telescope site. Measuring the Fried's parameter helps us to design a proper on-line correction system.

## **2.5 Results of Seeing measurement using Speckle Interferometry method**

Chinnappan et. al., (27) have used an intensified CCD camera based speckle interferometer to observe speckles of close binary stars at VBT. Using the data taken during this observation, apart from finding the star parameters, they have measured the seeing at very short intervals for the first time using the speckle interferometer. This instrument is best suited for evaluation of the seeing using short exposure times, based on which suitable parameters for real-time image correction can be worked out. As seen in the previous paragraph, the different methods developed and used by various groups to measure seeing involve long integration time while obtaining the image. The integration times may vary from a

few seconds to tens of seconds. This has the effect of averaging the distortions created by the atmosphere. It was theoretically shown by Fried [28] that short-time exposures in the order of atmospheric coherence time which is in the order of a few tens of milliseconds, where the image motion is frozen, contains higher resolution information than long exposure images. A down to earth example is seeing a rotating fan at high speed. What we see is not the blades of the fan but a big circle formed by the path of the rotating blades. If one wants to see the blades of the rotating fan, one has to take a photograph with a very short exposure time. Speckle interferometry method uses the same principle. In speckle interferometry, hundreds of short exposure images of about 10-millisecond integration time are first recorded using a highly sensitive CCD [29] camera and later it is analyzed off-line to get the highly resolved images and seeing at very short intervals of time.

The speckle interferometric (30) technique was used to find the Fried's parameter at 2.34M Vainu Bappu Telescope through a 5-nm band filter centered on  $H\alpha$  at Kavalur Observatory [31]. This instrument was built at the Indian Institute of Astrophysics [32] for observation of close binary stars. Normally, an exposure time of 10 to 20 ms is used for observation depending on sky conditions. At these time intervals, each patch of the wave-front with diameter  $r_0$  would act independently of the rest of the wave-front resulting in many bright spots called 'speckles' spread over the area defined by the long exposure image. These speckles can occur randomly along any direction inside an angular patch of diameter  $1.22 \lambda / r_0$ . If many short exposure images and their autocorrelations are summed, the summed images have the shape of seeing disk,

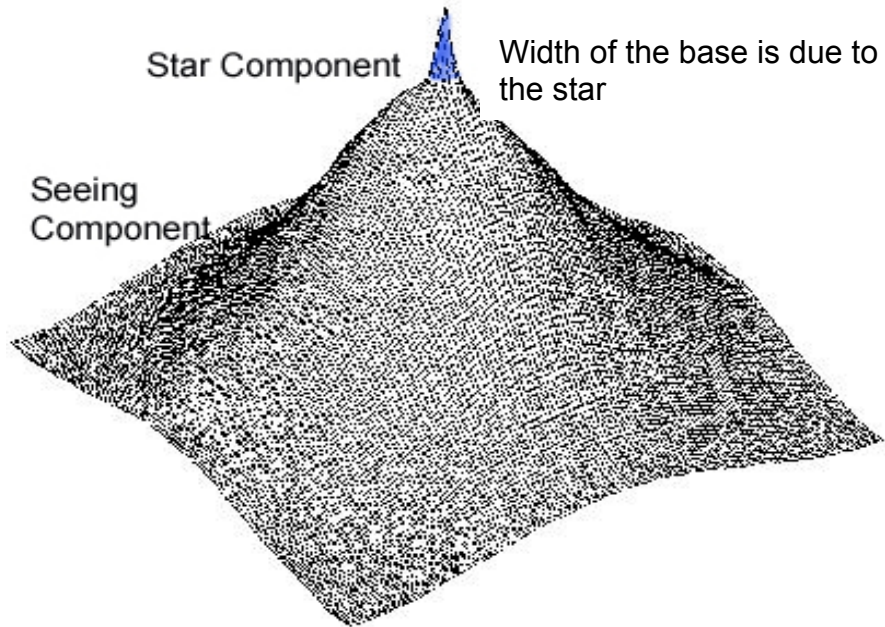


Fig. 2.2 Autocorrelation of star  $\alpha$ -Andromeda observed with speckle interferometer at 2.3 m Vainu Bappu Telescope

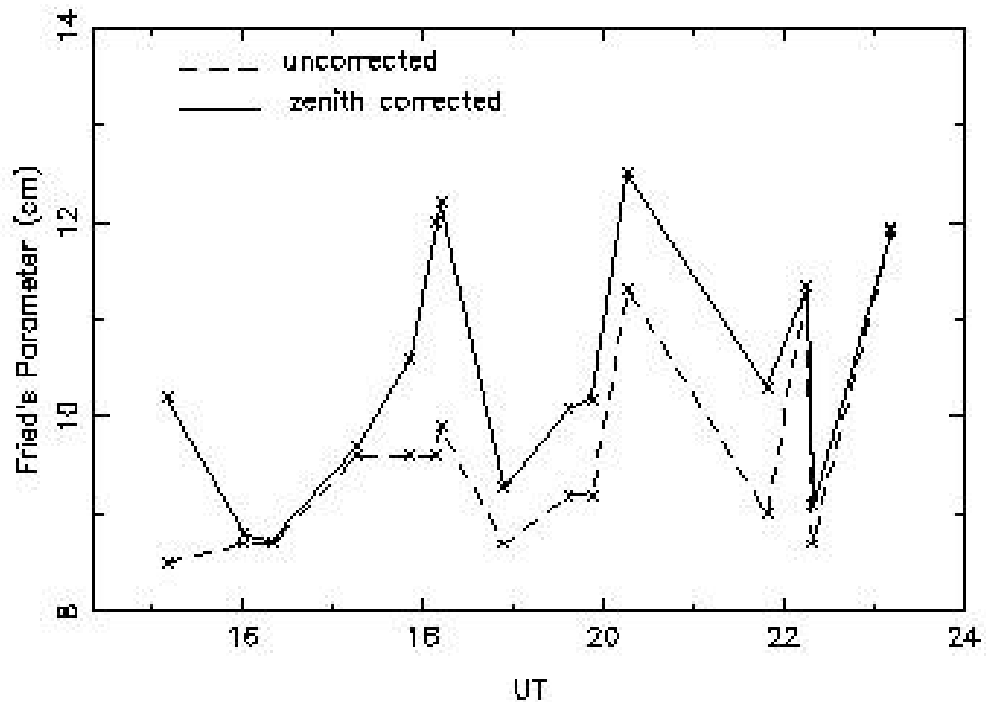


Fig. 2.3 Night time variation of Fried's parameter  $r_0$  as observed at VBT, Kavalur.

while the summed autocorrelations contain autocorrelation of seeing disk together with the autocorrelation of the mean speckle cell. From the seeing disk, the Fried's parameter is computed by measuring the Full Width at Half Maximum (FWHM) at these short intervals. At VBT, The image scale at Cassegrain focus is 6.854 arc-sec per mm. In the speckle interferometer, the image scale is magnified to 0.68 arc second per mm by microscopic objective. The image at the focus is sampled at 0.027" per pixel. Fig. 2.2 shows the autocorrelation of the seeing disk together with autocorrelation of the mean speckle cell that is due to the star. The size of the  $r_0$  is found to be 11.44 cm at the FWHM. The variation of Fried's parameter  $r_0$  over the night is shown in fig. 2.3. It is seen from the graph that the seeing value keeps on changing even at these short intervals. The atmospheric correction system to be designed should take this factor into account. It is to be noted that, to my knowledge, this is the first time that speckle interferometric technique is used to measure Fried's parameter at these shorter time intervals. The temporal variations of the seeing over a period of time was also measured and it is shown in fig 2.4. It can be seen from the figure that the atmospheric effects are not steady but vary over the entire night even at short intervals. As shown in the rectangular box in the left, even within a few seconds interval,  $r_0$  varies from 9.75 cm to 9.25 cm and then to 10 cm. The rectangular box at the right side shows even larger variations; starting at 12.2 cm and coming down to 9.2, reaching a peak value of 14 and back to 11.5 cm. These variations indicate how the closed loop control of correction system should follow the atmospheric variations so that it is effective in compensating the seeing. There is a limit to the correction rates that can be applied to the in-coming wave-front by the adaptive mirrors. It can be seen from fig. 2.4 that the average  $r_0$  value is about 10 cm. As a rule of thumb, 10 cm value of  $r_0$  corresponds to 10 milli-second correction loop time at visible wavelength which may be difficult to achieve.

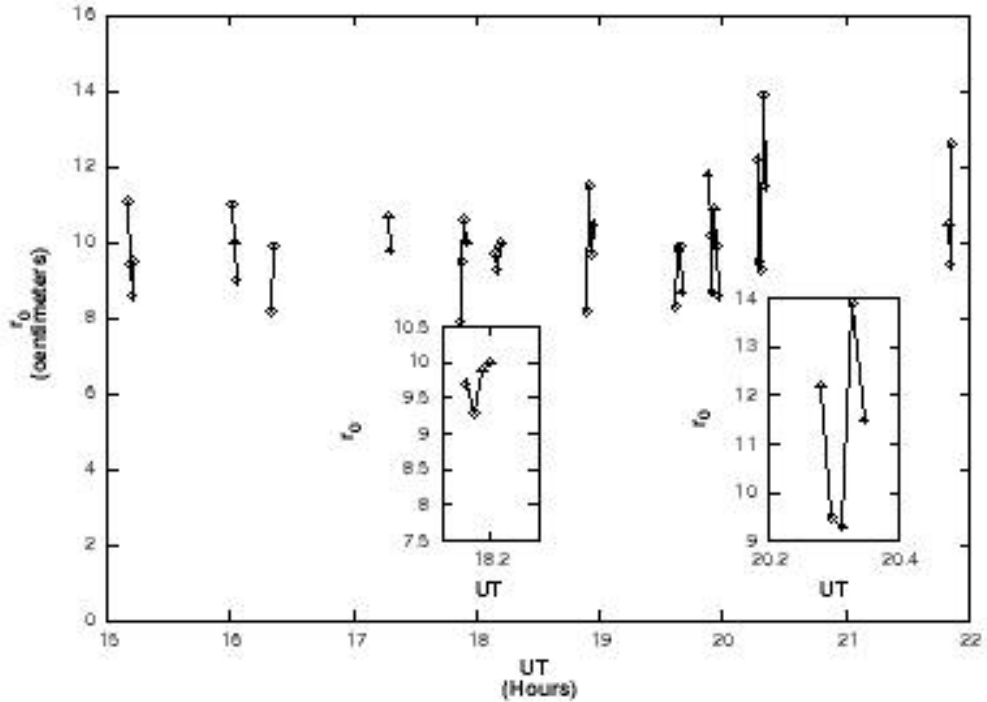


Fig. 2.4 Variation of  $r_0$  at short interval over a night

As seeing depends on wavelength,  $r_0$  value is higher at longer wavelengths for the same atmospheric conditions and the correction frequency will be correspondingly less

## 2.6 Typical parameters of the telescope for which online correction is being worked out and the determination of degradation factor.

It is found that  $r_0$  value varies from 7.5 cm to 12 cm, 12 cm corresponding to 1 arc second seeing at the observed wavelength. For the system design, lowest Fried parameter of 7.5 cm can be taken. Next chapter gives various methods used for image correction. The correction system parameters largely depend on telescope's parameters and the atmospheric seeing parameters. The important atmospheric parameter  $r_0$  was measured by experiments as explained earlier.

The important parameters of 2.3M VBT are given below:

Diameter	:2360 mm
Clear aperture	: 2320 mm
Material	: Zerodur
Density	: 2.52 gm / cc
Cassegrain hole dia	: 720 mm
Central obscuration	:0.3
Prime focus F ratio	:3.237
Prime image scale	:27.463 " / mm
Cassegrain focus F ratio	: 12.97
Aperture of Secondary mirror	: 630 mm
Cassegrain image scale	: 6.854 " / mm

The measured  $r_0$  value for this telescope varies from 7.5 cm to 12 cm. It can be computed from the above data that the degradation caused by atmosphere varies by a factor of  $(234 / 7.5)$  19.4 to 32.

## **Chapter 3.**

### **Methods for image improvement**

#### **3.1 Introduction**

It is seen from the discussion in section 2.4 that at earlier times, good seeing value was taken as about 1" and it is enough if a telescope is able to concentrate 80 % of the light energy in sub-arc-second diameter. Now it is very clear that sub-arc second seeing is not exceptional, but it is the norm. In order to utilize the best seeing available at a particular place, all the contributors for seeing as explained in chapter 2, section 2.4 should be studied and corrective methods are to be taken to improve the seeing, which is in our control. This includes choosing a site with less than 0.5 arc-sec atmospheric seeing contribution. Dome seeing and telescope mirror seeing which is under user's control should be made negligible by appropriate design methods. In our VBT, best seeing available are in the range of 0.75 sec. of arc to 1.5 sec of arc. Our study and technological development centers around these parameters. For online servo correction of images, the system developed has two parts; Active Optics and Adaptive Optics. The following pages give a brief introduction to both.

#### **3.2 Active Optics**

Over the years, every attempt has been made to reduce the cost of the telescope as well as well as to incorporate latest technology and materials available. Mirrors with almost zero thermal expansion like Zerodur were developed. The diameter to thickness ratio of the mirror was considerably reduced. Present day telescopes of 8 to 10 m aperture are only 15 to 25 cm thick. To keep down the very large dome costs, they have much faster prime focal ratio, which is around 1.8. The fast systems introduce field curvature and some astigmatism, so that the image field is approximately spherical and off-axis

image is out of focus. The accurately figured thin mirror cannot maintain its surface accuracy because of its low stiffness. The requirements to achieve good imaging with light weight mirror are the maintenance of mirror figure and optical alignment independent of telescope pointing. Modern telescopes depend upon an active optics system, which measures the aberration of the telescope system using a wave-front analyzer system and provides real-time collimation of the telescope and optical figure control of the primary mirror (33). Hence the mirror support system has been changed from passive supports to what is called as active supports. In passive mirror support system, a set of springs and counter weights offer equal but opposite thrust to the mirror bottom, so that there is no net force acting on the mirror and no variation in the optical figure in any orientation. In active support system, each support is driven by some form of force drivers like stepper motors or electro-hydraulic support system to correct for any surface distortion. A computer monitors these forces by measuring the pressure between the mirror bottom and the actuators using load cells. The active optics system, in principle, is similar to adaptive optics correction system, the main difference being that it does not correct the wave-front distortion by atmosphere. Active optics correction is done once in a few tens of seconds, or some times minutes, where as adaptive optics correction, depending on wavelength, may vary from a few milliseconds to a few tens of milliseconds. We plan to use Active approach for initial alignment and tuning of the primary and secondary mirror support systems.

### **3.3 Adaptive optics**

The plane wave-front coming from the distant star is corrugated and tilted by the intervening atmospheric turbulent layers. The effect of this disturbance is that the star image size is broadened by many tens of times and fine details in the image are completely lost. Fried showed that some part of the distortion can be considered to be random tilt of the wave-front. This tilt displaces the image but does not reduce its sharpness. If very short exposure image is recorded, the

image sharpness is insensitive to tilt which can be substantial part of total distortion (34). Real-time stellar image correction methods, that is also called adaptive optics in a broader sense, measures the errors in the incoming wave-front by capturing images at very short intervals as suggested by Fried. Based on one reference image and an aberrated image, the tilt and other errors like defocus, coma etc., are computed in real time. The wave-front distortion introduced by the earth's atmosphere is compensated by means of one or more optical components which are introduced in the light path and which can introduce controllable counter wave-front distortion, which spatially and temporally follows that of the atmosphere. It is basically a multi-channel, real-time, wave-front measurement and correction control system. Real-time electronic control has become indispensable not only for image degradation correction but also for the basic operations of the large astronomical telescopes. Without it, in fact, the latest generation of telescopes could not function at all [35]. For bigger projects like OWL (Over Whelming Large) telescope of 100-m size which are in the drawing boards now [36] or even the 4-m class telescopes of the last decade, funds for implementing adaptive optics is not a big concern but the technology limitation is a big constraint. Even for moderate size telescopes of 2-m aperture, the degradation created by the atmosphere is considerable and it needs to be corrected. Improvement in the image quality by using adaptive optics method will improve the throughput of even these moderate size telescopes (37). Using this compensation technique, the resolution can also be increased nearing to the intrinsic resolving power of the telescope. The benefits of such a system is that because of the increased resolution and light intensity, objects can be observed in great detail and more faint objects can be observed and the observing time can be reduced. The following pages give a brief summary of the important parameters that are required for implementation of an adaptive optics system.

As explained in section 2.2, the atmospheric degradation can be represented by the single parameter  $r_0$  that describes the turbulence strength

along the line of sight. The atmospheric variations can be expressed in terms of refractive index structure constant,  $C_n^2$  as follows:

$$r_o = 0.185 \lambda^{\frac{6}{5}} \cos^{\frac{3}{5}} z \left( \int C_n^2 dh \right)^{-\frac{3}{5}} \quad (3.1)$$

and the dependency of Fried parameter with wavelength is given by

$$r(\lambda) = \left( \frac{\lambda}{\lambda_o} \right)^{\frac{6}{5}} r_o \quad (3.2)$$

It is seen that  $r_o$  also depend on zenith angle,  $z$ , and varies as  $\lambda^{6/5}$ . Hence,  $r_o$  value of 10 cm at 550 nm corresponds to 53 cm at 2.2  $\mu\text{m}$ . As  $r_o$  is more at infrared wavelength, successful real-time control of the aberrated wave-front is achieved only in the longer wavelengths. At shorter wavelengths, the speed of wave-front measurement and control becomes so fast that it becomes impossible to do full compensation with the currently available technology. The same viewpoint is expressed by McGuire et. al., (38) and their comment is “.. thus making adaptive optics work possible in the infrared and next to impossible in the visible”.

The standard deviation of the phase introduced by seeing with a separation of  $D$  as given by Roddier (39) is

$$\sigma_\phi = 2.62 \left( \frac{D}{r_o} \right)^{\frac{5}{6}} \quad (3.3)$$

In terms of optical path difference this becomes

$$\sigma_z = 2.62 \left( \frac{\lambda}{2\pi} \right) \left( \frac{D}{r_o} \right)^{\frac{5}{6}} \quad (3.4)$$

The characteristic time scale for evolution of the wave-front is

$$T_o = 0.314 \frac{r_o}{V_{wind}} \quad (3.5)$$

where  $V_{wind}$  is the transverse wind velocity in the path of the light beam.

### 3.3.1 Greenwood frequency

The rate of control for an adaptive optics systems is related to the Greenwood frequency (40) and is given by

$$f_o = 0.4 \frac{V_{wind}}{\sqrt{\lambda}} z \quad (3.6)$$

$z$  is the altitude of the turbulent layer. The sampling frequency for closed loop control is about 30 times higher than the Greenwood frequency.

### 3.3.2 Iso-planatic patch

The area on the sky over which aberrations are same is called the iso-planatic patch, and the angular radius is called iso-planatic angle  $\theta_o$ . It depends on the altitude  $H$  at which dominant disturbance in the atmosphere takes place.

$$\theta_o = 0.314 \frac{r_o}{H} \quad (3.7)$$

As  $r_o$  parameter is a crucial one for adaptive optics,  $r_o$  was measured at short exposure time using speckle interferometer as explained section 2.5

$$\text{Degradation factor caused by atmosphere} = D / r_o \quad (3.8)$$

The degradation can be thought of spread of the image to a large area as shown in fig. 2.2. This factor is known as point spread function (PSF) of the telescope. In an atmospherically degraded telescope, the width of the PSF is a measure of the resolution. As the shape of the PSF may be irregular, Full Width at Half Maximum (FWHM) of PSF gives a numeric measure of resolution. When the image is spread into larger area, the intensity of the central core decreases.

### 3.3.3 Strehl ratio and Marechal criterion

To quantify the performance of an Adaptive Optics system, Strehl ratio can be used. It is defined as the ratio of the central intensities of the aberrated

PSF and the diffraction-limited PSF of the instrument. If aberrated image PSF is  $P(\rho)$  and diffraction limited PSF is  $P_0(\rho)$ ,

$$\text{Strehl ratio } S = \frac{P(\rho)}{P_0(\rho)} \quad (3.9)$$

The integral of PSF is unity. The PSF integral over the circle of radius  $\beta$  is called encircled energy. If all the energy is concentrated into a small area, the photon intensity is more; correspondingly, the photon to electron conversion in detector like CCD is more, thus reducing the observing time required for faint objects. For objects fainter than sky background, the observing time is reduced as  $r_o^{-2}$  where  $r_o$  is the Fried's parameter.

Once the normalized intensity at diffraction focus has been determined, the quality of the optical system may be ascertained using the Marechal criterion which states that a system is regarded as well corrected if the normalized intensity at diffraction focus is greater than or equal to 0.8, which corresponds to an rms wave-front error  $\leq \lambda / 14$ .

Having defined some of the important parameters for AO system, the next step is find out the types of errors that can be present in an incoming wave-front and their representation.

### **3.4 Wave-front representation with Zernike polynomials**

The Zernike polynomials (41) were developed as a convenient tool for representing wave-front optical aberrations over a circular pupil. A minor problem with this representation is that non-rotationally symmetric aberrations like coma and astigmatism are decomposed into two components, one along the x-axis and the other along the y-axis. These, however, may be combined in a single aberration with a certain orientation that depends on the magnitude of the two components.

Zernike polynomials can be conveniently written in polar coordinates as products of angular functions and radial polynomials. These polynomials are defined by

$$Z_{j\text{even}} = [2(n+1)^{\frac{1}{2}} R_n^m(r) \cos m\theta] \text{ when } m \neq 0 \quad (3.10)$$

$$Z_{j\text{odd}} = [2(n+1)^{\frac{1}{2}} R_n^m(r) \sin m\theta] \text{ when } m \neq 0 \quad (3.11)$$

$$Z_j = [(n+1)^{\frac{1}{2}} R_n^m(r) \cos m\theta] \text{ when } m=0 \quad (3.12)$$

where

$$R_n^m(r) = \sum_{s=0}^{\frac{(n-m)}{2}} \frac{(-1)^s (n-s)!}{s! [\frac{(n+m)}{2} - s]! [\frac{(n-m)}{2} - s]!} r^{n-2s} \quad (3.13)$$

The values of  $n$  and  $m$  satisfy the following condition;

$m \leq n$ , and  $n-m$  is even. The index  $j$  is a mode ordering number derived from  $m$  and  $n$ . The total number of modes up to a given radial order is

$$j_n = \frac{(n+1)(n+2)}{2} \quad (3.14)$$

These polynomials with their order, azimuthal frequency, and physical description are given in table 3.1, in terms of polar coordinates. The pertinent properties of these polynomials are listed by Malacara (42) and it is given below:

- The values of  $n$  and  $m$  are always integers and satisfy  $m \leq n$  and  $n - m =$  even. Consequently, only polynomials with certain combinations of  $n$  and  $m$  exists.
- They are invariant in form with respect to rotations of axes about the center of the pupil.
- $R_n^m = R_n^{-m}$

## Zernike polynomials

n	m	n-2m	Zernike polynomial polar coordinate	meaning
0	0	0	1	piston or constant
1	0	1	$\rho \sin\theta$	tilt about y axis
	1	-1	$\rho \cos\theta$	tilt about x axis
2	0	2	$\rho^2 \sin 2\theta$	astigmatism with x axis at $\pm 45^\circ$
	1	0	$2\rho^2 - 1$	focus shift
	2	-2	$\rho^2 \cos 2\theta$	astigmatism with x axis at $0^\circ$ or $90^\circ$
3	0	3	$\rho^3 \sin 3\theta$	Triangular atigmatism (base) on x axis
	1	1	$(3\rho^3 - 2\rho)\sin\theta$	3 <sup>rd</sup> order coma along x axis
	2	-1	$(3\rho^3 - 2\rho)\cos\theta$	3 <sup>rd</sup> order coma along y-axis
4	0	4	$\rho^4 \sin 4\theta$	
	1	2	$(4\rho^4 - 3\rho^2)\sin 2\theta$	
	2	0	$6\rho^4 - 6\rho^2 + 1$	
	3	-2	$(4\rho^4 - 3\rho^2)\cos 2\theta$	
	4	-4	$\rho^4 \cos 4\theta$	

Table 3.1. Zernike polynomials up to fourth degree

- $$\int R_n^m R_n^m r dr = \frac{\delta_{nm}}{[2(n+1)]}$$
- $$\int d2r W(r) Z_j(r) Z_{j'}(r) = \delta_{jj'}, \quad \text{where}$$

$$W(\mathbf{r}) = \frac{1}{\pi} \quad \text{for } |\mathbf{r}| \leq 1 \text{ and } W(\mathbf{r}) = 0 \quad \text{for } |\mathbf{r}| > 1$$

is the weighing function.

$$OPD(\rho, \phi) = \sum a_j \lambda Z_j(\rho, \phi). \quad (3.15)$$

The  $a_j$  coefficient determines the contribution of the  $j^{\text{th}}$  Zernike term ( $Z_j$ ) measured in terms of waves i.e., in units of wavelength  $\lambda$ . In this representation  $a_j$  coefficient represents the root mean square deviation of the OPD surface contributed by the  $j^{\text{th}}$  Zernike term.

Algorithm used for mirror testing and AO wave-front sensing are different even though the wave-front error measuring hardware has similar features. In mirror testing applications, speed of computation is not important, hence, time consuming algorithm like centroiding with efficient filters to remove noise can be used. The wave front errors in terms of Zernike polynomials can be computed and displayed. AO applications need fast computing time, hence quad cell approach is normally used. Wave front display may not be possible.

The aberrated wave-front  $W$  can be mathematically represented in terms of a series:

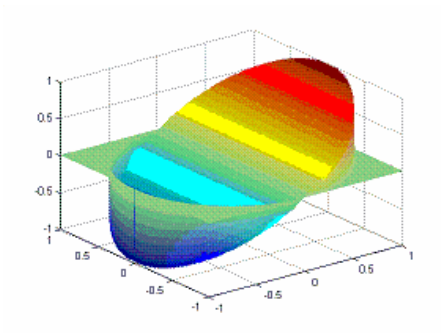
$$W = Z_0 * (\text{piston term}) + Z_1 * (\text{x tilt term}) + Z_2 * (\text{y tilt term}) + Z_3 * (\text{defocus term}) + Z_4 * (\text{astigmatism at 45 deg}) + Z_5 * (\text{astigmatism at 0,90 deg}) + Z_6 * (\text{coma along x axis}) + Z_7 * (\text{coma along y axis}) + Z_8 * (\text{Trefoil on x axis}) + Z_9 * (\text{Trefoil on y axis}) + \text{higher order terms} \quad (3.16)$$

Here,  $Z_0$ ,  $Z_1$  and  $Z_2$  etc. are the Zernike polynomial coefficients;  $W$  is reconstructed wave-front using Zernike polynomial upto 3<sup>rd</sup> degree which gives 10 terms as shown above. For more accuracy, many terms can be included. The constants  $Z_0$ - $Z_9$  are the constants of Zernike polynomial, which can be obtained from the combined centroid position. In general, it is sufficient to fit the data to 20 Zernike terms for low order aberrations. A typical example from electrical sciences is in order now. Electrical engineers are very familiar with Fourier Transforms and the related applications. A square wave can be generated from

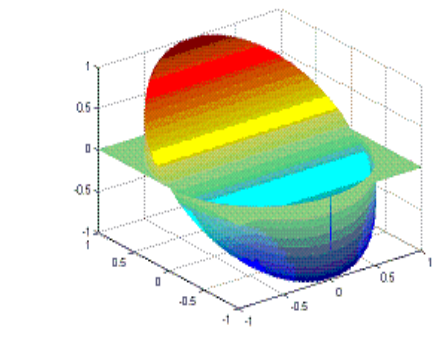
summing an infinite number of sine waves with multiple frequency of the fundamental frequency. But the question is how many terms you can sum. For theoretical studies you can practically include infinite frequencies, ie., as many terms as you can if you have computing resources and time, but if you are constrained by computing power and time and if you want to use your generated waveform for some control application which needs fast action, then you have to compromise on the number of terms to be include to generate the waveform which will just do the work within the required time with the fastest computer power at your disposal. In a similar fashion, the aberrated wave-front can be reconstructed from a large number of Zernike polynomial terms, but the question is how many terms are to be summed to give a reasonable representation of the measured wave-front.

### **3.4.1 Visualization of Zernike polynomials**

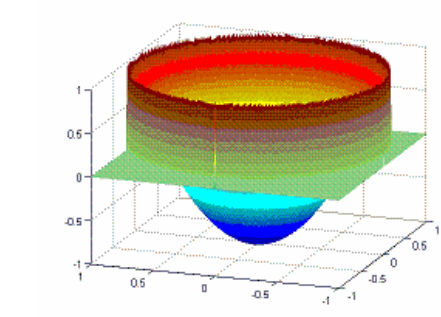
As explained earlier, Zernike polynomials were developed as a convenient set for representing wave-front aberrations over a circular pupil. Zernike polynomials in terms of familiar optical errors such as tilt, astigmatism, coma etc. are shown in fig. 3.1. The pseudo colour pictures are generated using MATLAB<sup>®</sup>. Zernike coefficient  $Z_0$ , which corresponds to piston term, is not shown. The tilt about Y axis is Zernike coefficient  $Z_1$ . Major optical errors are mentioned below the corresponding pictures. In a typical optical telescope, the aberrations will have a complex shape because of the combination of above said errors in different proportions. Two such simple combinations of two optical errors are also shown above; one is the sum of X tilt and Y tilt and the other one is the sum of defocus with third order spherical aberration.



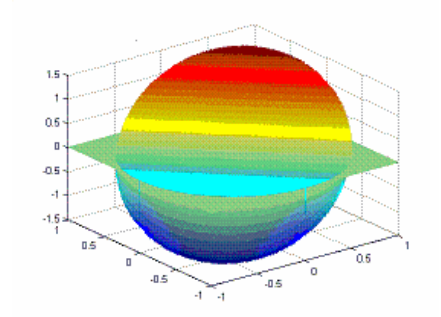
*Tilt about X axis*



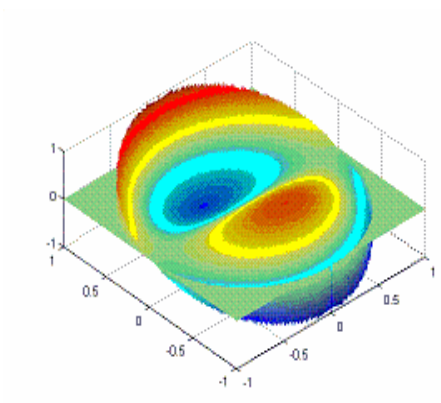
*Tilt about Y axis*



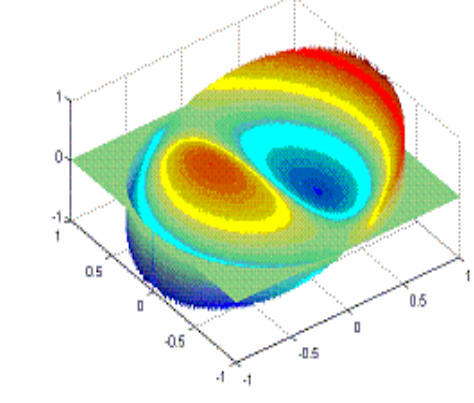
*Defocus*



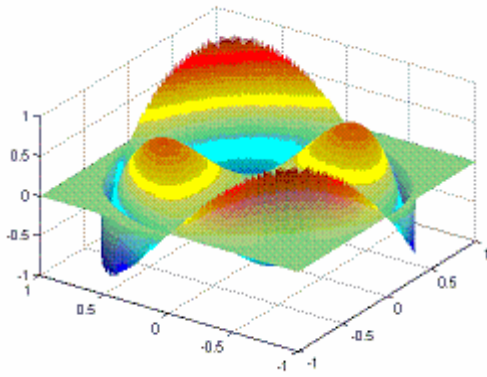
*X and Y tilt combined*



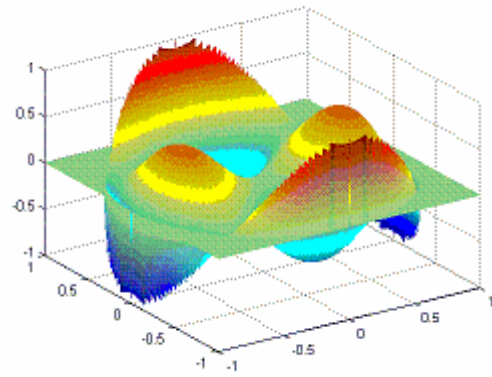
*Coma along Y axis*



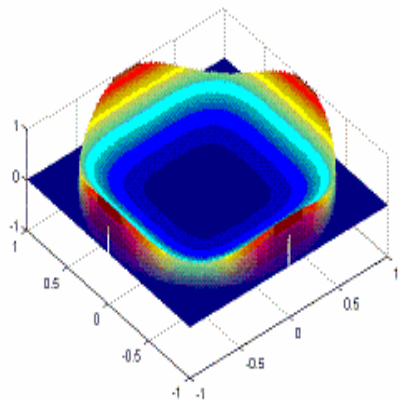
*Coma along X axis*



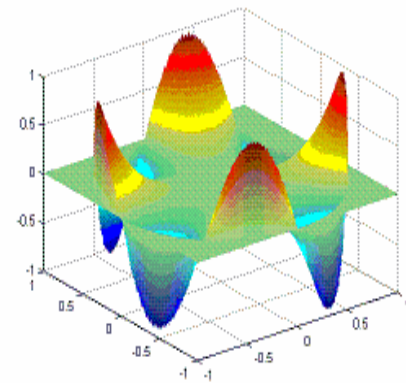
*5<sup>th</sup> order astigmatism +/- 45 deg*



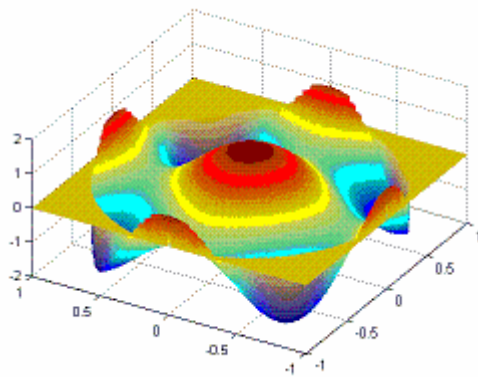
*5<sup>th</sup> order astigmatism 0, 90 deg*



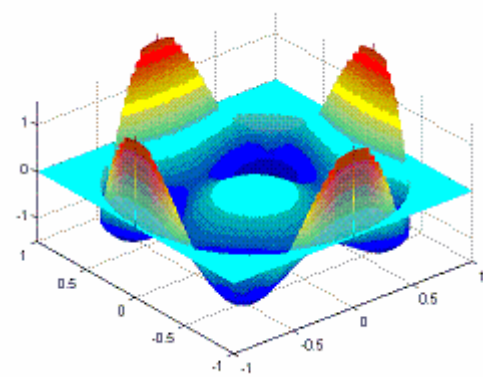
*Tetrofoil X*



*Tetrofoil Y*



*3<sup>rd</sup> order spherical*



*Defocus + 3<sup>rd</sup> order spherical*

*Fig. 3.1 3-D view of optical aberrations for some of the Zernike coefficients.*

### **3.4.2 Zernike polynomial for annular pupil**

Conventional Cassegrain optical telescopes have a central hole in the primary mirror to pass the light reflected by the secondary mirror. Zernike polynomials are to be suitably modified to take this into account. Annular Zernike polynomials can be constructed from circular Zernike polynomials by Gram-Schmidt orthonormalization process. Mahajan (43) has developed an algorithm for Annular Zernike polynomials and detailed discussion is available in that reference. Since the annulus preserves the azimuthal symmetry, only radial functions of the same azimuthal order are orthonormalized with respect to each other.

Having studied briefly, the two methods of online correction and the related important concepts, the requirements for an atmospheric correction system is discussed in the next chapter.

## **Chapter 4**

### **Schematic design, identification and evaluation of sub-systems for an atmospheric image correction system**

#### **4.1 Introduction to atmospheric image correction system**

Having defined the aim of research work in chapter 1 and measurements of the relevant atmospheric parameters in chapter 2, the typical requirements to design and implement a wave-front measurement and correction system which can remove the aberrations in an optical telescope system is taken up next.

#### **4.2 Adaptive optics system blocks**

The essential subsystems of an adaptive optics system are

- Wave-front sensing (WFS)
- Wave-front error computation
- Control of adaptive mirrors to compensate the measured errors

Wave front sensing unit captures the snap shot of incoming wave-front with some geometrical error measuring devices fitted to an imaging camera. The captured images are analyzed and errors present in the images are computed in known optical quantities. Once the errors are known, corrective action is taken using adaptive mirrors to remove the distortion in the in-coming wave-front. Detailed design and construction of these blocks are given in the following chapters.

Schematic diagram of closed loop a compensation system is shown in Fig. 4.1. In a conventional imaging system, the imaging camera like CCD is mounted at the focal plane of the telescope. As discussed earlier, this image is broadened many times by earth's atmosphere. The distortion in the wave-front is in the form of random tilts and corrugations. In the real time image correction system, a portion of the beam is obtained by beam splitters, before it goes to the final detector, and the wave-front sensor analyzes the image and measures various



## **4.2 Wave-front sensing – Different approaches**

There are two methods available for wave-front sensing, i.e., zonal and modal techniques. In these methods, the optical beam aperture is divided into sub-apertures and the wave-front phase slope values are computed in each of these sub-apertures using difference in centroids from a reference image and an aberrated image. The wave-front can be constructed from these slope values. Out of many available methods for wave-front sensing, some of the methods suitable for Adaptive Optics are detailed below

- Shack – Hartmann technique
- Curvature sensing
- Lateral Shearing Interferometry
- Interferometric Hartmann wave-front sensor
- Neural network wave-front sensor
- Pyramid wave-front sensor

These different methods are briefly described in the following subsections.

### **4.3.1 Shack-Hartmann technique**

The classical Hartmann grid was developed (44) to test optical telescope's primary mirror during fabrication. The Hartmann grid has equal size square grids made of metal rods covering the whole aperture of the primary mirror. The number of squares depends on the number of measurement points one wants to accurately sample the mirror surface. The grid is placed on the primary mirror and image formed by the mirror for an input beam is captured. If the mirror surface has least optical errors, then the image of the grid also will be squares of equal size. If error is present in the mirror then, the square opposite to that location will have a distorted square. As the location of the mirror having error is known, it can be worked upon further to reduce the error. Later Shack changed

the position of the grid to the pupil's plane. As the size of the image formed by primary mirror after focus is small, the measuring grid can be of small size, typically about 25 mm. But the number of grid points required for big telescopes are very high. A small lens replaces each aperture so that each one collects the light in the area and focuses to a small spot giving a sharp image. The Shack-Hartmann (SH) sensor consists of an array of lenslets or small lenses of size typically of 300 to 500 microns arranged in the form of a square grid and accurately positioned from one another. Making so many sub-apertures within a small area with good dimensional accuracy is a very difficult task. The physical construction of lenslet array involves advanced manufacturing technology and remains as a proprietary of the manufacturer.

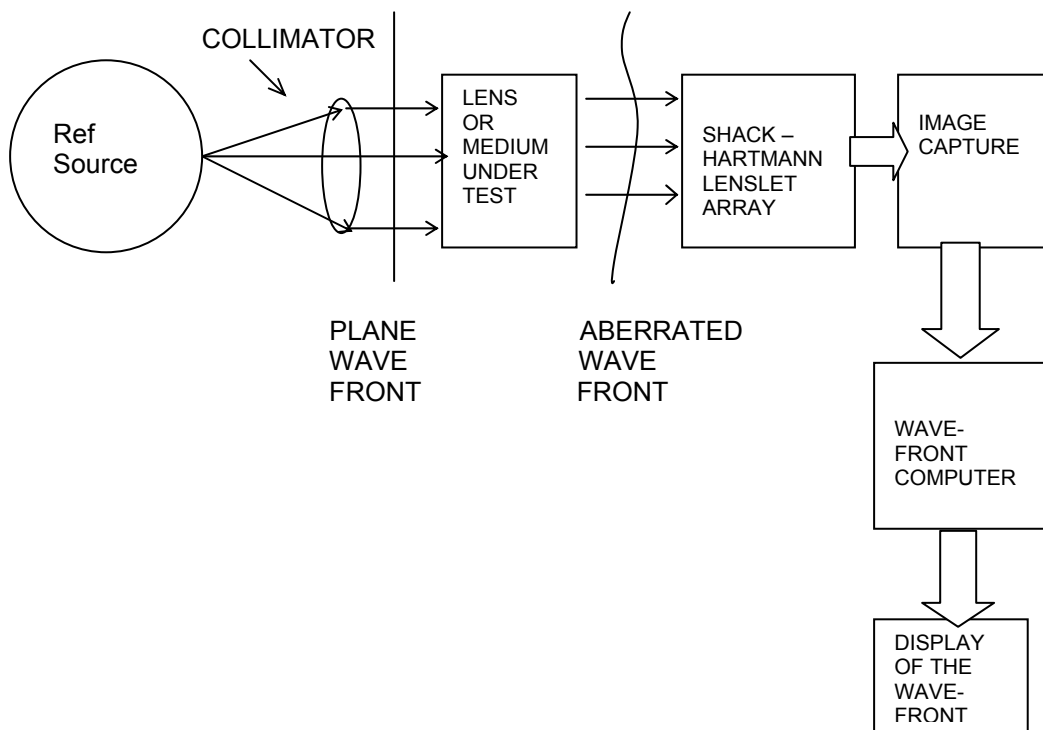
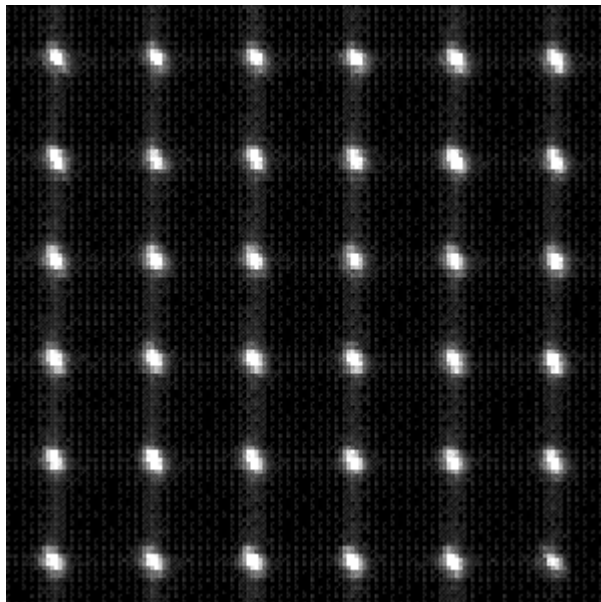


Fig. 4.2 Block diagram of Shack-Hartmann wave-front sensor.

A typical image of 6 x 6 lenslet array is shown in fig. 4.3. SH wave-front sensor needs two wave-fronts for analysis, the reference wave-front and the object wave-front. Reference wave-front is a plane wave-front produced by an accurately collimated beam of light. The object wave-front is the image what the object under test gives. Using the two images, the errors in the incoming beam is computed in terms of Zernike polynomial. The typical setup of a Shack-Hartmann sensor is shown in fig. 4.2. Reference image is first captured without the lens or medium under test not kept in the optical path. The aberrated image is taken with lens to be tested is inserted in the optical path. The parallel beam created by the point source after passing through a pinhole and the achromat passes through the lenslet array. If the beam is perfect, each lenslet focuses the light to a spot and all the spots will have uniform distribution. If an aberrated optics is introduced in the light path, depending on the aberration, the lenslet spot positions in each sub-aperture are shifted in different directions and to various magnitudes.



*Fig. 4.3 Image of a 6 x 6 lenslet array captured by a CCD camera (Twice Magnified)*

By computing the deviation of each lenslet position of the object image from the reference lenslet image positions, slope values at the lenslet positions are computed from which the errors in the incoming beam is then computed in terms of Zernike polynomial. Optical errors in the device under test is computed by methods explained in section 4.4. A lenslet array is placed in a conjugate pupil plane in order to sample the incoming WF. If the WF is plane, each lenslet forms an image of the source at its focus (Fig. 4.4 a) which is uniformly distributed. If the WF is disturbed, to a first approximation each lenslet receives a tilted WF and forms an off-axis image in its focal plane (Fig. 4.4 b).

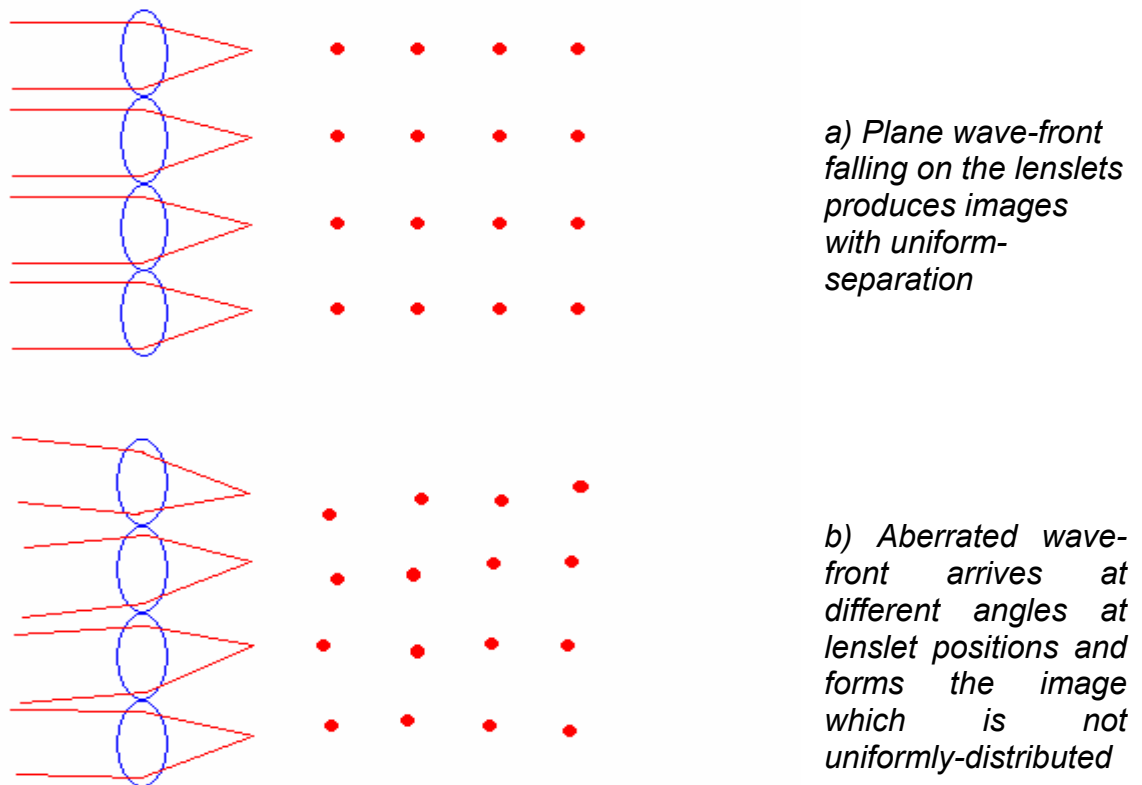
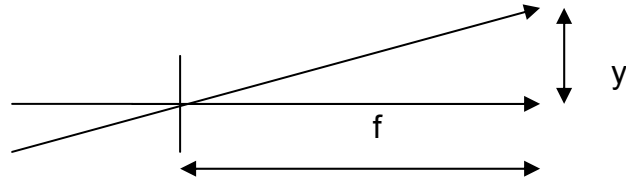
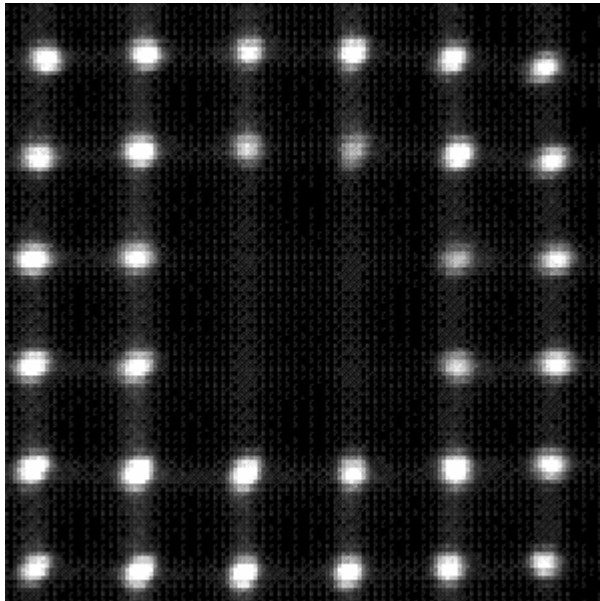


Fig 4.4 Shack-Hartmann wave-front sensor spots (a) plane wave (b) aberrated wave



*Fig. 4.5 Reference ray and aberrated ray are shifted by a distance  $y$*

The measurement of image position gives a direct estimate of the angle of arrival of the wave over each lenslet aperture. It is to be noted that the SH WFS always requires a reference plane wave generated from a reference source in the instrument, in order to calibrate precisely the focus positions of the lenslet array. The Zernike coefficient 0, which is the piston movement cannot be measured by the Shack-Hartmann lenslet array based wave-front sensor



*Fig. 4.6 An Aberrated wave-front taken with a Cassegrain telescope.*

The average gradient of the wave-front over the sub-aperture along the Y axis as shown in fig. 4.5 is given as

$$\text{Slope} = y / f \quad (4.1)$$

In a practical system like a Cassegrain telescope, the SH image from the telescope is as shown in fig. 4.6. Careful observation of the lenslet spots will reveal deviations in the spot position. The 4 missing spots in the middle are due to the central hole in the primary mirror of a Cassegrain telescope. The 6 x 6 lenslet image shown in fig. 4.4 is the reference image and fig 4.6 is an aberrated image of a telescope system. Next section describes how to find out the wave-front errors using these two images.

#### 4.3.1.1 Centroid computations

The algorithm normally used for SH sensor is centroid computation to determine the lens spot positions to sub-pixel accuracy.

The centroid of a sub aperture is calculated by the formula

$$\text{x-position of the centroid} \quad C_x = \frac{\sum_x \sum_y x * I(x, y)}{\sum_x \sum_y I(x, y)} \quad (4.2)$$

$$\text{y-position of the centroid} \quad C_y = \frac{\sum_x \sum_y y * I(x, y)}{\sum_x \sum_y I(x, y)} \quad (4.3)$$

Where  $I(x,y)$  is the intensity of the pixel at location (x,y) and symbol \* is multiplication. The centroid co-ordinates are given by

$$\text{Centroid} = (C_x, C_y). \quad (4.4)$$

The reference frame is used to calibrate the aberrations of the SH system itself. The displacement of the spot center  $X_c, Y_c$  within the sub-aperture with respect

to a reference position  $X_r, Y_r$  is measured. Local gradient of the wave-front  $\Phi(x,y)$  is obtained by the following equations

$$\frac{\delta\phi}{\delta x} = \frac{S_x}{f}, \quad (4.5)$$

$$\frac{\delta\phi}{\delta y} = \frac{S_y}{f} \quad (4.6)$$

where  $S_x = X_c - X_r$ ,  $S_y = Y_c - Y_r$ , and  $f$  is the focal length of the lenslets. From the computed centroid position of the reference frame and the aberated frame, displacements of spot positions are calculated and the slope values in  $x$  and  $y$  direction is computed by equations 4.5 and 4.6. Some times the lenslet array and the imaging camera are mounted in a pre-fixed geometrical position to each other to reduce the computation time of lenslet positions. This scheme is explained in the next section.

#### **4.3.1.2 Wave-front error computation using Shack Hartmann wave-front sensor - The Quad Cell approach**

The SH sensor's two-dimensional array of lenslets divide the incoming wave-front into an array of spatial samples known as sub-apertures. In the reference image shown in fig. 4.3, there are 36 sub apertures for 36 lenslets. The total image size is 150 by 150 pixels. Each sub-aperture is 25 by 25 pixels, each pixel is 20 by 30 micrometer size. In the quad cell scheme (45) shown in fig.4.7 (a), the quadrants A, B, C and D represent one sub aperture and  $I_a, I_b, I_c$  and  $I_d$  are the intensities of the quadrants. The position of the lenslet image in the reference wave-front is arranged in such a way that it is at the center of a quad cell. The aberrated wave-front lenslet image is shifted from the center as shown in fig. 4.7 b.

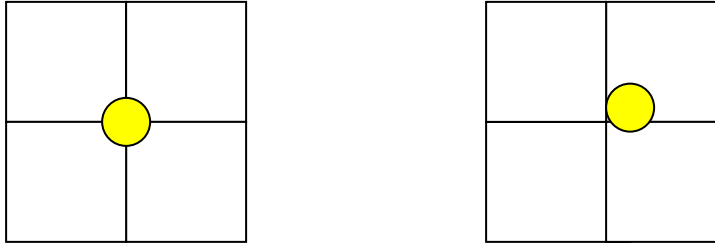


Fig. 4.7 a) The reference image      b) Aberrated image position in a quad cell

Gradient calculations are performed on each sub-aperture using the following algorithms:

$$\text{X slope} = \frac{(l_b + l_d) - (l_a + l_c)}{(l_a + l_b + l_c + l_d)} \quad (4.7)$$

$$\text{Y slope} = \frac{(l_a + l_b) - (l_c + l_d)}{(l_a + l_b + l_c + l_d)} \quad (4.8)$$

Each quad cell may contain 2 x 2 or 4 x 4 pixels. Wave-front error computation using the slope values are given in section 4.4. If one compares the computation of slopes with centroiding algorithm and the quad cell approach, the latter approach involves less number of calculations, hence less time for computation. But the precise alignment of lenslet centre with the center of quad cell is a very difficult problem to be solved.

The advantages of SHWF sensor are

- Geometrical measurement technique, tolerant to vibrations
- Works with white light
- With CMOS or CCD imager, high measurement accuracy and possibility of measuring large deflections

The only drawback of SHWF sensor is that it cannot detect piston movement.

### 4.3.2 Curvature sensing:

The curvature sensor (CS) has been proposed and developed by Roddier to make WF curvature measurements instead of WF slope measurements (46). The Laplacian of the WF, together with WF radial tilts at the aperture edge, are measured, providing data to reconstruct the WF by solving the Poisson equation with the Neumann boundary conditions. An interesting feature of this approach is that a membrane or a bimorph mirror can be used directly to solve the mirror control equations, because of their mechanical behavior, a priori removing any matrix multiplication in the feedback loop. The principle of this sensor is presented in Fig 4.8. The telescope of focal length  $f$  images the source in its focal plane. The CS consists of two detector arrays placed either side of focus. The first detector array records the irradiance distribution in plane  $P_1$  at a distance  $l$  before the focal plane. The second detector records the irradiance distribution in plane  $P_2$  at the same distance  $l$  behind the focus. A local WF curvature in the pupil produces an excess of illumination in one plane, for instance, and a lack of illumination in other. A field lens is used for symmetry in order to re-image the pupil planes.  $P_1$  and  $P_2$  can also be seen as two defocused pupil planes.

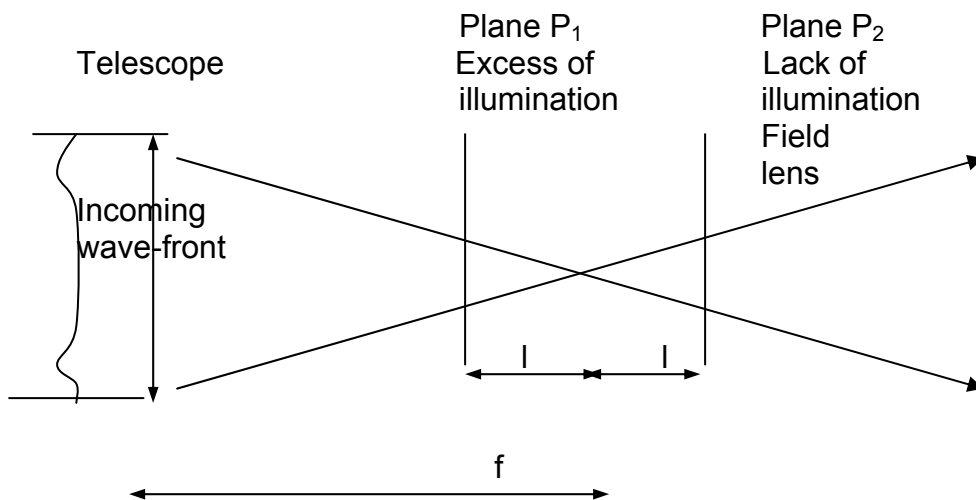


Fig. 4.8 Principle of curvature sensor

It can be shown that in the geometrical optics approximation, the difference between the two-plane irradiance distributions is a measurement of the local WF curvature inside the beam and of the WF radial first derivative at the edge of the beam.

### **4.3.3 Lateral Shearing Interferometry (LSI) based wave-front sensors**

The LSI combines the wave-front with a shifted version of itself to form interference. A shearing device splits the incoming wave-front into two components and shifts one of them. The two wave-fronts are mutually displaced by a distance  $s$ , called shear. They interfere in their overlap area. By their position, the interference fringes are a measure of the phase difference over the shear distance in the shear direction. In order to determine completely the WF, two interferograms having shear in orthogonal directions ( $x$  and  $y$ ) are required. At the entrance of the sensor, the WF is usually split into two similar channels using beam splitters, one with a  $x$ -shear device and the other with a  $y$ -shear device. Each channel is equipped with a detector array to measure a map of the WF gradient. Each detector pixel corresponds to an area in the telescope pupil called a sub-aperture. The two detector planes must be divided into contiguous sub-apertures for maximum efficiency. Therefore, the detector array directly determines the spatial sampling of the WF. The area of one detector also provides a spatial filtering of the phase gradients. The measurement represents the average slope of the OPD in the shear direction, over each sub-aperture.

#### **4.3.3.1 In-house developed interferometer based on Babinet compensator**

An interesting interferometer based on Babinet compensator using Polarization Shearing Interferometer concept was developed by Saxena (47) and the same was used in the new Long Trace Profilometer (LTP) (48) developed by him. The optical head of the LTP is based on polarization shearing interferometer concept.

A Babinet Compensator (BC) has been conveniently used for shearing or splitting the beam into two. Their interference can be utilized for local slope measurement. It consists of two similar quartz wedges cemented together in such a way that the combination forms a plane parallel plate. The optic axes of the two component wedges are parallel to the external faces and are mutually perpendicular. This prism splits an incident ray into two rays called ordinary ray and extraordinary ray traveling in different directions as shown in Figure 4.9. The lateral displacement between the rays is different at different distances from the optical axis of the Babinet compensator. The angular splitting  $\alpha$  is given by

$$\alpha = 2(n_e - n_o) \tan \phi \quad (4.9)$$

where  $\phi$  is the wedge angle and  $n_e$  and  $n_o$  are refractive indices of the BC material (Quartz) for extra-ordinary and ordinary rays. For quartz  $(n_e - n_o) = 0.00911$

Placing a lens at a distance equal to its focal length from point 'o' one gets two parallel beams, their separation is

$$S = \alpha f \quad (4.10)$$

These two beams are allowed to fall on the surface under test. The two reflected beam from the surface are made to interfere and the interference pattern in the collimating lens plane which acts as the pupil plane is imaged onto the detector with a suitable magnification.

Interferogram in the detector plane can be represented by

$$\left(\frac{\partial W}{\partial x}\right)S = n\lambda, \quad (4.11)$$

where  $\frac{\partial W}{\partial x}$  is the wave-front slope at a given point,

$n$  is the order of the fringe

$\lambda$  is the wavelength of the laser beam.

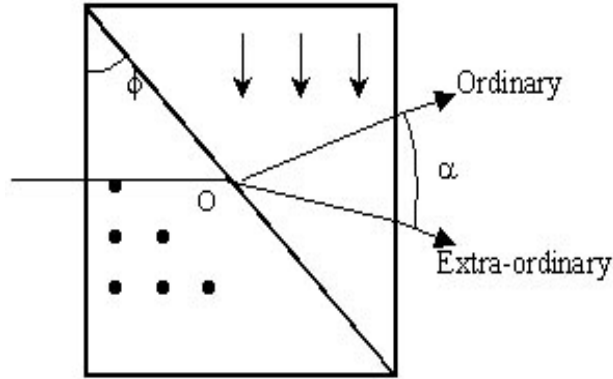


Fig. 4.9 Schematic of Babinet Compensator

#### 4.3.3.2 Estimation of Measurement accuracy

Slope at any point of the wave-front can be represented by the equation

$$\left(\frac{\partial W}{\partial x}\right)S = n\lambda \quad \Delta\left(\frac{\partial W}{\partial x}\right)S = \Delta n\lambda \quad (4.12)$$

Therefore the Shift in the fringe  $\Delta n$  is governed by the following equation:

$$\Delta n = \frac{[\Delta\left(\frac{\partial W}{\partial x}\right)S]}{\lambda} \quad (4.13)$$

or Slope error accuracy at any point can be determined by

$$\Delta\left(\frac{\partial W}{\partial x}\right) = \left(\frac{\Delta n}{S}\right)\lambda \quad (4.14)$$

Using the BC based interferometer, Saxena and Lancelot have developed a wave-front sensor (49) that can be used for adaptive optics work (50). An interferogram obtained in the laboratory using the above scheme is shown in fig.

4.10

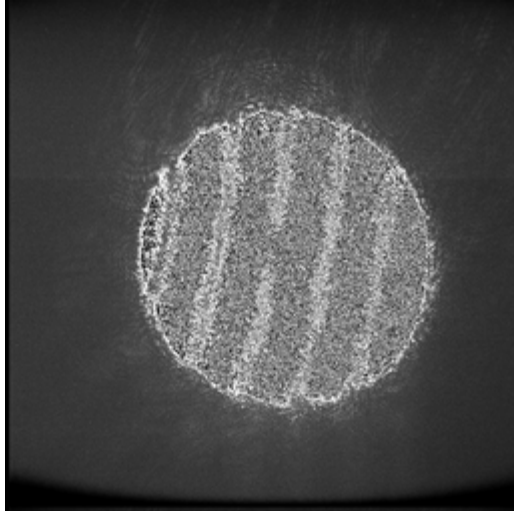


Fig. 4.10 Interferogram obtained with BC based interferometer with CCD camera

#### 4.3.4 Interferometric Hartmann Wave-front Sensor

The interferometric Hartmann wave-front sensor (51) directly measures wave-front phase differences unlike the Shack-Hartmann wave-front sensor which measures the wave-front gradients. Instead of a lenslet array, the interferometric device uses a Hartmann aperture mask array placed at the collimated re-imaged pupil as shown in fig. 4.11.

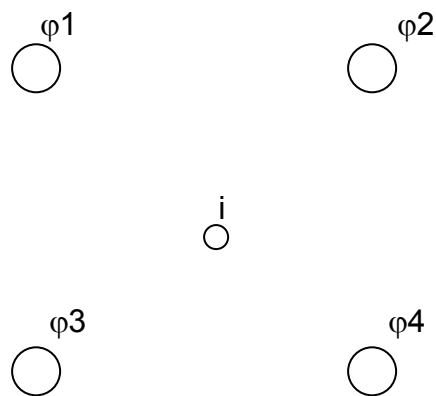


Fig. 4.11 Interference spot created by 4 lenslets forming a quartet

A single converging lens focuses the airy patterns produced by the apertures. An interference spot  $i$  is formed by an aperture quartet. The spot is exactly centered between the apertures only if the four individual phases in a quartet  $\phi_1$  to  $\phi_4$  are equal. Unequal phases cause a shift in the spot position proportional to the phase differences in the apertures. The merits and limitations of this wave-front sensor are listed by the authors in the reference.

#### **4.3.5 Neural network phase estimator**

Sandler et.,al, (52) applied a neural network to an in and out of focus images of a star to estimate the phase distortions. According to them, the neural network has several advantages over the Hartmann sensors or interferometers. The neural network operates directly on the optical point spread function of the telescope system. A neural network is a parallel computational architecture composed of individual elements called neurons in a similar way the biological neurons function. Their phase recovery network employs multiple perceptrons. The network is trained by adjusting the connecting weights using the back-propagation algorithm, which repeatedly presents the network with training data and minimizes the squared error between the known solution and the network output, using a gradient search technique. The optical phase distortion was represented by Zernike polynomials. The authors feel that the neural network in conjunction with an active deformable mirror can be used for adaptive optics on an astronomical telescope.

#### **4.3.6 Pyramid sensor**

Pyramid sensor was proposed by Ragazzoni (53) for adaptive optics work. The schematic of this sensor is shown in fig. 4.12. It consists of two pyramids with a top angle of  $90^\circ$ . The incoming beam is focused on the top of the first pyramid which divides the beam into four. Eight folding mirrors and the second pyramid reflect the beam towards CCD camera through the lens.

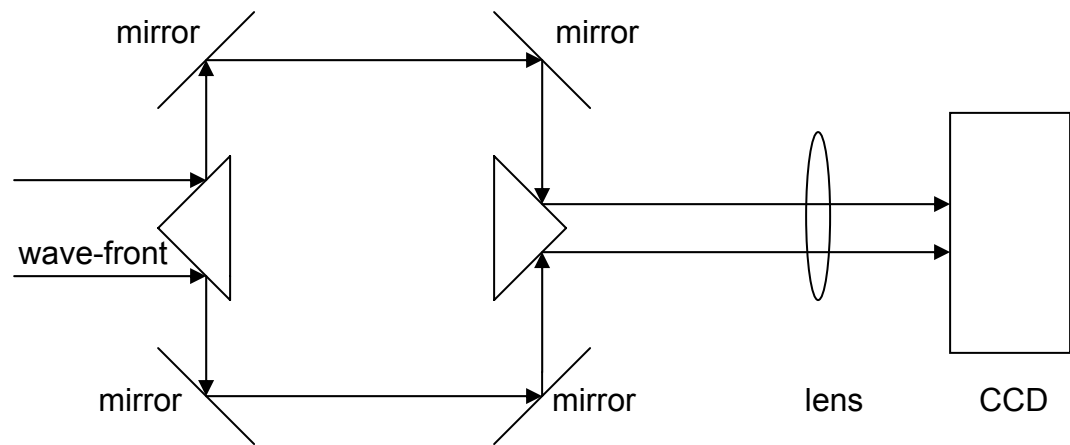


Fig. 4.12 Schematic of Pyramid sensor

The focal plane pyramid prism and the relay lens create four pupil images. From these images, with specially developed algorithms, the wave-front errors are computed.

Most of these methods are in different stages of development and deployment in the field and one or two methods like Shack-Hartmann method and curvature sensor method are already well tested. Therefore, Shack-Hartmann method has been chosen for the present technological development and Adaptive optics system study for 2.34M telescope. The easy availability of the lenslet array is another important factor. In section 4.3.1.1, details about computation of centroids and slopes in each sub-aperture is given. Following section describes the mathematical approach for the wave-front error computation from the S.H. slope data.



But it is computationally intensive. In this research work, centroiding algorithm is used for wave-front sensing. The aim of this exercise is to find out the speed of computation using the currently available processors; whether it is possible to achieve good accuracy in wave-front sensing within the limited time available time (loop time) for control of the adaptive mirrors.

As shown earlier, the difference between centroids  $C_1(x, y)$  and  $C_2(x, y)$  represents the average wave-front slope value at that sub-aperture. In this approach. each sub-aperture gives two measurements i.e., slope in x-direction  $S_x$  and slope in y-direction  $S_y$

The wave-front can be represented by the Zernike polynomial expansion,

$$W(x, y) = \sum_i A_i Z_i(x, y) . \quad (4.16)$$

Where the coefficients are the  $A_i$ , and the polynomial basis functions (modes) are  $Z_i(x, y)$ . The slope vector  $S$ , the mode coefficient vector  $A$  and the derivatives of the polynomial function  $B$  are shown below:

The x-slope and y-slope values at each sub-aperture are given by

$$\partial \frac{\partial W(x, y)}{\partial x l_m} = \frac{\sum_i A_i \partial Z_i(x, y)}{\partial x l_m} \quad (4.17)$$

$$\frac{\partial W(x, y)}{\partial y l_m} = \frac{\sum_i A_i \partial Z_i(x, y)}{\partial y l_m} \quad (4.18)$$

where subscript  $m$  implies evaluation at the coordinates  $(x_m, y_m)$ . This set can be represented by the familiar matrix equation  $[S] = [B] [A]$ , where the vector  $S$  is the slope vector and  $A$  is the mode coefficient vector as shown above.

The elements of  $[B]$  are the derivatives of the polynomial basis functions evaluated at the wave-front sensor sub-aperture positions. As noted by Tyson (45), there is a requirement that these elements are linearly independent, but it is not necessary that they are orthogonal.

#### 4.4.1 Polynomial fitting

As shown in the previous section, there are  $2M$  linear equations in the matrix form. To solve the equations for coefficients  $A_i$ , it is required an inversion of equation

$$[S] = [B] [A] \quad (4.19)$$

To find the parameters  $A_i$  that fit the series of basis functions  $[B]$  to the known or measured values  $S_i$ , involves the following method; When the number of equations  $2M$  less than the number of unknowns  $N$ , then it is an underdetermined system and can not be solved uniquely. When  $2M = N$ , the matrix  $[B]$  is square and, as long as it is not singular, it can be directly inverted. When  $2M > N$ , which is the general case, it is said to be over determined system. The problem reduces to calculating the values of unknowns such that the error between the measured and the actual values is small. An inverse for a non-square matrix cannot be found directly. An approximate solution can be determined based on a specific merit function. The merit function that represents a good determination is often a consideration, since there should be only one solution if not for real world errors such as noise. One method of estimating  $A_i$  is “Least Square Fitting”. This method finds the minimum of

$$\varepsilon = \sqrt{\sum_{i=1}^M \left[ S_i - \sum_{k=1}^N A_k B_{ik} \right]^2} \quad (4.20)$$

By differentiating ‘ $\varepsilon$ ’ w.r.t. each element  $A_k$  and setting  $d\varepsilon / dA = 0$ , a set of equations for the  $A$ ’s can be found. In matrix notation, this is equivalent to solving for the vector  $A$  by

$$[A] = [B^T B]^{-1} [B]^T [S]. \quad (4.21)$$

It is to be noted that  $[B^T B]$  is  $N \times N$  square matrix and can be inverted. The matrix  $[B^T B]^{-1} [B]^T$  is called pseudo-inverse of  $[B]$ . If  $[B^T B]$  is singular or if numerically close to singular, then inverse of  $[B^T B]$  is not possible. To get around this problem, the powerful method of singular value decomposition is used. Other numerical methods are Jacobi iterative method and Gauss-Siedel iterative

methods. But it is found that the matrix  $[B]$  does not approach singularity condition; hence ordinary matrix inversion could be used.

After matrix inversion one can easily find the coefficient matrix  $[A]$  by Eqn. 4.21. The error analysis can be done using Eqn. 4.20. Actual measurement of wave-front errors using 14 terms of Zernike polynomials using the above method is given in the next chapter

#### **4.5 On the choice of a suitable detector and its parameters for wave-front sensing**

In the real time atmospheric compensation system, the time required to complete one cycle of wave-front error measurement and control is in the order of 10 to 20 milliseconds. This time limit puts severe constraint on the image capture system based on CCD cameras or CMOS imagers as well as the computing power of the processor used for computation of wave-front errors and multi-loop control of mirror actuators.

##### **4.5.1 CCD based imaging system**

At present, CCD is the most successful imager because of low-noise characteristics and it is used in various applications. Typically, the CCD camera has 250000 pixels arranged in a square grid of 500 by 500 pixels. Even 2000 by 2000 pixel cameras are available. But the useful field available in an optical telescope is sometimes much higher. To cover wider fields, many CCDs can be butted together (kept side by side). Nagaraja Naidu has developed a mosaic CCD camera to cover wider fields (54). In scientific grade cameras, which are used for astronomical imaging, the charges generated in the CCD by the interaction of incoming photons are to be converted into digital numbers of 14 bits or more by the analog to digital converters (A / D converter) to have high accuracy. High accuracy converters need more time to convert the analog quantity. For high-speed operations, flash converters are normally used. But the

accuracy of these converters is limited to about 10 bits. Hence, there is a trade of between speed and accuracy. The CCD normally has only one, two or four read amplifiers and all the pixel charges are to serially pass through them. To increase the frame rates from the CCD, different read modes like frame transfer and kinetic modes are normally used. In these modes, half or less area of CCD is not sensitive to light by covering the area by an opaque material. Image is taken in one portion and shifted to the covered portion for storage and it is read from the storage area when the next integration starts. Recent development in the CCD is the interline-transfer CCD (IT-CCD). It has greatly reduced cell size, which has been major factor in the successful production of compact, low cost, and high quality image capturing equipment including video cameras, digital still cameras etc. A typical ¼ inch format, 380 k pixel IT-CCD for standard TV system contains 4.8 µm (H) x 5.6 µm (V) cells, and the 2/3 inch, 2 million pixel IT-CCD for High Definition Television (HDTV) contains 5 µm square cells. Reduction of cell size further can create other problems (55).

CCDs used in some of the wave-front sensors developed earlier used a 64 by 64 or 32 by 32 pixel CCD and the recent experiments used 128 by 128 pixels, thus limiting the number of lenslet arrays that can be used for wave-front sensing.

#### **4.5.2 Evaluation and selection of CCD based camera system for wave-front sensor**

CCD sensors are increasingly being used for wave-front sensing because of their high quantum efficiency, low noise and compatible with digital processing units. As there are many variations in CCD systems, a brief discussion is given below to select a suitable one.

##### **4.5.2.1 Custom built CCDs**

Some times the geometry and other constraints does not allow commercially available CCDs to be used in the wave front sensor. For the new

wave-front sensor developed for Multiple Mirror Telescope (MMT) of Steward Observatory, both the CCD and the lenslet were custom built (56) so that the pitch of the lenslet array was an integer multiple of the CCD pixel size – one subaperture lens is commensurate with a 6 x 6 subarray of CCD pixels. This CCD is a thinned, back-illuminated device with a square 80 x 80 array format and 24  $\mu\text{m}$  x 24  $\mu\text{m}$  pixels. It is found that CCDs with less than 100 x 100 pixels are always custom made. The cost and delivery time of custom made devices are always higher than the commercial ones.

#### **4.5.2.2 Scientific grade, cooled CCD**

A high speed Image capture system is a very crucial component of the wave-front sensor. For getting data from telescope using CCDs, one needs a scientific grade device that has almost zero defects, which is costly and the CCD is to be cooled to about  $-100$  deg C to eliminate the thermal noise that can accumulate and mask the weak signal received from faint stars. Cooling the CCD to this low temperature creates the problem of moisture condensation on the detector; hence the device has to be housed in a high vacuum cryostat. Jacob et.al., have designed and fabricated a high vacuum cryostat for CCDs which uses liquid nitrogen for cooling [57]. Storing and using liquid nitrogen for cooling the CCDs needs expertise. On the other hand, cooling the CCD to around  $-60$  deg C with Peltier cooler is much simpler. In wave-front sensing application, speed of operation is the main criteria. The scientific grade CCD output is normally digitized to more than 14 bits. For high accuracy, analog to digital conversion technique like correlated double sampling is employed and the conversion time is inherently higher. For the speckle observation at VBT, we have used two fast image acquisition systems. The first one is based on a peltier cooled, intensified CCD system and the second one is based on low light level CCD which does not need image intensification. The suitability of the above systems was evaluated for wave-front sensing and the following pages give details about that.

### 4.5.2.3 Intensified, Peltier cooled CCD

An intensified CCD camera is routinely used for Speckle observations at Vainu Bappu Observatory for many years. It has high-speed image acquisition features with programmable integration times of a few milliseconds to seconds. The CCD used here is a EEV chip with 576 x 378 pixels. The micro channel plate (MCP) intensifier is fibre-optically coupled to the CCD array. The proximity focused MCP has photomultiplier like UV - NIR response. Because of the architecture of CCD, even to read 10 by 10 pixel occupied by a single star, one has to read the whole device. This increases the reading time, thus limiting the number of frames that can be read with these systems. Frame transfer devices that store the image on chip in one half of the chip improves the speed but reduces the imaging area by half. The region of interest, say 100 x 100 pixel, can be read, in this mode, the data in the region of interest alone is digitised by the analog to digital converter after the charge is read from CCD, the remaining area charges are dumped out from CCD after reading without being digitised. This CCD has 1 MHz controller speed. As one needs a system that can capture at least 100 frames per second, this camera if used in frame transfer mode, may just meet the speed requirement.

If  $T_r$  is the time taken to read the CCD,

$$T_r = N_x * N_y (t_{sr} + t_v) + N_x * t_i \quad (4.22)$$

Where  $N_x$  and  $N_y$  are the number of pixels in x and y direction of CCD,  $t_{sr}$  is the time required to shift one pixel out of shift register

$t_v$  is the time taken to digitise one pixel

$t_i$  is the time to shift one line into shift register

For 100 by 100 region,

$$\begin{aligned} T_r &= 100 * 100 (0.2+0.9) + 100 * 15 \\ &= 0.0125 \text{ sec.} \end{aligned}$$

i.e., about 80 frames per second can be read from the CCD. This time is to read and digitize the required region alone and if one takes into account the discarded pixels, the time will be still more.

But the camera software as supplied by the manufacturer is most suited for high speed image capture which writes the data in the disk for later off-line processing; extensive software modification is required for use in real time control.

#### **4.5.2.4 Low light level CCD camera**

One of the very recent developments in the already matured CCD technology is the Low Light Level CCD (LLLCD) manufactured by Marconi Applied Technology of U.K. It has photon counting capabilities without requiring an image intensifier. It is a frame transfer CCD; it utilizes a unique electron multiplying structure that is built into the silicon. This enables charge from each pixel to be multiplied on the sensor before it is read out. The gain of the camera can be varied from unity up to a thousand times. The LLLCD is manufactured utilizing standard CCD fabrication techniques. The unique feature of this device is an electron multiplying structure that has been inserted between the end of the shift register and the output amplifier, and is referred to as the gain register, as shown in figure 4.13. The gain register is operated at much higher voltage than the rest of the CCD creating ionization. Impact ionization generates new electrons, i.e. multiplication or gain. Andor Technology Limited, an U.K. company has made a high speed camera system using this chip. This CCD is used as wave-front camera and the next chapter contains details about the development of LLLCD based wave-front sensor.

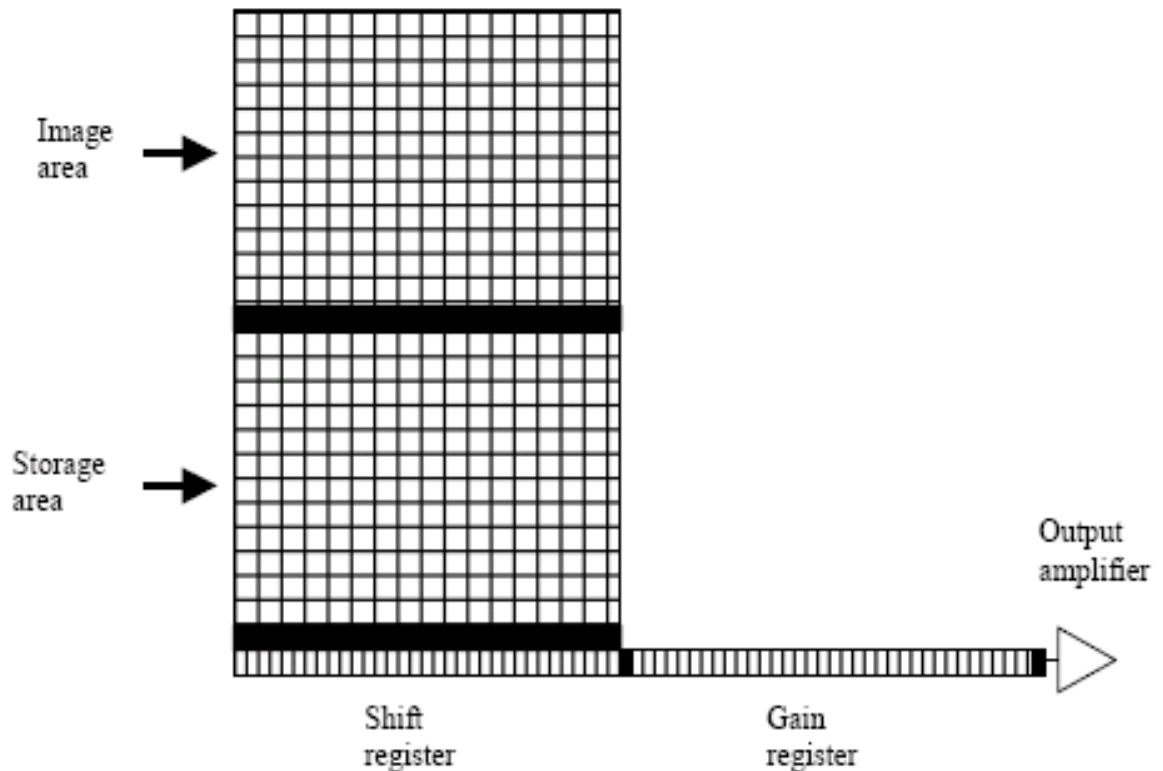


Fig. 4.13 Schematic of low light level CCD as provided by the manufacturer.

In intensified CCD, the output of the micro channel plate (MCP) is coupled to CCD either by fibre optic bundle or through lenses. As there is no MCP and the associated high voltage of about 10000 V required for its operation and also there is no coupling problem, this device is more rugged with minimal components. The advantage of this LLLCD is that at low light levels, it can have single photon detection capability comparable to that of the intensified CCDs. The detector is peltier cooled to -65 deg C, and with water circulation, it can reach -80 deg C. Hence, the camera system gives noise performance comparable to the liquid nitrogen (LN<sub>2</sub>) cooled cryostats without the hassles associated with use of LN<sub>2</sub>. Architecture wise, a LLLCD is similar to a regular CCD except for the extra gain stage register; hence, the high-speed operation is comparable to that of ICCD. Like other CCDs, it has full frame, frame transfer and kinetic mode of operation.

#### **4.5.2.5 Video rate camera and Frame grabbers**

Commercially available CCDs which give RS120 video format was not considered as the frame grabbers give a fixed time of 20 milliseconds per frame and the accuracy of the digitised data usually averages to 6.5 bits. Recent developments in the image sensor field are the CMOS imager. As the architecture of the device is best suited for high speed applications, the CMOS imager was chosen for image acquisition system.

#### **4.5.3 CMOS based imaging system**

The main advantages of CMOS imager are low system cost, high light sensitivity, reduced blooming or smearing effects, and use of technology which enables integration of millions of transistors in the same chip. It makes possible integration of complex analog, digital, and mixed signal processing on the same chip as the image sensor. CMOS realization enables parallel and random sensor access. One can implement very efficiently those image processing algorithms that are based on processing neighboring pixels. This feature can contribute significantly to data reduction, which is an important requirement in many image processing application. These types of devices are called Smart sensor arrays (58). The development of CMOS imager has eliminated some of the shortcoming of the CCD sensors. CCD needs different DC voltages of different polarity. The fabrication process of CCD is much involved, hence the yield from IC fabrication runs are low. Scientific grade CCDs which are used for accurate measurements, costs too much to be used for low cost applications. The CMOS technology based imagers are being developed now. The well matured fabrication technology of microprocessors and memory, the Complementary Metal Oxide Semiconductor (CMOS) fabrication technology was used for making the imagers, thus making it possible to have electronic Camera-on-A-Chip (59). Unlike the architecture of CCD, which is serial, the CMOS device pixels have random

access architecture, like memories thus, if 5 by 5 pixels have to be read, and then only 25 pixel readouts are required. For comparison, in a CCD device having 100 by 100 pixels, to read a sub-region of 5 by 5 pixels, the entire device's 10000 pixels are to be read thus severely limiting the speed. The CCD pixel just acts as storage of charge where as in CMOS imager pixels are active where an amplifier is normally incorporated in the pixel to multiply the signal; hence the pixel is appropriately named as active pixel sensor (APS). As the CMOS imager is developed only recently and it has architectural features best suited for high speed control applications, it was chosen as the appropriate low cost camera by characterizing and using them (60) in the wave-front sensor for real time aberration correction system.

CMOS imager is a recent development in the image sensor field. It is a monolithic solid-state camera chip with random addressability and logarithmic response. Random addressing of pixels enables frame speeds in the order of thousands, satisfying an important requirement of wave-front sensor. These types of imagers operate on single power supply of 5 V unlike CCDs that require 3 or 4 supplies. Full digital operation is possible with built-in analogue to digital converters. Section 4.5.2 gives detailed comparison of CMOS imager with CCD. A Shack-Hartmann lenslet array based wave-front sensor was designed and fabricated with CMOS as imager. Using the hints provided by the chip manufacturer, fast image acquisition software was developed. As there is no intensification of incoming light source, this system can be used for bright sources only otherwise, an image intensifier is to be attached in the front of the camera for observation of faint sources. Detailed description of Shack-Hartmann wave-front sensor developed using CMOS sensor is given in the next chapter.

#### **4.5.4 APD based wave-front sensor**

Avalanche photo diode (APD) is a good detector for wave-front sensing. APDs have 70% or more quantum efficiency and output a digital pulse of 100 nsec after photon detection giving very high frame rate. Number of counts from

the detector is very high giving a very good signal to noise ratio. The dark current for APD is less. Short integration time of about 200 micro second is possible. The only drawback is the smaller number of pixels available. European Southern Observatory wave-front sensor is based on APD and the curvature sensor. In 2001, Reinhold (61) did research on using specially designed CCD for wave-front sensing

#### **4.6 Camera control computer and wave-front computation and display computer**

CMOS imager and Low Light Level CCD are capable of at least meeting the speed requirement of a camera system for wave-front sensing. Normally, a PC controls these cameras with one of the standard interface cards. It is found that the interface standard become obsolete in a couple of years and there is a constant need to upgrade hardware interface, software drivers etc. The two camera systems that have been chosen for a detailed study have Peripheral Component Interconnect (PCI ) bus interface thus providing high speed input / output (I /O) throughput.

Normally, the camera manufacturer provides camera control software in the executable file format. The software has setting for different parameters for data gathering and collects the required image and stores the image in the system disk in one of the standard image formats like BMP, TIFF, PNG etc. One has to access the data from the disk only. This operation, severely limits the speed with which the wave-front error can be computed for real time control. This deficiency was rectified by developing custom camera control software for CMOS imager so that the acquired image is immediately available for further processing by storing the image in the computer memory.

#### **4.7 On the choice of Tip-tilt and deformable mirror systems for wave-front error compensation**

The error in the in-coming wave-front can be divided into two parts. (i) Tilt in the wave-front and (ii) the high spatial frequency corrugation. If wave-front tilt is measured and corrected, then more than 80% of the error can be removed. Contribution of high frequency errors in the wave-front is less. Once the tilt error component and the high frequency error components are resolved, separate mirrors can be used to compensate them. Tilt mirrors based on piezoelectric actuators, are highly reliable. When voltage is applied across the piezoelectric stack, depending on the magnitude of the voltage, there is a change in the length. Linear movements in the range of a few tens of micrometers with resolution of a nanometer are currently available.

For high frequency wave-front error correction, continuous faceplate mirrors activated by piezoelectric actuators or its variants like Remnant Poled Lead Magnesium Niobate (PMN:RP) are used. Typical stroke of 4  $\mu\text{m}$  with a resolution of 2 nm is possible. The cost of these systems are very high. Recent development in MEMS based adaptive mirror has reduced the cost considerably. MEMS based adaptive mirror for 37 channel costs about \$5000, factor of 20 less than the PMN:RP based mirrors. The low cost of the membrane mirror was made possible by the mass production technologies used in semiconductor fabrication.

#### **4.8 Suitability of low cost components**

The distortion created by earth's atmosphere on star image was known from Isaac Newton time onwards. Successful use of closed loop servo controls during world wars for gun control prompted Babcock to look for a solution and the scheme he has given could not be implemented for a long time. U.S. Military has done a major part of the research for real-time control of the wave-front. Their effort was to get clear photographs of man-made satellite and to beam powerful laser beams on enemy targets to destroy them. The latter application is the so

called “star war” program. Tip-tilt mirrors based on piezoelectric actuators which can work at kilo-hertz rate were developed. For real time control of complicated wave-fronts, custom made computers working in parallel (64) that can capture images at tens of millisecond intervals and to compute the errors within a few milliseconds, were developed. For high frequency error corrections, adaptive mirrors (AM) or deformable mirrors (DM), which can create any desired surface like plane, parabola or any arbitrary surface, were developed. Roddier (62) comments on this development as the unfavourable consequence because military applications led towards expensive technological solutions not directly suitable to astronomical applications and sometimes led to misconceptions. A common misconception is that very large number of sensors and actuators are required to obtain images close to the diffraction limit of an optical telescope. The number of actuators required for correction depends on the aperture of the telescope and the seeing parameter called Fried’s parameter. For a telescope of aperture size  $D$  and Fried’s parameter  $r_o$

$$\text{No. actuator required} = \left(\frac{D}{r_o}\right)^2 \quad (4.23)$$

For a 2 m aperture telescope, and  $r_o$  of size 10 cm, number of actuator required is 400. All these channels are to be operated in close loop control. Earlier DMs were made with piezoelectric actuators stacked together. On top of each actuator a small reflecting mirrors is pasted. These small mirrors can be moved up and down by voltage control, thus producing any desired surface. The cost of 1 actuator with control electronics is about \$ 2000; hence for a small telescope of 2 m size, DM mirror system will be costing about \$800000. Even if sufficient money is provided, the technical complexity of making the system work is enormous. Roddier et.,al, (62) have used only two Zernike modes (x and y tilt) and successfully corrected the image quality of an aberrated image to a satisfactory level at Infra red wavelengths. Later, they had extended this to 9 Zernike terms.

Recent advances in micro electro opto-mechanical system (MEOMS) fabrication have reduced the cost of the DM which is the crucial component of wave-front correction. But with the currently available technology, only mirrors

with 50 actuators are commercially available and there are only one or two firms in the world which are making these mirrors. A DM with 37 actuators was procured, the details of which is given section 5.2

On the computational front, there is a many fold increase with the processing power, at much lower cost than the dedicated parallel computers. Low cost CMOS imagers which have random access of pixels can increase the number of frames that can be acquired. The availability of low cost components prompted us to research upon these technological challenges and to provide a low cost solution for the on-line A.O. correction.

#### **4.9 Close Loop time requirement**

Control frequency for wave-front correction is given by the Greenwood frequency as shown in eqn. 3.6. It depends on the seeing parameter  $r_0$ , the wavelength of observation and prevailing wind velocity. For a given refractive index change, a large wind velocity moves this disturbed image across the telescope pupil more, forcing one to go for higher speed correction. As the seeing depends on the wavelength, and infra red seeing is better than the visual band; hence infrared detectors can be used for wave-front sensing, reducing the time requirement of the wave-front sensor. Typically, the loop time can vary from 10 to 50 milliseconds depending on the parameters mentioned above.

#### **4.10 Control computer for adaptive mirrors**

For Closed loop error correction, piezoelectric actuator based tip-tilt mirror system and low cost MEMS based deformable mirror systems are possible choices. The number of actuators required is theoretically a few hundreds, but they are not commercially available. Low cost mirrors with 37 and 50 channels are presently available. Each channel control can be thought of a closed loop feed back control system. Hence computers with high input-output throughput are required to match with the system parameters.

#### **4.11 AO system for online wave-front error measurement and correction system for VBT**

For designing a AO system for VBT, following sub systems selection criteria was adopted.

- The Shack-Hartmann lenslet array for wavefront sampling
- Centroiding algorithm for wave-front slope calculation
- Zernike polynomial representation for wave-front error calculation
- CMOS imager as the high speed camera system for wave-front sensor
- Three Piezo-electric actuator based tilting mirror for tip-tilt correction
- MEMS based DM for high frequency error correction
- Personal Computer for the wavefront sensor as well as adaptive mirror control.

The above broad category of selection is arrived based upon survey of literature to implement a low cost system. The actual systems with their size and ranges were determined after suitable optical design of the system. Such a design for VBT is described in the next chapter.

## Chapter 5

### Optical design and selection of components for wave-front measurement and closed loop correction system for VBT

#### 5.1 Introduction

The different approaches for wave-front sensing, algorithms for wave-front error calculations and a few types of imaging cameras which can be used for wave-front error measurement are explained briefly in the earlier chapter. Based on the measured wave-front errors, on-line correction has to be done. Adaptive mirrors suitable for wave-front control and the related computer control requirements were also looked into. In following chapters, design of a wave-front error measurement and correction system is explained.

A typical layout of a closed loop image correction system is shown in fig. 5.1. Referring fig. 5.1, T is the telescope and its Cassegrain focus CF is shown. Normally, a science camera is mounted at this focus to obtain images of star. As explained in the previous chapters, this image is distorted by the atmosphere. Hence, an on-line correction system is designed and implemented. The beam of light, after the focus, is made into a parallel beam by the lens L1 and the tip-tilt mirror TTM reflects the beam towards the deformable mirror DM and the lens L2 forms the image of the star in the science camera SC. A portion of this beam is borrowed for on-line correction by beam splitter BS and reaches the wave-front error measurement system. The error measurement system consists of Shack-Hartmann lenslet array SH and at the focus points of the lenslet array the fast CMOS or CCD wave-front camera is kept. The images are acquired in 10 to 20 msec integration time by the PC. Optical errors in the wave-front are computed by the PC. The errors are in two broad categories; the tilt errors and the high frequency corrugation errors. The tilt error is corrected by the tilt mirror TTM and the high frequency errors are corrected by the deformable mirror DM.

For the proper selection of tip-tilt mirror and the deformable mirror, the maximum tilt angles required and the maximum depth required of deformable mirror is to be known. Hence an optical design of the system was carried out. The 2.34M telescope is taken as the telescope for on-line wave-front error measurement and correction.

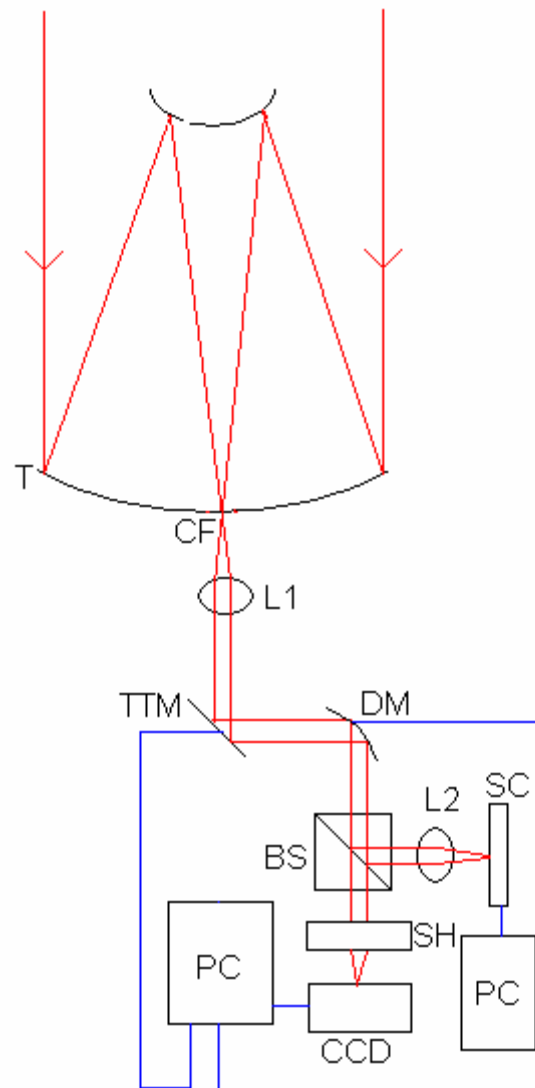


*Fig. 5.1 A typical layout for closed loop wave-front error measurement and correction system for 2.34M Vainu Bappu Telescope*

## 5.2 Optical design for closed loop error measurement and correction system for VBT

For 2.34M VBT, a complete optical configuration design for an on-line correction system was worked out. The design was carried out using ZMAX package. This design gives the stroke lengths and tilts required for correction of aberrated input wave-fronts. Based on these results, adaptive mirror and tip-tilt mirror are chosen for closed loop wave-front correction. The following pages outline the design methods:

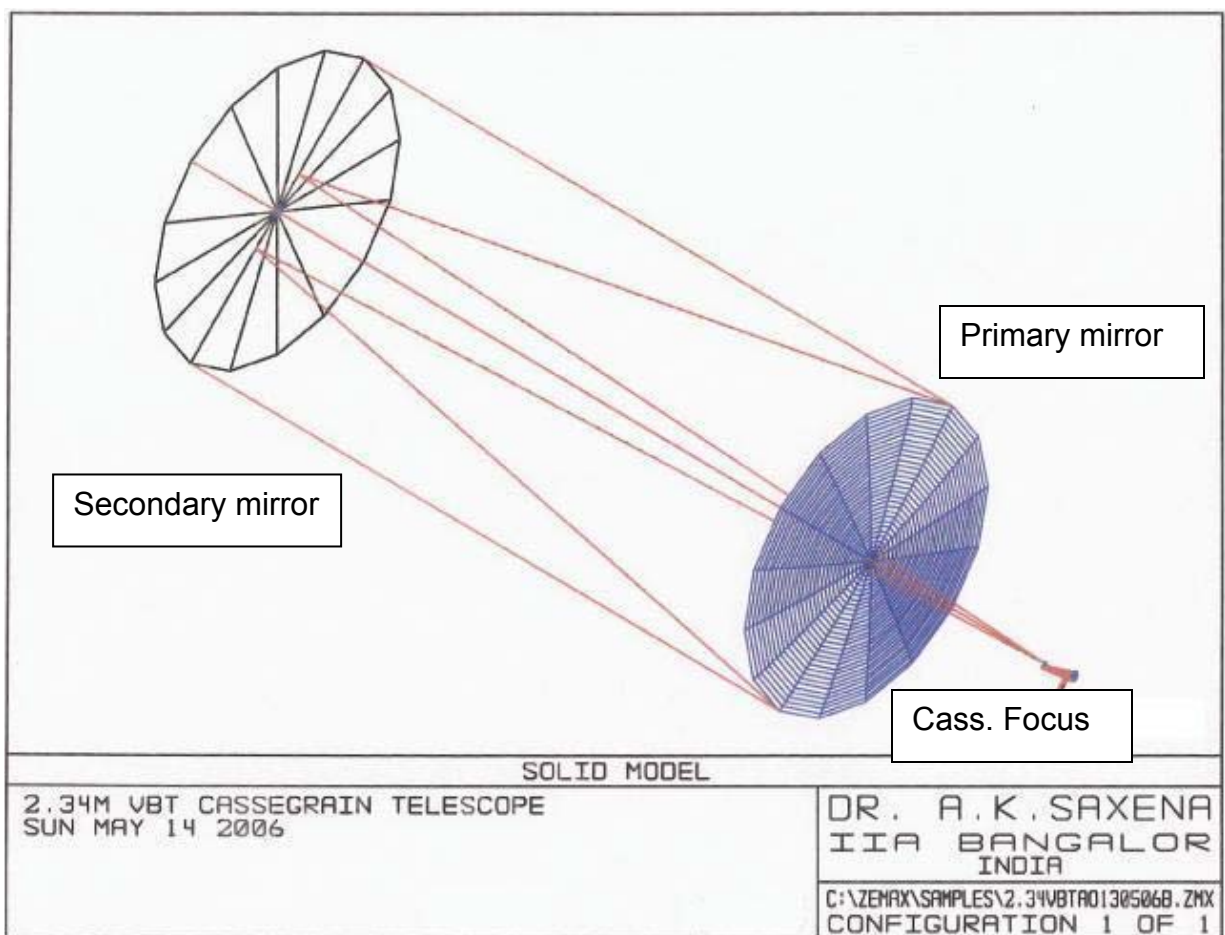


Fig. 5.2 The solid model of Cassegrain mode of 2.34M VBT

A solid model of optical system of 2.34M VBT in Cassegrain mode is shown in fig. 5.2. The primary mirror of 2.34M diameter and secondary mirror of 0.575 m diameter and the Cassegrain focus are also shown in the figure.

```

DATE          : SUN MAY 14 2006
FILE NAME     : C:\ZEMAX\SAMPLES\2.34VBT\0130506B.ZMX
TITLE        : 2.34M VBT CASSEGRAIN TELESCOPE
              : NOTES...
              :
UNITS         : MILLIMETERS
EFL          : -11603.1          BFL          : -15915.7
TOTAL TRACK  : 7605.33
WORKING F/#  : 5.00069
IMAGE HEIGHT : 4.05023          MAGNIFICATION: 0
ENTR PUP DIA : 2340            EXIT PUP DIA : 6.7889
ENTR PUP POS : 5678.94         EXIT PUP POS : -33.8611
FIELD TYPE   : ANGLE IN DEGREES
#            X-VALUE          Y-VALUE          WEIGHT
1            0.000000         0.000000         1.000000
2            0.010000         0.000000         1.000000
3            0.020000         0.000000         1.000000
WAVELENGTHS IN MICRONS:
#            VALUE           WEIGHT
1            0.650000         1.000000

```

*Table 5.1 Entrance and exit pupil and focal lengths of VBT*

- Important data of optical system of 2.34M are shown in Tables 5.1 and 5.2. Here, EFL is the effective focal length and BFL is the back focal length. The entrance and exit pupil diameters are also given.

System/Prescription Data

File : C:\ZEMAX\Samples\2.34vbtal130506b.ZMX  
 Title : 2.34M VBT Cassegrain telescope  
 Date : SUN MAY 14 2006

LENS NOTES:

Notes...

GENERAL LENS DATA:

Surfaces : 17  
 Stop : 2  
 System Aperture : Entrance Pupil Diameter = 2340  
 Glass Catalogs : SCHOTT  
 Ray Aiming : Off  
 Apodization : Uniform, factor = 0.00000E+000  
 Effective Focal Length : -11603.05 (in air at system temperature and pressure)  
 Effective Focal Length : -11603.05 (in image space)  
 Back Focal Length : 19727.77  
 Total Track : 7605.331  
 Image Space F/# : 4.95857  
 Paraxial Working F/# : 4.95857  
 Working F/# : 5.000687  
 Image Space NA : 0.1003268  
 Object Space NA : 1.169999e-007  
 Stop Radius : 1170  
 Paraxial Image Height : 4.05023  
 Paraxial Magnification : 0  
 Entrance Pupil Diameter : 2340  
 Entrance Pupil Position : 5678.943  
 Exit Pupil Diameter : 6.788903  
 Exit Pupil Position : -33.86106  
 Field Type : Angle in degrees  
 Maximum Field : 0.02  
 Primary Wave : 0.65  
 Lens Units : Millimeters  
 Angular Magnification : -344.6801

Fields : 3  
 Field Type: Angle in degrees  

#	X-Value	Y-Value	Weight
1	0.000000	0.000000	1.000000
2	0.010000	0.000000	1.000000
3	0.020000	0.000000	1.000000

Vignetting Factors  

#	VDX	VDY	VCX	VCY	VAN
1	0.000000	0.000000	0.000000	0.000000	0.000000
2	0.000000	0.000000	0.000000	0.000000	0.000000
3	0.000000	0.000000	0.000000	0.000000	0.000000

Wavelengths : 1  
 Units: Microns  

#	Value	Weight
1	0.650000	1.000000

SURFACE DATA SUMMARY:

Surf	Type	Comment	Radius	Thickness	Glass	Diameter	Conic
OBJ	STANDARD		Infinity	Infinity		0	0
1	STANDARD		Infinity	5678.943		2343.965	0
STO	STANDARD		-15021	-5678.943	MIRROR	2340.032	-1
3	STANDARD		-4880	7345.331	MIRROR	575.5022	-2.769377
4	STANDARD		Infinity	260		21.07979	0
5	COORDBRK		-	0		-	-
6	STANDARD		-520	-265	MIRROR	74.55612	-1
7	COORDBRK		-	0		-	-
8	STANDARD		Infinity	0	MIRROR	20.61137	0
9	COORDBRK		-	0		-	-
10	STANDARD		Infinity	225		20.61086	0
11	COORDBRK		-	0		-	-
12	STANDARD		Infinity	0	MIRROR	38.00633	0
13	COORDBRK		-	-175		-	-
14	COORDBRK		-	0		-	-
15	PARAXIAL		-	-100		52.04415	-
16	STANDARD		Infinity	0.2512401		8.115883	0
IMA	STANDARD		Infinity			8.134787	0

SURFACE DATA DETAIL:

```

Surface OBJ      : STANDARD
Surface 1       : STANDARD
Surface STO     : STANDARD
Surface 3       : STANDARD
Surface 4       : STANDARD
Surface 5       : COORDBRK
  Decenter X    :          0
  Decenter Y    :          27
  Tilt About X  :        -5.96
  Tilt About Y  :          0
  Tilt About Z  :          0
  Order        : Decenter then tilt
Surface 6       : STANDARD
Surface 7       : COORDBRK
  Decenter X    :          0
  Decenter Y    :        -27
  Tilt About X  :         -5
  Tilt About Y  :          0
  Tilt About Z  :          0
  Order        : Decenter then tilt
Surface 8       : STANDARD
Surface 9       : COORDBRK
  Decenter X    :          0
  Decenter Y    :          0
  Tilt About X  :         -5
  Tilt About Y  :          0
  Tilt About Z  :          0
  Order        : Decenter then tilt
Surface 10      : STANDARD
Surface 11      : COORDBRK
  Decenter X    :          0
  Decenter Y    :          0
  Tilt About X  :       -37.5
  Tilt About Y  :          0
  Tilt About Z  :          0
  Order        : Decenter then tilt
Surface 12      : STANDARD
Surface 13      : COORDBRK
  Decenter X    :          0
  Decenter Y    :          0
  Tilt About X  :       -37.5
  Tilt About Y  :          0
  Tilt About Z  :          0
  Order        : Decenter then tilt
Surface 14      : COORDBRK
  Decenter X    :          0
  Decenter Y    :          0
  Tilt About X  :          0
  Tilt About Y  :          0
  Tilt About Z  :          0
  Order        : Decenter then tilt
Surface 15      : PARAXIAL
  Focal length  :         100
  OPD Mode     :          0
Surface 16      : STANDARD
Surface IMA     : STANDARD

```

COATING DEFINITIONS:

Table 5.2 Input data for Zemax design software

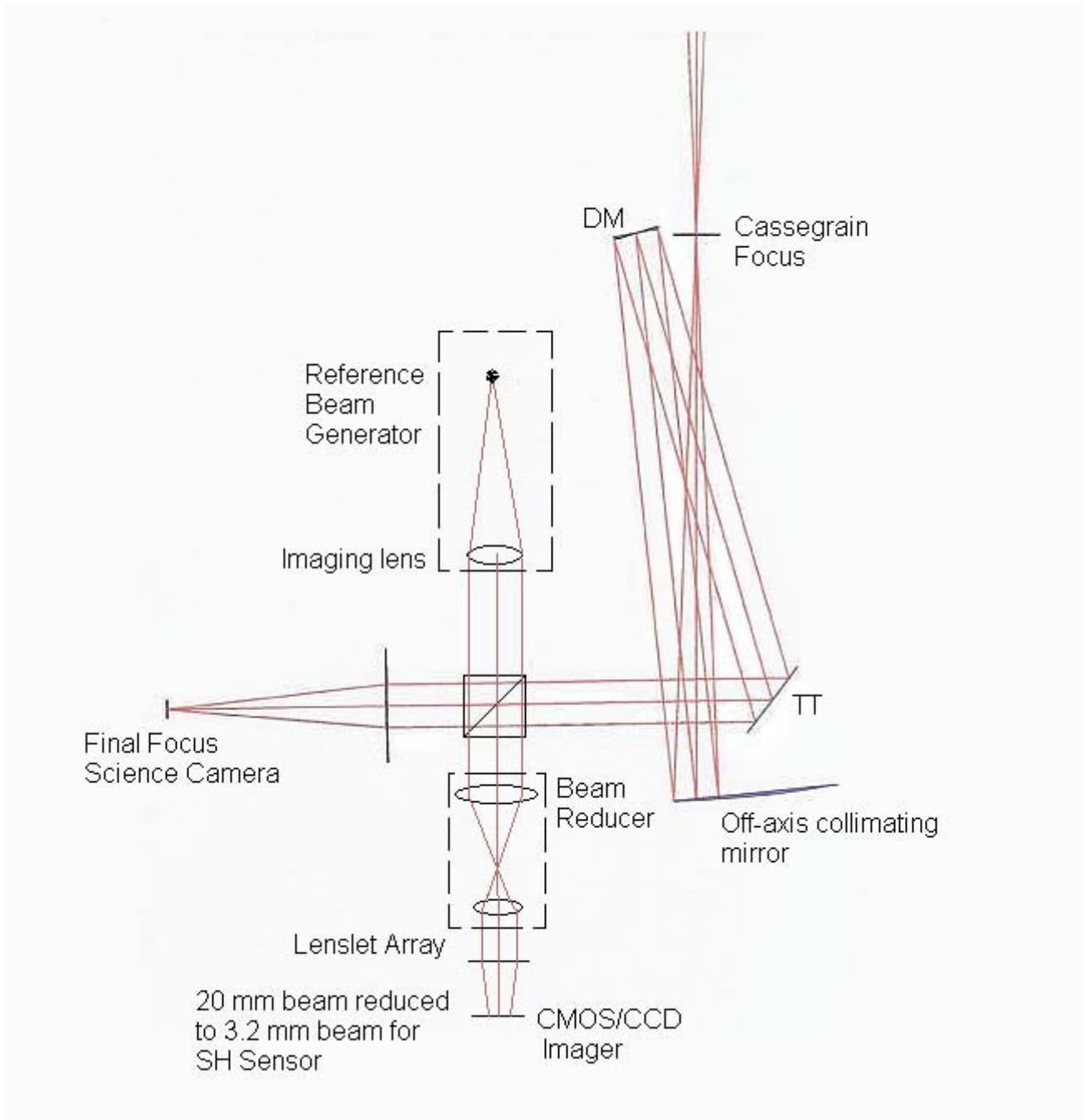


*Fig. 5.3 Ray diagram of the optical error correction system*

- In Fig. 5.3, the Cassegrain focus point telescope is marked and the diverging beam after the focus is made into a parallel beam by the off axis collimating mirror. The parallel beam is then reflected by the deformable mirror and then by the tip-tilt mirror. These two mirror surfaces are

controlled by computer, based on the wave-front sensor output, such that a conjugate surface of the aberrated wave-front is created. The corrected beam is focused on to the Science camera by the imaging lens.

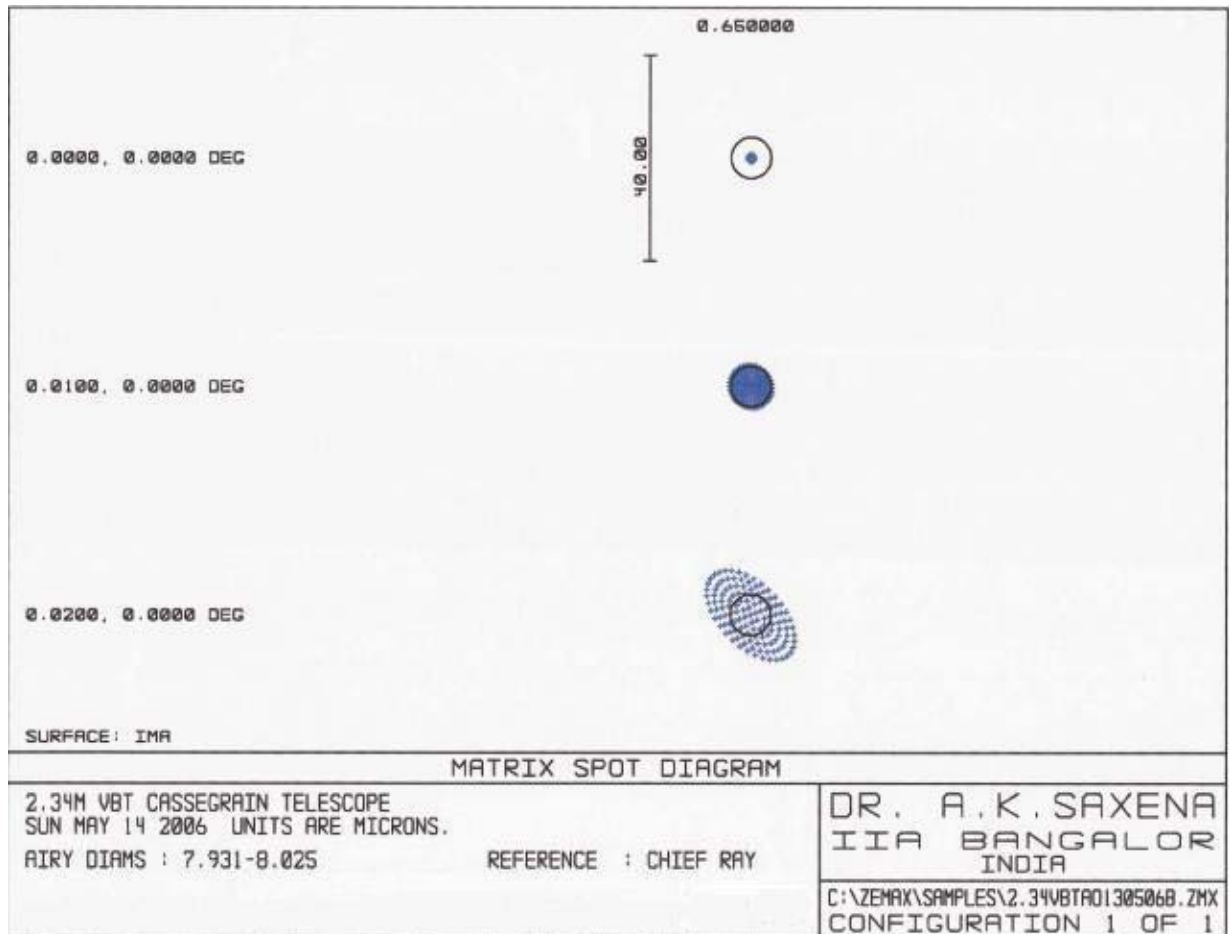


*Fig. 5.4 Airy's disk for on axis and 0.01 and 0.02 deg off axis ray*

- A portion of the corrected beam is borrowed by beam splitter and it is fed to wave-front sensor for error measurement. A beam reduction unit reduces the beam size of 20 mm to 3.2 mm for the Shack-Hartmann camera.

- Fig. 5.4 shows spot diagram of images formed for
  - On axis image,
  - For off-axis ray with a shift of 0.01 deg,
  - Off-axis ray with a shift of 0.02 deg.

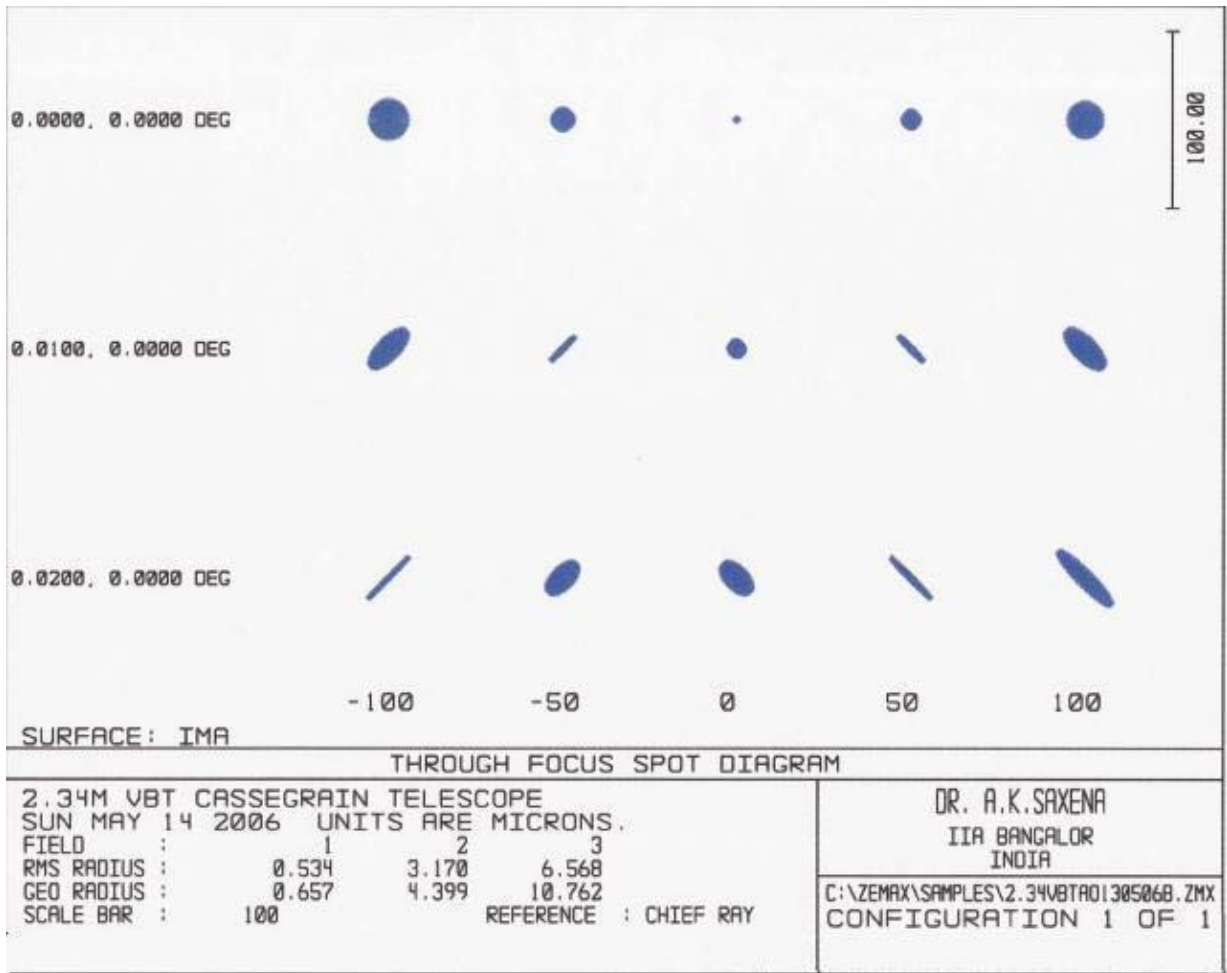
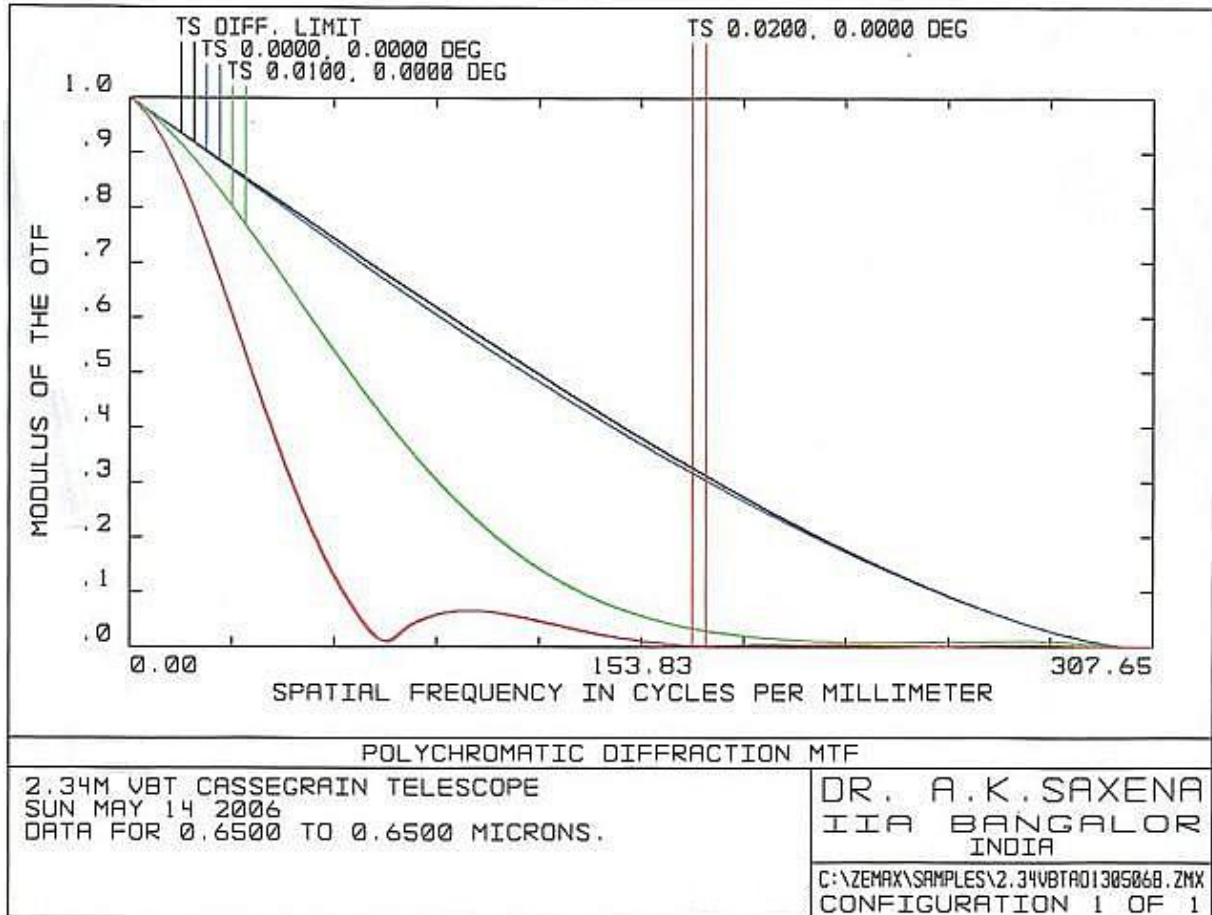


Fig. 5.5 Through focus spot diagrams for the error condition

- Fig. 5.5 shows the through focus spot diagrams for the same 3 input beam conditions as mentioned before.
- Fig. 5.6 shows polychromatic diffraction MTF for the same 3 input beam conditions
- Fig. 5.7 shows the encircled energy

- Fig. 5.8 shows the aberrations produced due to entrance pupil



*Fig. 5.6 Diffraction pattern for three input wave conditions*

- Fig. 5.9 shows the wave-front computed for on axis beam
- Fig. 5.10 shows the PSF for on-axis beam.
- Fig. 5.11 shows the wave-front for 0.01 degree shift of input beam
- Fig. 5.12 shows the PSF for 0.01 deg. shift of the input beam.

- Fig. 5.13 shows the wave-front for 0.02 degree shift of input beam
- Fig 5.14 shows the PSF for 0.02 deg. Shift of the input beam.
- Zernike coefficients computed up to 37 terms are given in Table 5.3

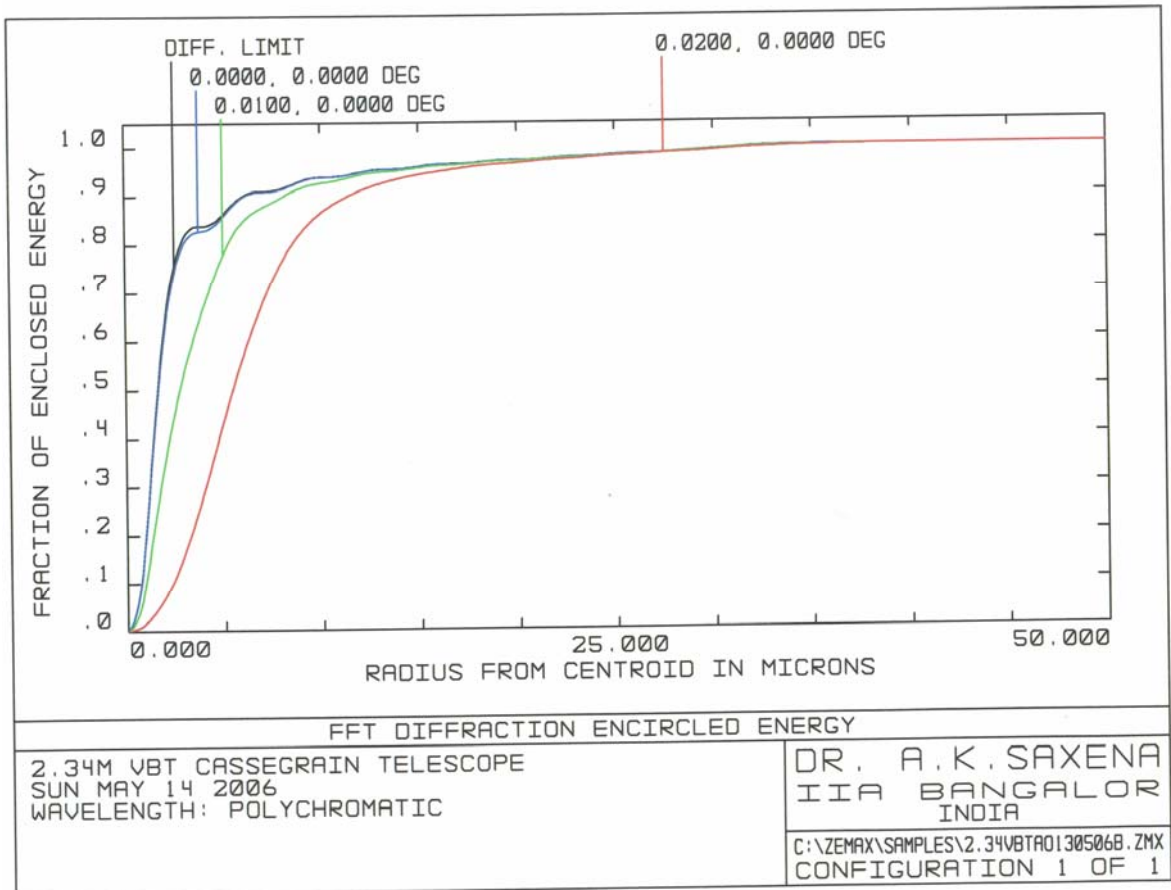
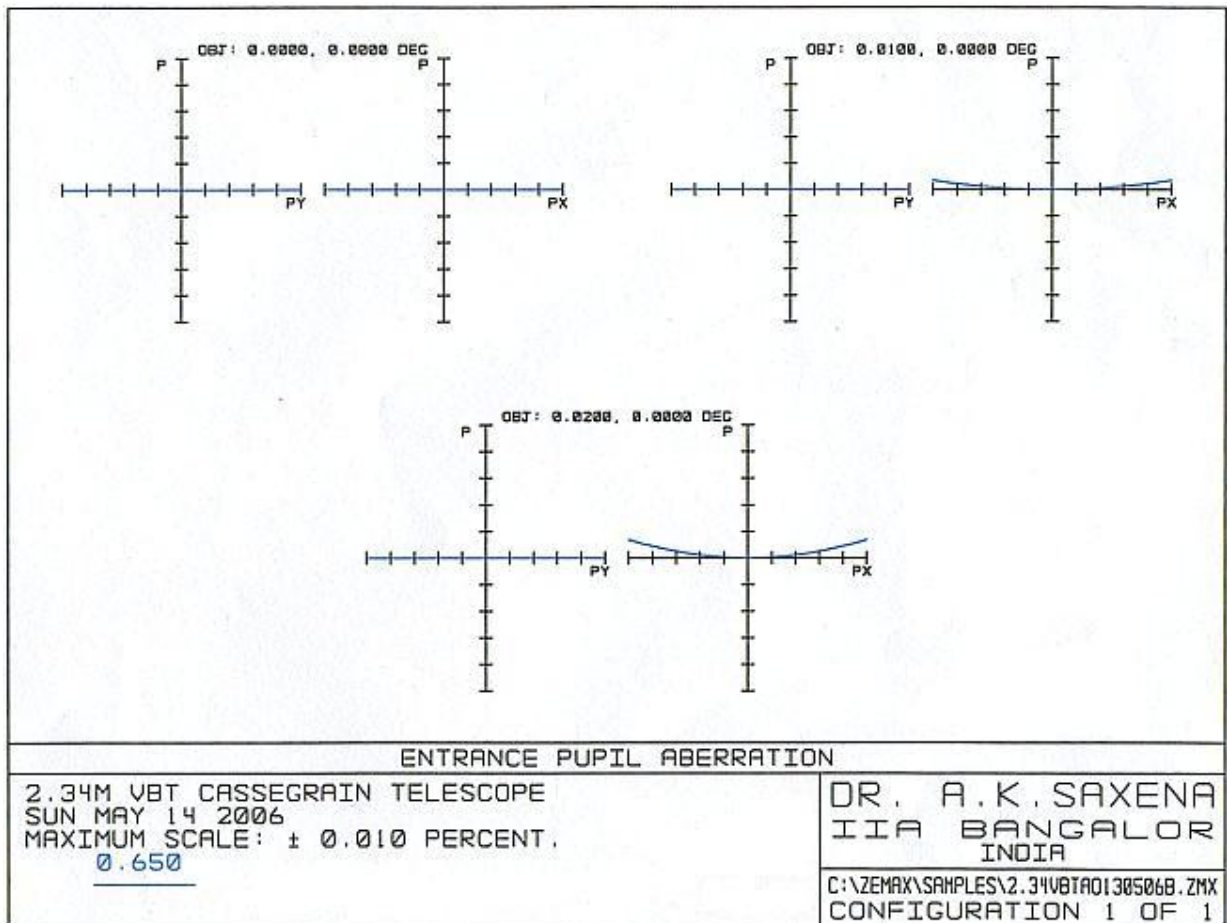


Fig. 5.7 Enclosed energy profiles



*Fig. 5.8 Entrance pupil aberration for 0.01 and 0.02 deg*

It is found from the above results that the peak to valley wave-front error is 1.3038 waves. Based on this input, a study was conducted to find out suitable control mirrors that are commercially available for the closed loop correction. The characteristics of the adaptive mirrors chosen are given in the subsequent sections.

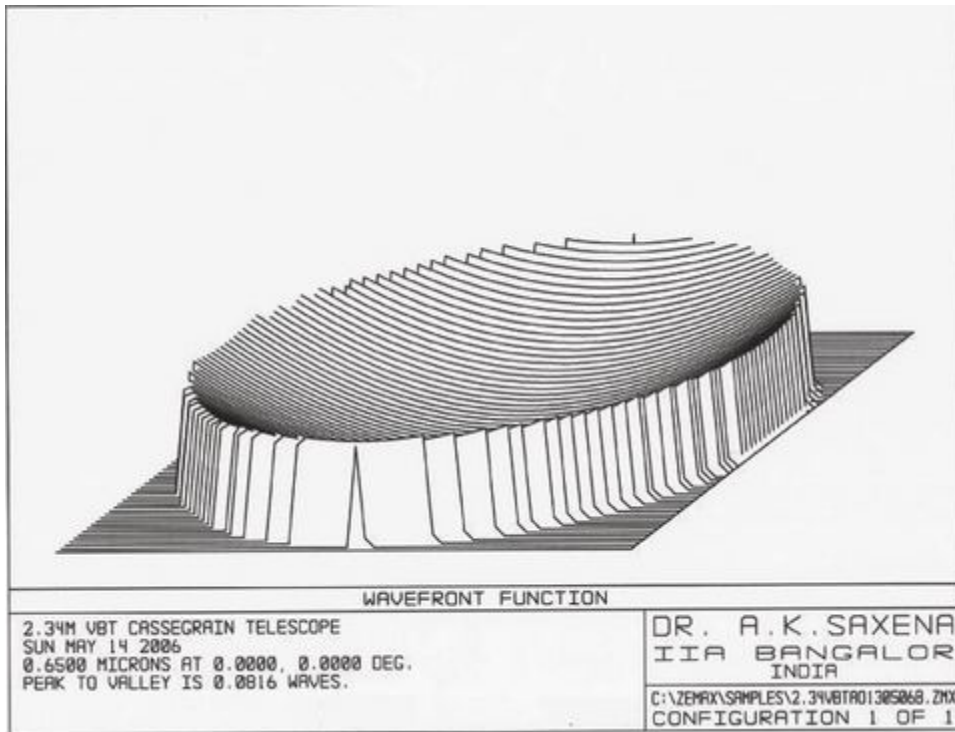


Fig. 5.9 Input on axis wave-front with peak to valley error of 0.0816 waves

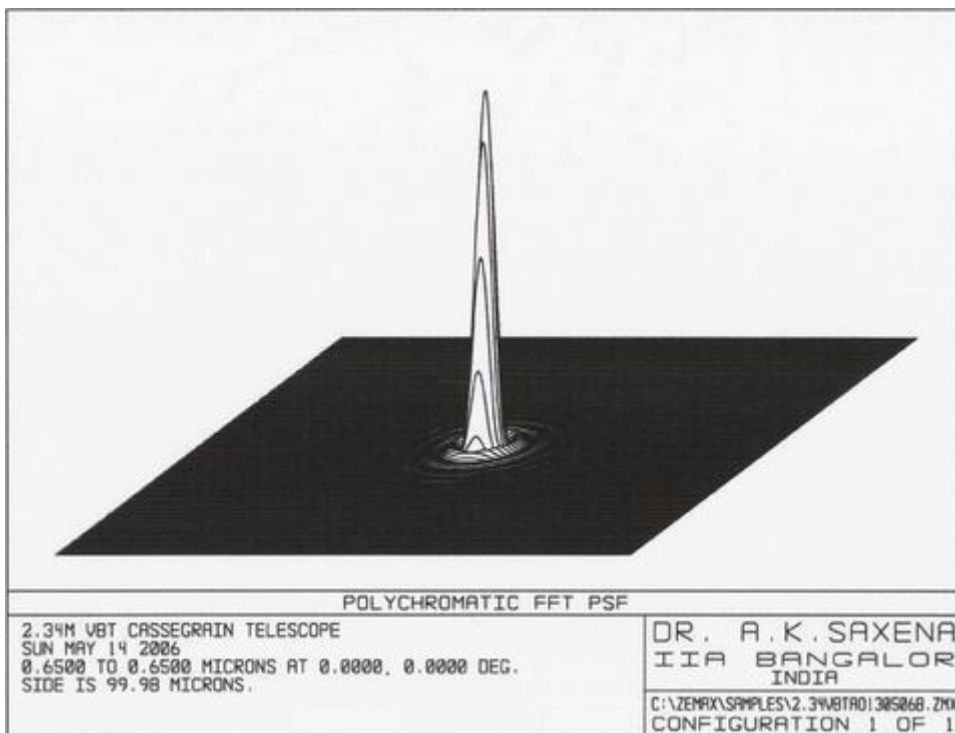
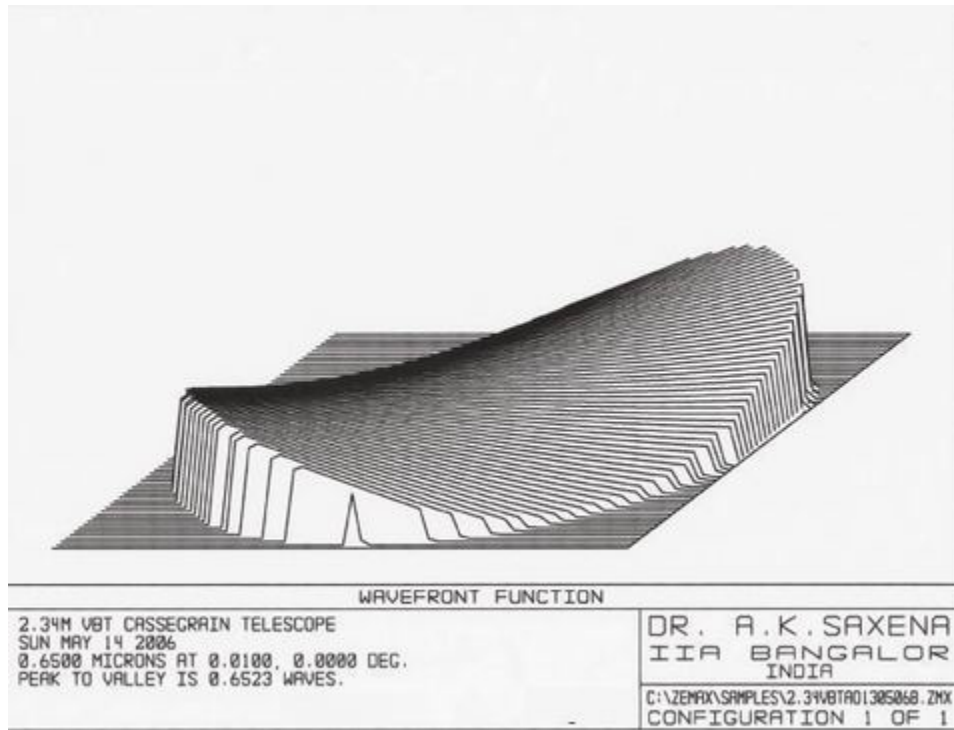
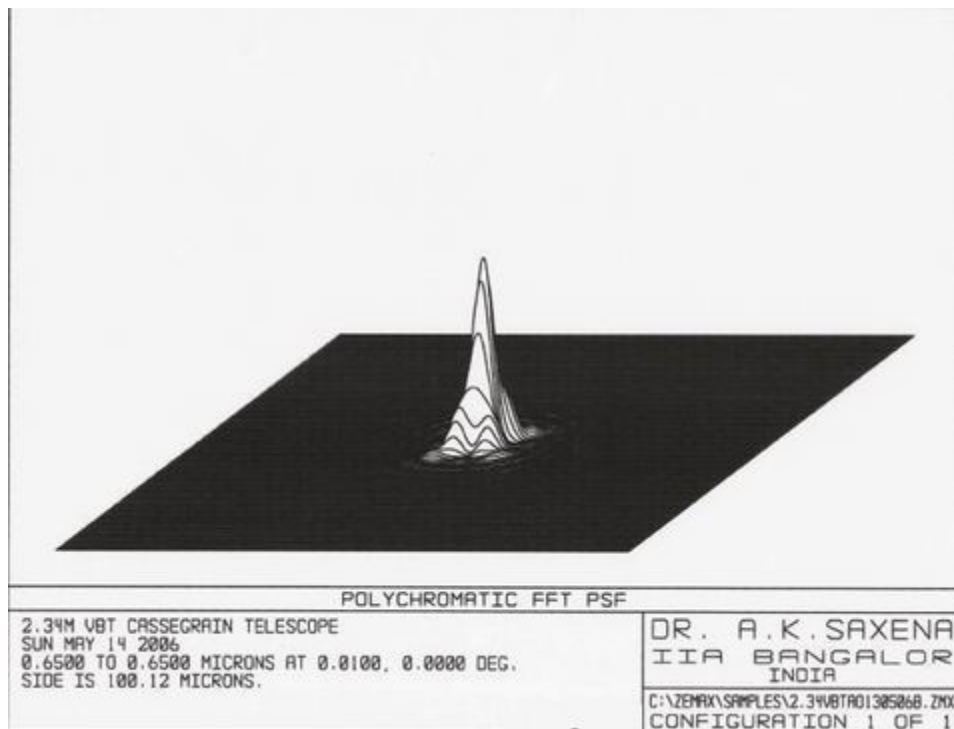


Fig. 5.10 PSF of wave-front for input wave-front error of 0.018 peak to valley error



*Fig. 5.11 Input wave-front with 0.01 deg. Error*



*Fig. 5.12 PSF for wave-front error of 0.01 deg.*

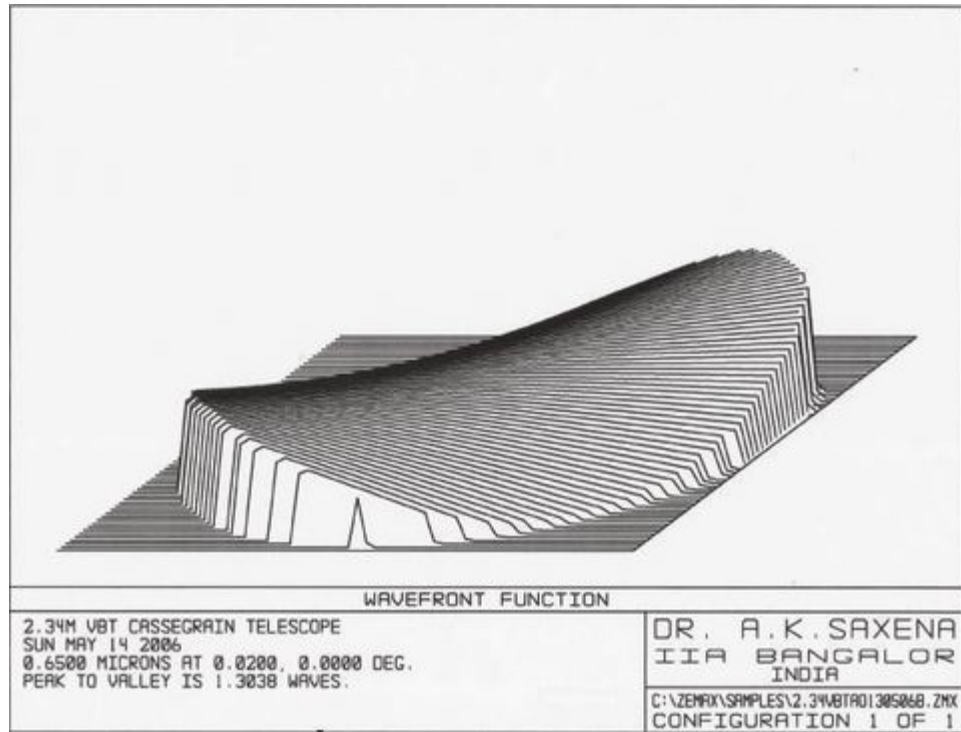


Fig 5.13 (Top) Input Wave-front with 0.01 deg. Error

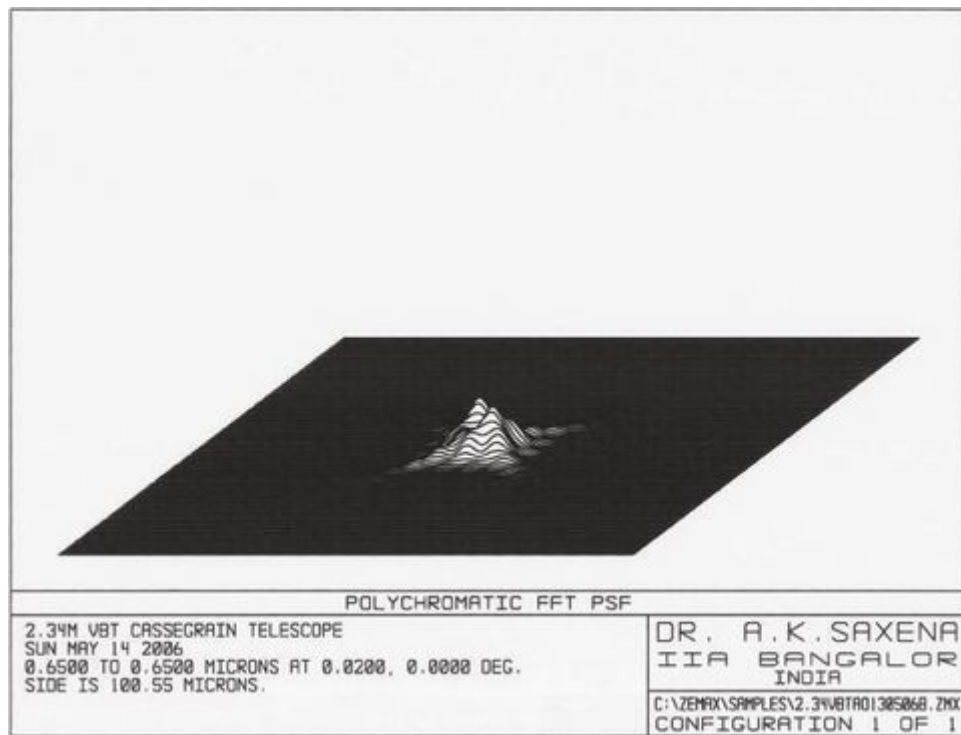


Fig 5.14 PSF for input Wave-front with 0.01 deg. Error

Listing of Zernike Standard Coefficient Data

File : C:\ZEMAX\Samples\2.34vbt\aoi30506b.ZMX  
 Title : 2.34M VBT Cassegrain telescope  
 Date : SUN MAY 14 2006

Note that RMS (to chief) is the RMS of the OPD after subtracting out piston.  
 The RMS (to centroid) is the RMS after subtracting out both piston and tilt.  
 The RMS (to centroid) is most physically significant and is generally what  
 is meant by 'the RMS'. Although ZEMAX uses the term 'centroid' for brevity,  
 the reference point is not the diffraction intensity centroid, but the reference  
 point which minimizes the variance of the wavefront.

Using Zernike Standard polynomials.

Field : 0.0000, 0.0000 deg  
 Wavelength : 0.6500 microns  
 Peak to Valley (to chief) : 0.081617 waves  
 Peak to Valley (to centroid) : 0.079099 waves

From integration of the rays:  
 RMS (to chief) : 0.022440 waves  
 RMS (to centroid) : 0.022405 waves  
 Variance : 0.000502 waves squared  
 Strehl Ratio (Est) : 0.980377

From integration of the fitted coefficients:  
 RMS (to chief) : 0.022567 waves  
 RMS (to centroid) : 0.022532 waves  
 Variance : 0.000508 waves squared  
 Strehl Ratio (Est) : 0.980158

RMS fit error : 0.000000 waves  
 Maximum fit error : 0.000000 waves

Z	1	0.039803	:	1
Z	2	-0.000000	:	$4^{1/2} \{p\} * \cos(A)$
Z	3	-0.001266	:	$4^{1/2} \{p\} * \sin(A)$
Z	4	0.022524	:	$3^{1/2} \{2p^2 - 1\}$
Z	5	0.000000	:	$6^{1/2} \{p^2\} * \sin(2A)$
Z	6	0.000079	:	$6^{1/2} \{p^2\} * \cos(2A)$
Z	7	-0.000445	:	$8^{1/2} \{3p^3 - 2p\} * \sin(A)$
Z	8	-0.000000	:	$8^{1/2} \{3p^3 - 2p\} * \cos(A)$
Z	9	0.000000	:	$8^{1/2} \{p^3\} * \sin(3A)$
Z	10	-0.000000	:	$8^{1/2} \{p^3\} * \cos(3A)$
Z	11	-0.000353	:	$5^{1/2} \{6p^4 - 6p^2 + 1\}$
Z	12	0.000000	:	$10^{1/2} \{4p^4 - 3p^2\} * \cos(2A)$
Z	13	0.000000	:	$10^{1/2} \{4p^4 - 3p^2\} * \sin(2A)$
Z	14	-0.000000	:	$10^{1/2} \{p^4\} * \cos(4A)$
Z	15	-0.000000	:	$10^{1/2} \{p^4\} * \sin(4A)$
Z	16	0.000000	:	$12^{1/2} \{10p^5 - 12p^3 + 3p\} * \cos(A)$
Z	17	0.000002	:	$12^{1/2} \{10p^5 - 12p^3 + 3p\} * \sin(A)$
Z	18	0.000000	:	$12^{1/2} \{5p^5 - 4p^3\} * \cos(3A)$
Z	19	0.000000	:	$12^{1/2} \{5p^5 - 4p^3\} * \sin(3A)$
Z	20	-0.000000	:	$12^{1/2} \{p^5\} * \cos(5A)$
Z	21	-0.000000	:	$12^{1/2} \{p^5\} * \sin(5A)$
Z	22	0.000000	:	$7^{1/2} \{20p^6 - 30p^4 + 12p^2 - 1\}$
Z	23	0.000000	:	$14^{1/2} \{15p^6 - 20p^4 + 6p^2\} * \sin(2A)$
Z	24	-0.000000	:	$14^{1/2} \{15p^6 - 20p^4 + 6p^2\} * \cos(2A)$
Z	25	-0.000000	:	$14^{1/2} \{6p^6 - 5p^4\} * \sin(4A)$
Z	26	0.000000	:	$14^{1/2} \{6p^6 - 5p^4\} * \cos(4A)$
Z	27	-0.000000	:	$14^{1/2} \{p^6\} * \sin(6A)$
Z	28	0.000000	:	$14^{1/2} \{p^6\} * \cos(6A)$
Z	29	-0.000000	:	$16^{1/2} \{35p^7 - 60p^5 + 30p^3 - 4p\} * \sin(A)$
Z	30	-0.000000	:	$16^{1/2} \{35p^7 - 60p^5 + 30p^3 - 4p\} * \cos(A)$
Z	31	-0.000000	:	$16^{1/2} \{21p^7 - 30p^5 + 10p^3\} * \sin(3A)$
Z	32	0.000000	:	$16^{1/2} \{21p^7 - 30p^5 + 10p^3\} * \cos(3A)$
Z	33	0.000000	:	$16^{1/2} \{7p^7 - 6p^5\} * \sin(5A)$
Z	34	-0.000000	:	$16^{1/2} \{7p^7 - 6p^5\} * \cos(5A)$
Z	35	-0.000000	:	$16^{1/2} \{p^7\} * \sin(7A)$
Z	36	0.000000	:	$16^{1/2} \{p^7\} * \cos(7A)$
Z	37	-0.000000	:	$9^{1/2} \{70p^8 - 140p^6 + 90p^4 - 20p^2 + 1\}$

### 5.3 Theoretical requirements of a wave-front error measurement and correction system for VBT

The 2.34M VBT configuration and the measured seeing parameter are already given at the end of chapter 2. For the above telescope and the atmospheric seeing parameters, technology for an online optical servo correction system developed is the main theme of this thesis work.

Number of lenslet array required	$= \left(\frac{D}{r_o}\right)^2$
	$= (2320 / 75)^2 = 957$
Lenslet geometry	$= 31 * 31 = 961$
Number of actuators required for deformable mirror	$= 957$
Bandwidth required of deformable mirror	$= 500 \text{ Hz}$
Cycle time required for control	$= 10 \text{ msec}$

The time required to acquire one frame of image is about 10 msec, These calculations give us a theoretical, ideal requirement of lenslet array and the deformable mirror system. But in actual practice, low cost mirrors with about 1000 actuators are not available. Based on the study and available technology, the following recommendations are made for the on-line wave-front measurement and correction system for VBT.

### 5.4 Recommendations of system parameters for Wave-front sensing system and on-line error correction system for VBT

The telescope with optical layout and the error measurement and correction system is shown in fig 5.1. As explained in section 4. it is not possible to work out a complete correction system because of non availability of low cost adaptive mirrors. Currently mirrors with 37 and 59 actuators alone are available commercially. The CCD or CMOS camera speeds are the other restrictions.

Even though CMOS imager is faster than CCD, for full correction, the speed of CMOS also is not enough; hence a partial correction system is being worked out. Here, the 37 actuator deformable mirror is taken as the control mirror and a system is worked around that.

No of actuators available in a low cost deformable mirror	= 59
No of lenslet array required	= 100 (10 x 10)
No. of pixels for subaperture	= 20
CMOS imager region of interest	= 100 x 100 pixels
No.of frames obtained for 128 by 128 pixel region	= 50 frames / sec
If 24 $\mu\text{m}$ pixel is chose, CMOS pixel area covered	= 3.2 mm x 3.2 mm
In-coming collomated beam diameter	= 20 mm

As the CMOS size is a limiting factor, suitable re-imaging unit can be used.

### **5.5 Identification of sub-systems for a real time correction system**

The essential subsystems for a real time correction system are;

- Precision optical components consisting of wave-front sampler, Beam generation optics and beam reducer.
- An imaging camera
- A tilt mirror system to correct the tilt errors
- A deformable mirror to correct high frequency errors
- A computer system to acquire images from the wave-front sensor camera and to compute the wave-front errors. Optionally, the 3-D wave-front can be displayed in the computer monitor. After finding the Zernike polynomials, the voltages required to correct the aberration are generated.

### 5.5.1 Lenslet array and precision optical components

Important components to implement a wave-front sensor are lenslet array, a fast camera system, a good quality reference beam and a fast computer to acquire and process the data coming from the camera system. A suitable beam reducer is introduced in the path of the beam to suit the combination of lenslet array and CMOS detector area. The lenslet array is placed in a conjugate pupil plane in order to sample the incoming wave-front. If the number of lenslet is small, correspondingly the geometric area covered by that lenslet will be large thus giving coarse sample. For experiments, Lenslet array with 20 x 20 lenslets was selected. In the earlier section, various types of CCD and CMOS cameras suitable for wave-front sensing are briefly discussed. Out of the various wave-front sensing methods explained in section 4.3, the wave-front sampler chosen for building and doing investigation is a Shack-Hartmann lenslet array based wave-front sensor. The details of the lenslet is given in the Appendix A.

#### Beam generation

- Commercially available beam expander with low wattage laser pointer powered by a regulated D.C. Supply can be used for reference beam generation.
- 6328 Å wavelength of operation.
- 20 cm beam expander from Casix, China
- Fibre optic light source from USA for telescope beam
- 50 µm pin hole for point source

#### Beam reducer

The CMOS sensor is 6.4 x 6.4 sq. mm. size, where as the lenslet size is 20 x 20 mm. sq. size. Beam reducer of suitable size is imperative. Other optical components required for wave-front sensing system are:

Good quality beam splitters are required to take a portion of the beam for wave-front error measurements and circular apertures for field reduction

- Cube beam splitters of 25 mm size
- Aperture of 20 mm diameter (usable area)

### **5.5.2 Selection of a Camera system**

Fuga-15d CMOS imager (63) manufactured by C-Cam technologies, Netherlands is a suitable choice for the system. It consists of a Peripheral Component Interconnect (PCI) bus based controller card and a single chip camera. The CMOS imager is mounted on a Printed Circuit Board (PCB) of size 25.4 mm square. It has a provision to mount a C mount lens. The main characteristics of the camera system are as follows:

- total die size: 7.4x8.2 mm<sup>2</sup>, 48 pin LCC package
- 512 x 512, 3-transistor active pixels, 12.5 μm pixels pitch, fill factor 15%
- 6.4x6.4 mm optical area
- on-chip 8 bit ADC
- on-chip multiplexing of address and data
- on-chip illumination control
- layer of dummy pixel around the active matrix
- pixels have a continuous operation in time (non-integrating)
- logarithmic intensity to voltage conversion
- extra row with reference current sources for calibration of the pixel photo currents
- addressing speed beyond 5 MHz
- Single power supply operation at +5 V.

Fuga 15 D is one of the first devices to be commercially available in the market, a few years ago. The CMOS imagers are being increasingly available now with special features and the same is chosen for experiments.

### **5.5.3 Selection of Deformable mirror**

Deformable mirror is used for correction of high frequency corrugation of in-coming wave-front. The clear aperture required for wave-front correction experiment is 20 mm. Hence an adaptive mirror with 30 mm aperture size is

more than adequate. 59 channels, 30 mm, low cost mirrors are available from OKO technologies, Netherlands. It also requires 59 channels Digital to Analog converters and 59 channel high voltage amplifiers. Even though the theoretical design requires more channels, only 59 channel mirrors are commercially available.

#### **5.5.4 Selection of tip-tilt mirror**

Tip-tilt mirror is required for correction of tilt in the in-coming wave-front. Tilts are measured about X and Y co-ordinates. Normally, piezoelectric actuator based systems have required acquired accuracy and stroke. The hysteresis effect seen in these devices can be eliminated in closed loop control. Three actuators are used to obtain two axis tilts.

#### **5.5.5 Computer system**

Currently 64 bit PCs with 3 GHz clock speed are available. The current PCI bus standard has high throughput, hence the same can be chosen for computer system and interfacing.

The optimal configuration for an on-line wave-front error measurement and correction system is worked in some detail in the above paragraphs. Present technology and availability of the deformable mirror limits the adaptive optics correction in a restricted way. Even the restricted correction is useful for the better performance of the telescope and improved image quality. Wave-front sensor is an important component of the closed loop correction system. Next chapter gives details about the design, construction and testing of the wave-front sensor system.

## Chapter 6

### Design, construction and testing of Wave-front sensor system

The design and construction of an online wave-front error measurement and correction system depends on the atmospheric parameters that degrade the image obtained through the telescope at the specific telescope location. It is shown in chapter 2 that the Fried's parameter  $r_0$  is an important atmospheric degradation parameter. The measured values of  $r_0$  for 2.34M VBT at 10 millisecond intervals was given in the same chapter. Based on these inputs, the system design was carried out. All optical components, control mirrors and electronic components were chosen based on the optical system design outlined in chapter 5. The sub-systems were integrated in the laboratory for design verification and validation. The testing of the system on the telescope will be done later as it involves special mechanical interface fabrication. The telescope is always in use for current astronomical research, hence the system integration and verification was done in the laboratory first to validate the approach.

#### 6.1 Schematic of Shack-Hartmann lenslet array based wave-front sensor

In this chapter, details about the implementation of a wave-front aberration measurement system are given. It is to be noted that the experiments are conducted with available components and costs into consideration. Some times, the available components like adaptive mirrors and tilt mirrors have less than the required aperture and actuators. The laboratory experiments are conducted to develop the required technology in hardware, software and optical systems. The following pages explain the design, construction and testing of a wave-front sensor system based on Shack-Hartmann lenslet arrays.

Two types of imaging camera were used for tests; first one is the CMOS Imager and the second is the Low light level CCD camera. Experiments were

conducted to measure the spectral response of the Fuga CMOS imaging device using table top spectrometer and the spectral response matched well with the one supplied by the manufacturer. It is experimentally found that about 480 frames per second can be captured using this device for a 32 x 32 region. The size of the CMOS imager is 6.4 x 6.4 mm but the lenslet array is 20 mm square. A collimated source of light passing through lenslet array gives 21 x 21 spot images. A re-imaging optical system was assembled to match the fields. The performance of Shack-Hartmann lenslet array based wave-front sensor using the CMOS imager as detector is satisfactory as shown below and meets the requirement of wave-front sensor for adaptive optics. The theoretical background and the algorithm developed for data reduction for wave-front sensing is already explained in section 4.4.

The schematic of the new wave-front sensor is shown in fig. 6.1. In this experiment, commonly available, good quality laser pointer is used as the source. The cell of the pointer was removed and a regulated varying D.C. power supply was connected. By this way, the intensity of the laser beam can be easily controlled by adjusting the voltage applied to the pointer. The other way to reduce the beam intensity so that CCD or CMOS camera is not saturated is to introduce neutral density filters. It is found that varying the voltage of the laser source is much easier. Laser source is attached to one end of the beam expander unit, which gives out a 25 mm collimated beam. A circular aperture restricts the beam to 10 mm diameter and the beam then passes through a beam splitter of 25 mm cube and gets reflected by the tip-tilt mirror. The details of the tip-tilt mirror are given in the next section.

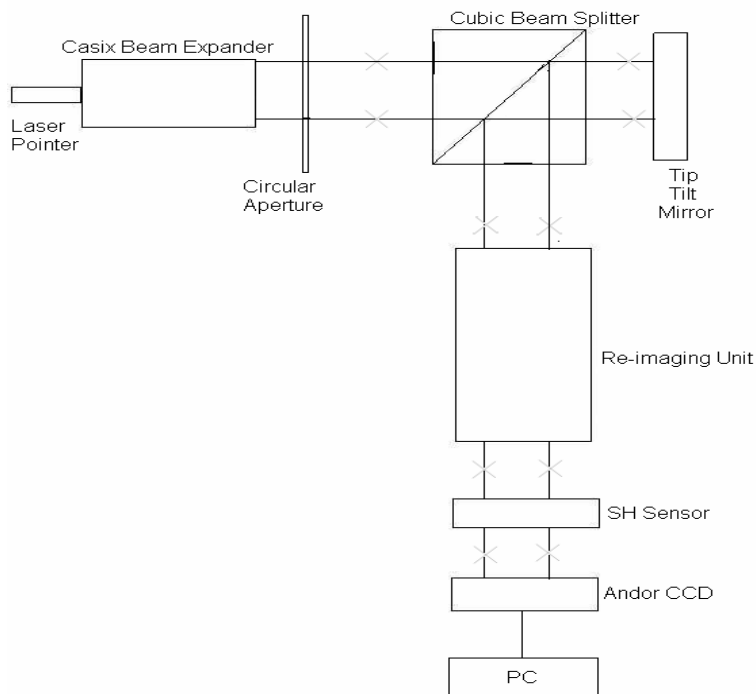


*Fig. 6.1 Schematic of Shack-Hartmann lenslet array based wave-front sensor*

The image size is reduced to match the CMOS sensor size of 6.4 by 6.4 mm by the beam reduction unit and passes through the Shack-Hartmann lenslet array. The wave-front camera is kept at the focal point of the lenslets. For calibration purposes, a known aberrated wave-front is to be given as a test input. When the tip-tilt mirror voltages are zero, the reflected wave-front from the tilt mirror does not have any tilt and this beam is taken as the reference beam for aberration measurement. Referring to fig. 6.2, the mirror is mounted in its support such that moving actuator A gives Y tilt.

Initially, 0 V is applied to all the three channels of the tip-tilt mirror. A reference beam is first obtained by powering the laser and capturing an image by the wave-front camera. Then voltage to actuator A alone is varied in steps and

the corresponding wave-fronts are captured. Using these two images, error in the wave-front is computed in terms of Zernike polynomials using the procedures and methods explained in chapter 4.

## 6.2 Tilt mirror system

The tilt mirror platform consists of a housing made with invar and three piezoelectric actuators. The three actuators beneath it push up and down the mirror platform. Referring to Fig. 6.2, A, B and C are the length of the three actuators.

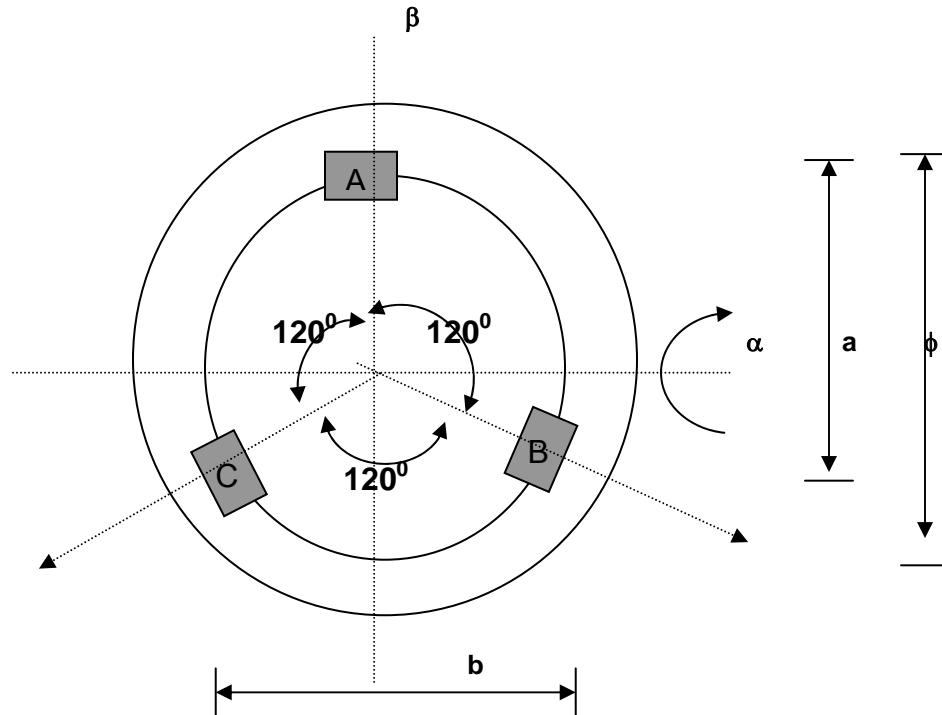
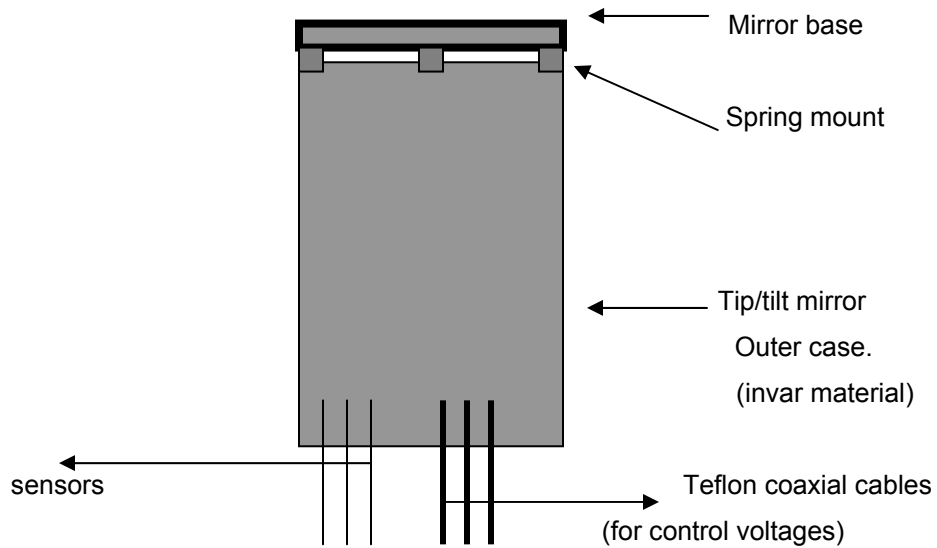


Fig. 6.2 Piezoelectric actuators A, B and C and the tilt angles  $\alpha$  and  $\beta$



*Fig. 6.3 Side view of the tilt mirror*

The lengths can be varied by applying a D.C. voltage of - 20 to +250 V and  $\alpha$ ,  $\beta$  are the two orthogonal angles about which the mirror base can tilt. Vertical spacing between actuator A and B is  $a$ , and horizontal spacing between B and C is  $b$ . Applying equal voltages to the actuators moves the mirror forward without any tilt and this is called piston movement. Varying the voltages applied to the actuator A alone keeping B and C at 0 V varies the length of the actuator A alone giving Y tilt. Same way, keeping actuator voltage A at zero and varying voltages of B and C equally tilts the mirror in  $-Y$  direction. In a similar way, applying different voltages to the actuators tilts the mirror mount in different directions

Dimensions of tilt mirror system used in experiments:

$$\varphi = 10\text{mm}$$

$$a = 7.5\text{mm}$$

$$b = 8.66\text{mm}$$

$$0 \leq A = B = C < 10\mu\text{m}$$

### **6.2.1 Power amplifiers for Piezoelectric actuators**

Three power amplifiers are required for three actuators. Input signal to the power amplifier is  $\pm 10$  V. The actuators are essentially capacitive loads, and hence they need high charging current. As the piezoelectric effect is a molecular phenomenon, the length can be varied in tens of nanometers. Piezoelectrics have appreciable hysteresis. To linearize them, strain gauge foils are mounted with the actuators to give a feedback on the actual movement of the piezoelectrics and the position control system compensate for the varying length.

### **6.3 Computer system**

The computer system chosen for experiment is a readily available PC in the laboratory. It can be upgraded to a much more powerful system later on.

- Pentium IV with 2.0 GHz or more clock speed
- 1 GB memory
- High speed graphics card

U.S. military has developed dedicated parallel processors for wave-front computers, (63) investing huge amount of money and man-power. For low cost systems, commercially available desk-top PC is the cheap solution. Initially, a PIII system was used and later it was replaced by a P IV system.

#### **6.3.1 PCI bus based signal generation card**

Initially ISA bus based cards provided by OKO technologies were used for experiments.

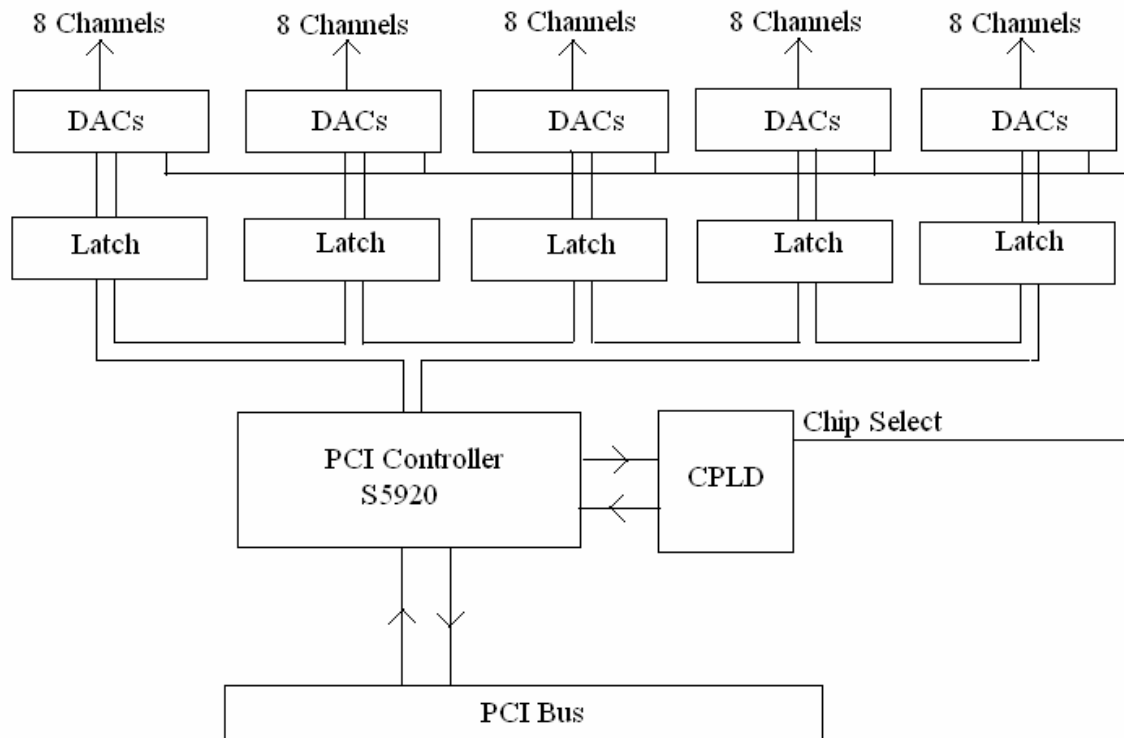


*Fig. 6.4 Block diagram of 32 bit PCI bus interface card with 40 channels of DACs*

As the this bus is no longer supported in the new machines, a compatible PCI bus based interface card was fabricated. Now, a single card contains all the 40 channels. Fig. 6.4 shows the block diagram of the DAC card. The driver software required for the control of this PCI card was developed and tested successfully. There are totally 40 channels to be controlled. The digital to analog converter (DAC) AD7228 contains 8 DACs of 8 bit resolution in a chip and 5 ICs give 40 channels of DAC. Three channel voltages are fed to the power amplifier of tip-tilt mirror and the remaining 37 channel voltages are fed to the power amplifier of the adaptive mirror.

The 37 actuator deformable mirror was procured from OKO<sup>R</sup> Technology, The Netherlands, who has the license to manufacture Delft University deformable mirrors. As the mirror was purchased a couple of years back, PC interface card

supplied with the mirror was based on 8 bit, ISA bus which was working with Pentium III or earlier computers. Now, P IV computers of 32 bit and 64 bits are available. The I/O bus of the PC is changed to PCI bus. This forced us to design and fabricate 32 bit, PCI interface card. The essential hardware is PCI bus controller based on S5920 chip from AMCC and a CPLD. CPLD generates chip select logic for 8 numbers of 8 bit ports. AD7228 chip contains 8 channels of 8 bit DAC in a chip. For a digital input word of FF(hex), the DAC generates 3.689 V. Details about the hardware is shown in fig. 6.4. In the computer field, frequent upgradation of processors, operating systems and I/O devices force us to spend considerable time on a continuous learning curve.

When it is found that the CMOS imager data is very noisy at room temperature, cooling arrangement with peltier coolers were tried out. The CMOS imager pixels have only 15 % fill factor, rest of the area of the pixel is occupied by electronic circuits. Later on, it is understood that the source of noise is not of thermal origin hence cannot be reduced by cooling.

#### **6.4 Testing of the new wave-front sensor using CMOS imager as the detector**

Initial tests of CMOS imager based Shack-Hartmann wave-front sensor system was performed in the laboratory, the schematic of which is shown in fig. 6.1. the only change is the ANDOR CCD is replaced by the CMOS imager. The reference beam is reflected by the tilt mirror and it passes through lenslet array and the CMOS imager. In this scheme, error sources like telescope optics and the image reduction optics are removed. The tilt mirror gives pure tilted wave-front with other optical errors of negligible amount. CMOS imager has 512 x 512 pixels and the full image gives 21 x 21 lenslet images. In the above picture, region of interest is chosen covering 128 x128 pixels which covers 5 x 5 lenslet arrays.

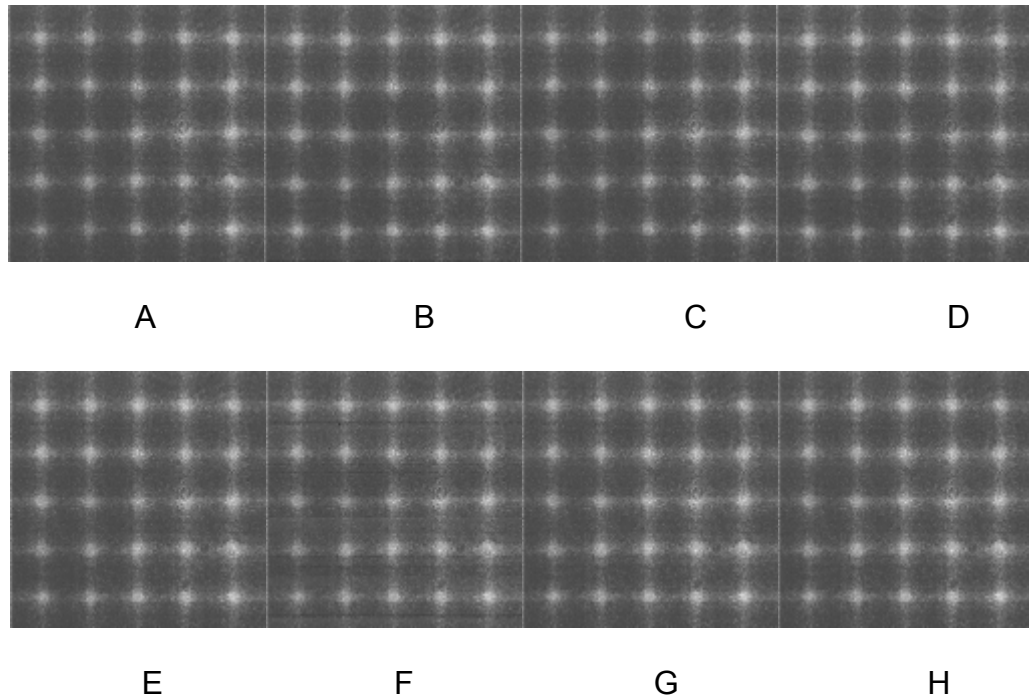


*Fig. 6.5 Images of 5 x 5 lenslet array for different actuator voltages of tip-tilt mirror. A B C etc. are the file names for varying tilt conditions.*

With a Pentium PC working at 550 MHz clock speed gave about 50 frames per second. It can be seen that each sub-aperture for a lenslet image is a matrix of 24 by 24 pixels. These images are without any intervening beam reduction unit. If a 50 % beam reduction optics is introduced in between, the 64 by 64 sub-area is enough for 5 by 5 lenslet images and the frame rates increases to 177 frames per second and the single frame time is less than 10 msec. Hence CMOS imager is able to satisfy the speed requirements with additional optics.

Results of analysis of the above images using the software developed are given in table 6.1. Usage of CMOS imager as a camera system for wave-front sensor reveals the following characteristics of the CMOS imager.

- The image is digitized to 8 bit accuracy by the on-chip analog to digital (A / D) converter. 128 by 128 pixels of CMOS imager gave 5 x 5 lenslet points. The user can choose the region of interest covering required number of lenslet

points depending on the speed within which one frame is to be read and the accuracy requirements.

- The maximum intensity at the lenslet center is about 150 to 185 counts where as the background counts near the lenslet is 70 to 80 counts, giving the signal to noise ratio of about 7. The contrast of the image was poor.
- The adjacent lenslets are jointed by very thin lines in horizontal and vertical direction. Careful inspection has revealed that it is the diffraction pattern which surrounds the lenslet image position.

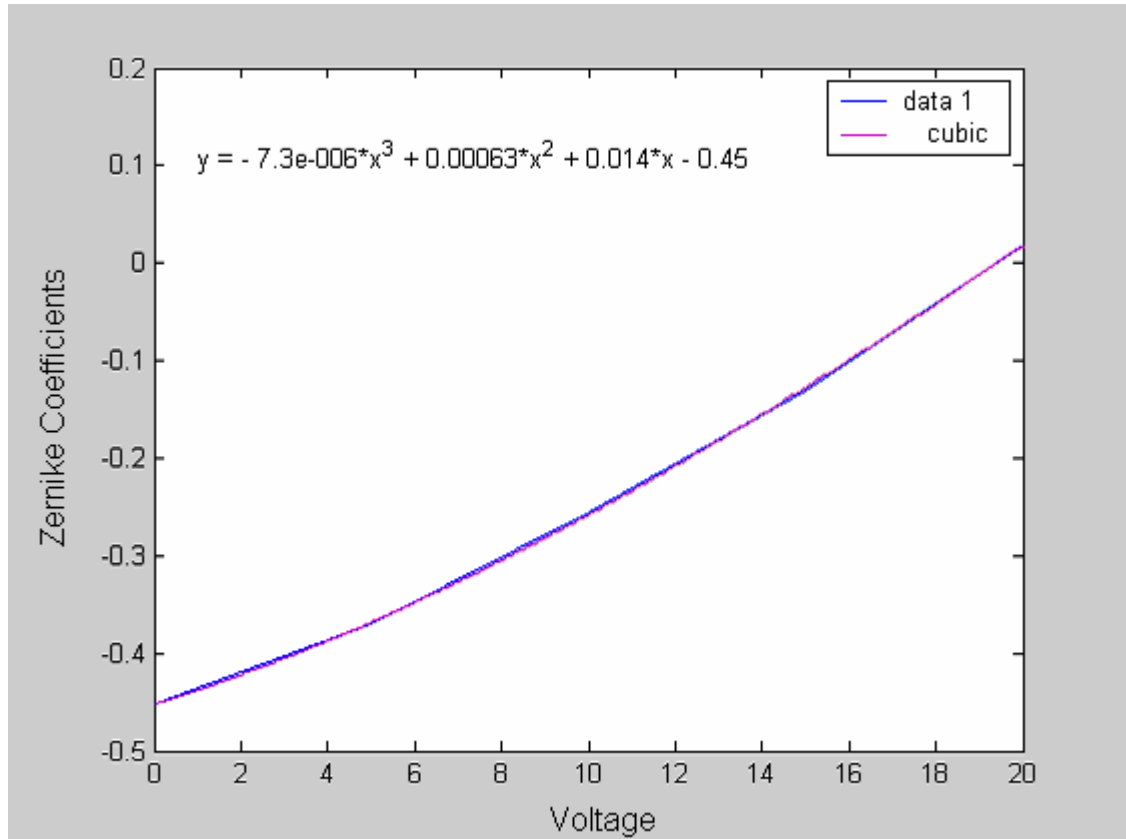
Each of the above images is taken by increasing the voltage applied to the three channels of tip-tilt mirror. Initially, centroid calculations did not show appreciable shift for varying voltages. But testing the tip-tilt mirror with the long trace profilometer explained in chapter 5 has shown movement of the actuator with varying voltages. It is found that straight forward application of centroid algorithm was not giving correct results because of the diffraction patterns and other noise present in the image. Hence alternate methods were tried out.

Image processing algorithm in MATLAB's toolbox can automatically identify circular, square or diamond shaped objects and centroids can be computed to those objects only. Control parameters like radius and width can be varied to suit the data. These parameters were varied for different light conditions. With the above modification, the computed centroids are found to be accurate.

Ref im.	Abb. Im.	3 Actuator volts	X and Y Tilts	Comment
Z	Z	a=0,b=0,c=0	X= 0 Y= 0	Reference image
Z	R	a=15,b=0,c=0	Y= 0.2746 X= 0.0085	Tilt in y
Z	S	a=20,b=0,c=0	Y= 0.432 X= 0.0105	Tilt in y increases
Z	E	a=20,b=5,c=0	X= -0.1307 Y= 0.4192	Tilt in x and y
Z	F	a=20,b=10,c=0	X= -0.1813 Y= 0.4127	“
Z	G	a=20,b=15,c=0	X= -0.396 Y=0.3224	“
Z	H	a=20,b=20,c=0	X= -0.5499 Y= 0.3610	“
Z	I	a=20,b=20,c=5	X= -0.4148 Y= 0.3104	“
Z	J	a=20,b=20,c=10	X= -0.3436 Y= 0.1750	
Z	K	a=20,b=20,c=15	X= -0.1818 Y= 0.0745	
Z	L	a=20,b=20,c=20	X=-0.0092 Y= 0.0183	Equivalent to reference image
Z	M	a=15,b=20,c=20	X= -0.0066 Y= -0.1297	Y tilt in negative dir
Z	N	a=10,b=20,c=20	X= -0.0398 Y= -0.2552	“
Z	O	a=5, b=20,c=20	X= -0.0444 Y= -0.3704	“
Z	P	a=0, b=20, c=20	X=-0.0764 Y= -0.4521	“

*Table 6.1 X and Y tilts computed from reference and aberrated images. Z is the reference image and R, S and E to P are the aberrated (pure tilts ) images.*

MATLAB did not support imaging cameras till recently (The new MATLAB release 14 has an image acquisition tool box but supports only a few popular camera systems). The algorithm explained section 4.3.1.1 and 4.4 were implemented in MATLAB and the results are shown in the table 6.1.



*Fig. 6.6 X axis shows Actuator A voltage varied from 20 V to 0 V and Y axis shows Zernike coefficient Y tilt alone changing for the configuration of the actuator shown in fig. 4.15. A cubic fit matches well to the hysteresis of the piezo actuator.*

It is seen that the background noise is higher. For reliable results, more than 12 bit data is required and the signal to noise ratio should be high. Normally CCD detector also has high thermal noise, but the detectors are cooled to - 40 to -100 deg. C. It seems that the noise origin in CMOS is not of thermal origin but of electronic noise which cannot be reduced by cooling the detector (65). When 0 V is applied to the three actuators A, B and C, the reflected wave-front from the tilt mirror is taken as reference. The actuator positions are so arranged that increasing the voltage to actuator A alone keeping B and C actuator voltages constant, as shown in Z, R and Z, S images increases the tilt in Y direction alone. Applying equal voltages to A, B, C as shown in Z, L images, gives the piston movement, ie., the mirror is moved forward, but the Hartmann-Shack sensor is

unable to detect the piston movement. In the same way, decreasing the voltage to A as shown in M, N, O, P images give y tilt in negative direction. This relationship is shown in the fig 6.3. Keeping A and B voltages same and increasing C voltage as shown in Z, I to I changes the tilt in both X and Y direction.

The software developed computes the Zernike polynomial up to 14 terms, but only the first two terms, ie., X and Y tilts alone are shown in the above table. A portion of data set is plotted in fig. 6.6. It is seen that the Piezo electric actuator has hysteresis and the cubic equation shown in fig. 6.6 can fit well to the data set. Other test methods like Long Trace Profilometer tests of the tip-tilt mirror shown in fig. 7.4 also shows hysteresis and matches well with the curve shown in fig. 6.6, thus proving that the algorithms developed and used for the wave-front sensor is correct and it gives reliable results even for noisy data as explained earlier (66). The CMOS imager that have been procured was a first generation device after it was commercially available. As there is considerable research activity being pursued by manufacturers to improve upon the device, the present day devices may have higher fill factor and low noise at a fractional cost of CCD systems, thus paving way for a very low cost wave-front sensing system.

#### **6.4.1 Summary of the new wave-front sensor using CMOS imager as a detector.**

The CMOS device has active pixel sensor with logarithmic response, which can tolerate high contrast scene. The single chip cameras have high-speed operation and the cost is less than that of a CCD camera. The random access architecture of CMOS pixels and the in-built analog to digital (A / D) converter increases the number of frames that can be acquired from the CMOS imager fulfilling the speed requirements. Unlike CCD, region of interest reading appreciably increase the speed as only those pixel data are digitised and read.

CMOS imager works with only 5V supply where as CCD needs multiple supplies. Interface to PC is simple because CMOS imager gives digital data

output. Camera system is compact with a small size PCB and consumes very little power. The cost of the system is also low. The Fuga 15 D CMOS imager what is used in the experiments is essentially a camera on a single chip with built in multiple Analog to digital converters on the imager itself.

Using the CMOS imager and shack-Hartmann lenslet array, a cost effective wave-front sensor was developed and its results are compared with other test methods and found to match well thus proving the correctness of design and development. Experimental results of the CMOS imager and LLLCCD camera as detector for wave-front sensors shown in Table 6.1 and 6.2, clearly prove the correctness of the new wave-front sensor developed. The data also shows that the tilt mirror platform is capable of responding to small voltage increments and the same can be effectively used for wave-front tilt corrections. The only drawback noticed is the presence of hysteresis to an extent. A cubic fit matches well with the data set and the resultant voltage equation is used for control of the tip-tilt mirror to compensate for the hysteresis effect.

The CMOS imager has the following drawbacks:

- The present Fuga 15 D camera has only 8 bit wide data.
- Signal to noise ratio is poor and noise cannot be reduced by cooling the detector
- Pixel has only 15% light sensitivity, Faint sources like stars may not give appreciable signal. Inter-pixel gaps give diffraction patterns.
- Accurate centroid calculations need further processing, increasing the computation time which in turn will increase the loop time for control of the adaptive mirrors.

### **6.5 Testing of the new wave-front sensor using Low Light Level CCD as the detector**

Low Light Level CCD (LLLCCD) is one of the most sensitive CCD available (67) in the market today. Details about this camera are already given in section 4.5.2.

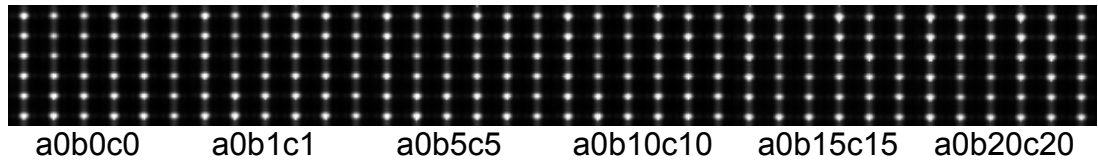


*Fig. 6.7 Images of 6 x 6 lenslet array captured by Andor L3 CCD camera. Image a0b0c0 is when the three actuators of tip-tilt mirror A,B and C are applied 0 volt. Image a0b1c1 is the lenlet image when actuator A is applied 0 V, actuator B is applied 1 V and actuator C is applied 1V.*

The experimental setup is same as used for testing CMOS imager based wave-front sensor. Laser beam generated by the laser pointer is expanded into a 25 mm size beam by the beam expander. This parallel beam is reflected by the tip-tilt mirror platform. The reflected beam passes through the lenslet array and then reaches the LLLCD. The three actuators (A, B, C) of the piezoelectric actuator based tip-tilt mirror platform is supplied with varying voltage by the computer and high voltage amplifier and the corresponding wave-front is captured by the CCD. Integration time used to capture one image is 10 msec. To start with, 0 V is applied to all the three actuators and the lenslet image is captured. This is shown as a0b0c0 image in fig 6.7. As the incoming wave-front is a parallel beam of good quality, a0b0c0 image is taken as the reference frame.

Zernike Coefficient	A0b5c5	a0b10c10	a0b15c15	a0b20c20
1 Tilt about X axis	-0.01948	-0.061855	-0.08133	-0.08879
2 Tilt about Y axis	-0.09832	-0.16985	-0.24516	-0.35071
3 Astigmat. +/-45deg	-0.00905	-0.02567	0.0085664	0.026946
4 Defocus	-0.01587	-0.035064	-0.024667	-0.04001
5 Astigmat. 0,90 deg	0.011256	-0.016897	-0.028187	0.015153
6 Trefoil x axis	-0.00383	-0.01878	-0.026595	-0.00912
7 3 <sup>rd</sup> order Coma x	0.002477	-0.002104	0.00436	0.007624
8 3 <sup>rd</sup> order Coma y	-0.0069	-0.013929	-0.012244	-0.01787
9 Trefoil y axis	-0.00814	-0.01380	-0.0007	-0.0101

*Table 6.2 First 9 coefficients of computed Zernike polynomial with LLLCD. Only Y variation is seen when actuators B and C are given equal voltage and actuator A voltage is 0*

By keeping the voltage to the actuator A at 0 V and applying equal voltages to actuators B and C, a pure tilt in the y direction can be generated.

The image a0b1c1 is the tilted wave-front when 0 V is applied to actuator A and 1 V is applied to B and C actuators. Increasing the voltages to actuators B and C increase the wave-front tilt in Y direction. These images are given as input to the Hartmann-Shack wave front sensor program for further computation. Zernike polynomials up to 14 terms are computed and only first 9 terms are shown in table 6.2. The data set is plotted as a graph in fig. 6.8 and the corresponding cubic fit to the data is also shown. The non linearity noticed is due to hysteresis

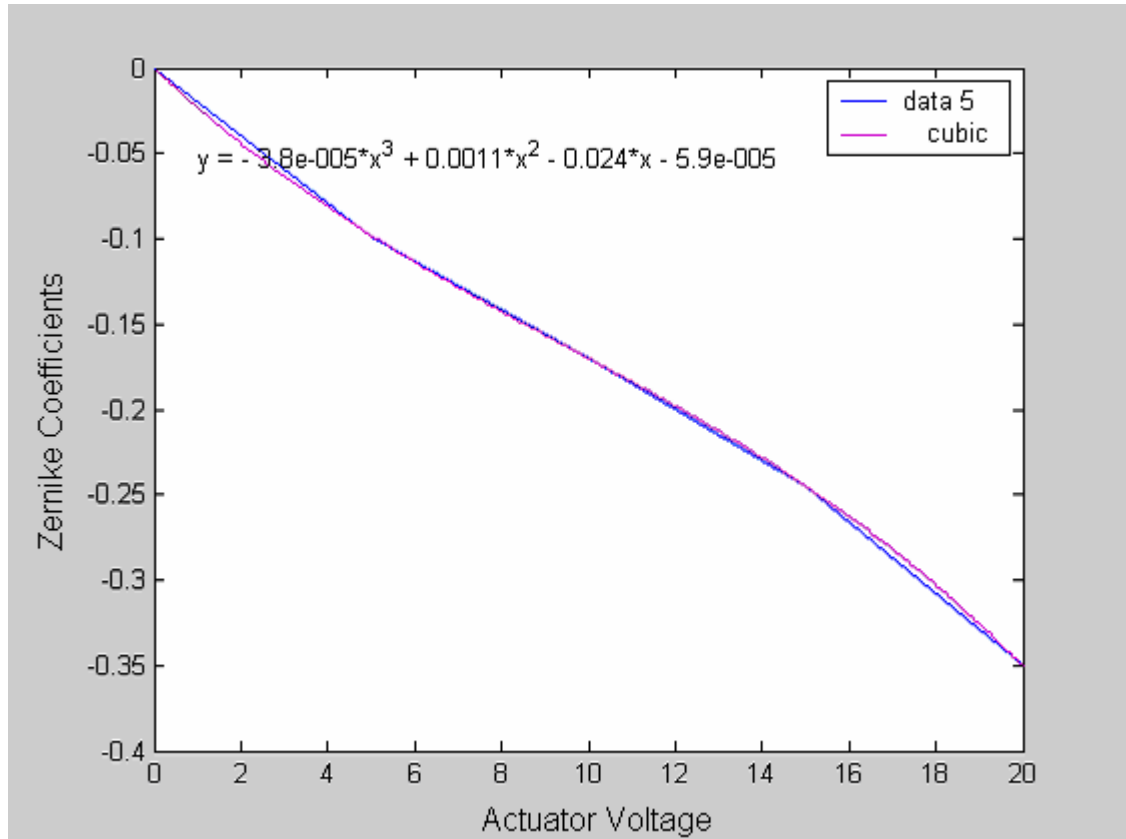


*Fig. 6.8 X axis is Actuators B and C voltages varied from 0 V 20 V when A voltage is kept constant*

### 6.5.1 Summary of the new wave-front sensor using LLLCCD as a detector

The advantages and drawbacks of the camera system is given below:

The chip has on-chip amplification of photo-electrons giving appreciable signal for faint sources like an intensified CCD camera. Peltier cooler used in the system is much compact and rugged than comparable liquid nitrogen cooled CCD cryostats. The CCD sensor is highly linear. With 16 bit digitization, bright and faint sources can be acquired without saturation. The lenslet image looks much sharper and occupies less number of pixels. Sharper the lenslet images, the better will be the quality of data.

The main drawbacks are as follows:

The pixel of the CCD is in rectangular size of 20 by 30  $\mu\text{m}$ . Software correction is to be applied to make the pixel square. The software supplied with the CCD camera system allows single frame acquisition with a minimum of 10 msec integration time. But the next frame can be taken only after 1.2 seconds. There is no provision in the software to reduce the time between frames.

If one wants to change the inter frame time, then one has to write the acquisition software himself. The company provides Software development kits (SDK) for this purpose. Windows programming knowledge is a must. The software given by the company acquires one frame of image, displays in the monitor and stores in the disk in one of the custom image formats. The user has to read from the disk for further processing. This process increases the cycle time for correction. The camera software should store the image in computer memory itself so that it can be read at much faster rate for further computation. The required software modification were tried out

## **6.6 Algorithms and software development**

For CMOS imager, the software supplied with the imager first finds out the available port addresses for PCI bus. The imager has 512 by 512 pixels. It is possible to take sub-region called region of interest, thus increasing the speed. First, a calibration file is acquired and then image frame is acquired. The calibration file is subtracted from the image file. The acquired image is displayed in the monitor and it is continuously updated. If one wants to save the image for further processing, the display can be halted and a file name can be given for storage. The software provided does not give real time capability.

Using the function calls provided by the manufacturer, driver software was developed for the imager to acquire one frame and the data was kept in the computer memory for further processing. Wave-front error computation and control were added to this program such a way that wave-front sensing and

control did not expect any further input from the user. The data reduction method used for wave-front sensing is detailed in the following section

### 6.6.1 Zernike polynomial representation in Cartesian Coordinates

It is assumed that circular apertures are normally used in practice. When an aperture circle of unit radius is expressed, Zernike coefficients for polar coordinates are usually used as listed in table 3.1. But the Shack Hartmann lenslet arrays are distributed in X and Y coordinates with equal distance between them. Sciichi Okuda et. al (68) have used Zernike polynomials in Cartesian coordinates for analysis of lateral shearing interferogram where the wave-front is circular. If the wave-front  $W(x,y)$  can be described by the polynomials, it is expressed as

$$W(x,y) = \sum_{i=1}^L A_i U_i(x,y) \quad (6.6)$$

l	n	M	U <sub>i</sub> (x,y)
1	1	0	1
2		-1	X
3		1	Y
4	2	-2	2xy
5		0	-1+2y <sup>2</sup> +2x <sup>2</sup>
6		2	y <sup>2</sup> -x <sup>2</sup>
7	3	-3	3xy <sup>2</sup> -x <sup>3</sup>
8		-1	-2x+3xy <sup>2</sup> +3x <sup>3</sup>
9		1	-2y+3y <sup>3</sup> +3x <sup>2</sup> y
10		3	Y <sup>3</sup> -3x <sup>2</sup> y

*Table 6.3 Zernike Polynomials in Cartesian Coordinates up to third order*

The term number L of the Zernike polynomials is  $L = (n+1)(n+2)/2$ , where n is the

maximum order of the polynomials and  $U_i(x,y)$  is the  $i$ th term of Zernike polynomials expressed in Cartesian coordinates and  $A_i$  is the coefficient of the term. Polynomials up to 4<sup>th</sup> order using 14 terms were used for error computation and the experiments conducted proved that the algorithm and software that has been developed and used is correct. Masking with a unit circle gives a circular pupil which is used for Zernike polynomial computation.

### **6.6.2 Computation of Zernike polynomials using lenslet array images**

Theory and algorithms for wave-front error computation from Shack Hartmann wave-front sensor is given in section 4.3.1 and 4.4. The number of lenslet array points are usually higher than the number of Zernike coefficients required giving an over determined system. Algorithms to solve an over determined system is developed and code was written in C and MATLAB to implement this algorithm.

### **6.7 Limitations and accuracy of wave-front error determination**

Shack-Hartmann lenslet images show diffraction patterns between the lenslet images, increases the errors in the computation of centroids. To overcome these problems, as explained before, circular object identifications were used. Fig. 6.5 shows the lenslet image from CMOS imager and Fig. 6.7 shows the image from cooled LLLCCD camera. Images from CCD camera are sharper and signal to noise ratio is much higher, but as explained previously, CMOS architecture of random addressing of the pixel and in-built A / D converter gives high speed operation suitable for real-time control experiments. Fuga 15 CMOS imager pixels, at present have only 15% fill factor, but CCD pixels have 100% fill factor and CMOS fill factor may improve in the coming years giving a very low cost, very fast imager compared to the CCD system.

It is shown in this chapter that a new wave-front sensor based on Shack-Hartmann lenslet array and CMOS imager as detector is successfully designed,

assembled, tested and calibrated with known input wave-fronts and it can be used for wave-front error measurements. Using the wave-front sensor output data as input, on-line correction of the wave-front is achieved. The following chapters give details about characterization of control mirrors and other details about the closed loop wave-front correction scheme.

## Chapter 7

### Characterization of tip-tilt mirror and MEMS based adaptive mirror

In real time wave-front compensation techniques, a conjugate surface of the incoming aberrated wave-front is to be created in real-time. Two types of mirrors are used for this purpose. The first one is a tip-tilt mirror and the second one is an adaptive mirror. Experiments were conducted using piezoelectric actuator based tip-tilt mirror and micro-electro-mechanical-systems (MEMS) based membrane mirror to understand their behaviour. This chapter explains the experimental results of characterizing tip-tilt mirror and theoretical and experimental characterization of the membrane mirror. The two control mirror systems that can be used for wave-front correction in adaptive optics are characterized by in-house developed test methods. The first one is a piezoelectric actuator based tilting mirror system and the second is MEMS based membrane mirror. The piezoelectric based mirror system was tested in the laboratory using interferometer and. Its performance and resolution matches the requirement of tilt corrections in adaptive optics. For the membrane mirror, only flat surface generation could be checked by interferometer. To find out the mechanical properties, FEM analysis was done. Tip-tilt mirror and deformable mirror were characterized using in-house developed Long Trace profilometer (LTP).

#### 7.1 Piezoelectric actuator based tip-tilt mirror system

Tests were conducted to measure the performance of a tilting mirror mount with its associated control module in the laboratory using the in-house built Long Trace Profilometer (LTP). A brief detail about LTP is given later in the chapter. Voltages required for the three actuators are produced by 8 bit digital to

analog converters and the linear and tilt movements of the actuators are measured. The main parameter of the tilting mirror system is as follows:

No. of actuators	: 3 mounted at 120 deg apart.
Operating voltage	: -20 to +120 V
Maximum tilting range	: 1 mrad
Linear position range	: 10 $\mu\text{m}$
Band width	: 2000 KHz (small signal)

With the preset gain in electronics control unit, a 7-volt change gave a linear movement of 7 microns. It is found that the actuator responds for even millivolts. The tilts were also measured using a standard interferometer and the new wave-front sensor and the data matches with this measurement. As the system responds to millivolt signals and it has sufficient resolution, it is suitable for wave-front tilt correction. The drawback is the hysteresis seen in the actuator as shown fig.7.1

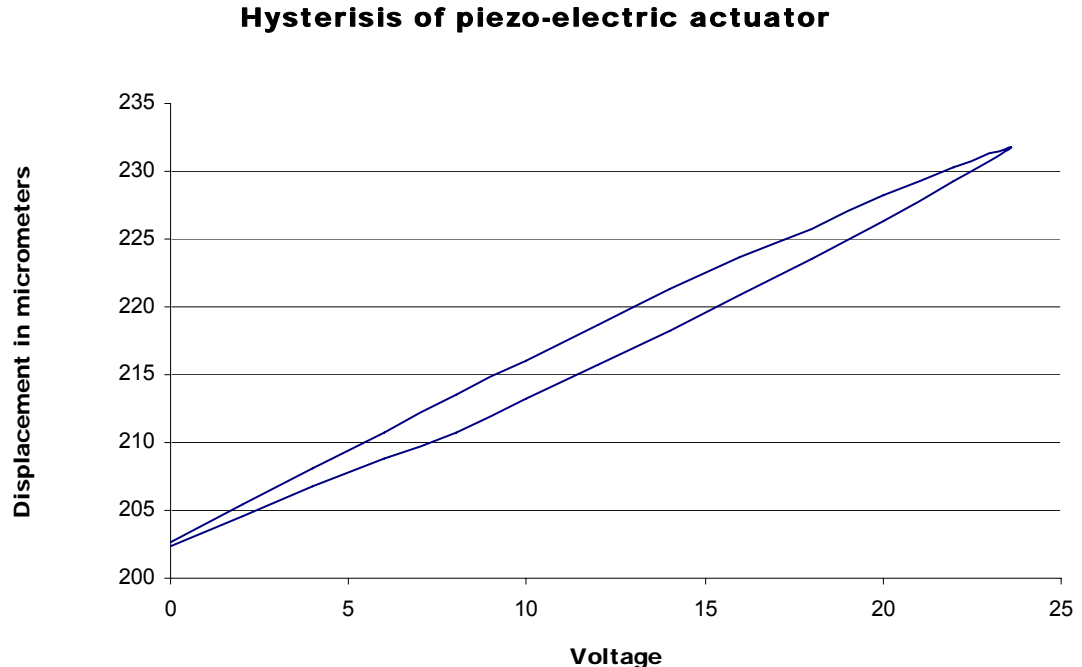


*Fig. 7.1 Hysteresis of one of the piezoelectric actuators measured with LTP*

. The effect of hysteresis is compensated by calibration of the wave-front errors with applied voltages with the new wave-front sensor.

## 7.2 Deformable mirror system types

Deformable mirrors (DM) are important components in a wave-front compensation system. Currently available deformable mirror types are:

- (i) Piezoelectric actuator based deformable mirror using variation in length
- (ii) Bimorph mirrors which bends for applied voltage
- (iii) MEMS based DMs where membrane is supported by mechanical attachment to actuators.

MEMS are of two types

- Bulk micromachined, freely suspended, continuous surface DMs
- MEMS based segmented DMs

Initially, adaptive mirrors were made with piezoelectric actuators. Thin rods of piezoelectric material with diameters of a few mm were used. On top of each actuator, reflective mirrors were placed. When voltage is applied to the rod, there is an increase in length of the actuator. Mirrors with 400 or more actuators were made and used for wave-front correction. Each segment of the mirror moves independently of each other, and hence, complicated wave-front corrections can be made. The disadvantage of this mirror system is the cost. As the mirrors are segmented, there will be diffraction effect and a small percentage of light loss. Zonal corrections can be applied easily; hence it is well suited for high order error corrections.

The bimorph mirrors are made with piezoelectric disks, where the diameter is much larger than the thickness. The piezoelectric disk acts as an active layer. A passive layer is glued to this and polished and coated with a reflective material. The bottom side of the piezoelectric disk is attached with many electrodes. When voltage is applied between electrodes and the top conducting layer, the piezoelectric layer expands in the plane of the device, causing a bending movement on the passive layer. By applying a voltage to

specific region, local bending can be achieved. The bimorph mirror has many attractive features. It has a continuous face-sheet; hence, there are no light loss or diffraction effects and the cost is lower than the stacked actuator explained before. Mark Ellis (69) has developed control equations for different configuration of bimorph mirrors. It is a modal device and therefore suited to low-order applications.

The recent developments in low cost DMs came from developments in microelectronics. Micro electro mechanical system (MEMS) based deformable mirrors as they are known is fabricated with the well developed integrated circuit fabrication technology. Bifano et. al., (70) of Boston University (BU), under a contract from National Aeronautics and Space Administration (NASA) have developed DMs using MEMS technology. Typical specifications of the Micro Machined Deformable Mirror (MMDM) of BU are as follows:

Membrane size	: 2 mm x 2 mm x 2 $\mu$ m
Active mirror area	: 1 cm <sup>2</sup>
Number of actuators	: 100
Actuator size	: 300 $\mu$ m x 300 $\mu$ m
Actuation	: Integrated electrostatic
Package size	: 10 cm <sup>3</sup>
Power consumption	: 0.2 W / channel
Actuator spacing	: 0.3 mm
Actuator stroke	: 2 $\mu$ m
Actuator repeatability	: 10 nm
Hysteresis	: 0%
Surface roughness	: 50 nm (root mean square)
Bandwidth in air	: 7 kHz
Maximum deflection	: 1.9 $\mu$ m at 241 V

The BU group has developed two types of continuous phase mirrors. The first is a continuous membrane mirror with a fill factor of 99.7%. The continuous mirror device

employs a single mirror membrane supported by multiple post attachments to an actuator array. This configuration has a mirror influence function of 30% which is higher than what is required for astronomical applications. The second is a continuous membrane mirror with inter-post cuts introduced into the mirror surface in order to relieve stress in the mirror membrane. It has a fill factor of 98.6%. As the mirror is not continuous, it will introduce unwanted diffraction patterns, but the mirror influence function may be suitable to some special applications. This stress-relieved design divides the mirror membrane into segments that are supported at their corners by post attachments to the underlying actuators. Post attachments are shared among adjacent mirror segments to ensure optical phase continuity from segment to segment.

The Air force institute of Technology of US has also developed DMs based on MEMS technology. The individual mirror segments are separated from each other; hence the mirror influence function is negligible. As in the case of piezoelectric actuator based stacked mirror, it is capable of doing zonal control and higher order corrections (71).

Gleb Vdovin, (72), Laboratory of Electronic Instrumentation, Delft University of Netherlands has developed DMs based on MEMS technology using bulk micromachining. The flexible mirror itself is formed by a low-stress nitride membrane, suspended on the edges of a window, etched into a silicon die. The top of the membrane is coated with a reflective material like aluminum or gold, to make it reflective and conductive. The actuators are hexagonal patterns of about 1.75 mm size, etched on a printed circuit board (PCB). There are 37 actuator patterns in the PCB arranged within a circle of about 12 mm. The membrane mirror is mounted over the PCB with a spacer. Voltage is applied between the conductive top of the membrane and the actuator pattern. The electrostatic force formed between the mirror top and the actuator pulls the mirror towards the PCB in the air gap between them.

This deformable mirror is commercially available from OKO technologies of Netherlands. DM with 37 actuators was procured from the above source. Presently, mirrors with more than 50 actuators are also available. Typical specification of the mirror is given below.

Typical specification of 37 channel Delft University DM:

Membrane mirror	: 0.5 $\mu\text{m}$ thick silicon-nitride membrane coated with 0.2 $\mu\text{m}$ Aluminum
Dia. of mirror	: 15 mm
Usable dia.	: 10 mm
Actuator	: Hexagon shaped PCB pad
Spacing of actuator	: 1.75 mm center to center
Distribution	: Actuators are in 3 concentric rings around a central Actuator with 6, 12 and 18 actuators in the rings
Max. deflection	: 5 $\mu\text{m}$

The differences between the three varieties of the DM mirrors are as follows. The BU DM and the AFIT DM are segmented, hence, capable of zonal correction, correcting higher order Zernike terms. DU DM is a continuous membrane, hence capable of correcting lower Zernike terms.

For this study, Delft University of The Netherland developed MEMS based DM was chosen for the reasons of easy availability and large size of the usable area of the mirror.

### **7.3 Deformable membrane mirror characterization**

The flexible membrane mirror is formed by low-stress nitride membrane suspended on the edge of a window, etched into a silicon die. Aluminum or gold coating is given on top of this to give reflectivity. This die is mounted on a printed circuit board with spacer in between in which hexogen shaped patterns are etched.

Fig. 7.5 gives the configuration of the 37 actuators used for the deformable mirror. The same set up mentioned earlier was used to test this mirror test also. The deformable mirror poses special problem for control. If one actuator is energized, not only the surface in front of this actuator is being pulled, but nearby surface is also influenced by it. This influence function is to be determined for

effective control of such mirrors. As the mirror is very thin, only a few  $\mu\text{m}$  thick, it becomes necessary to find out its mechanical properties like the force that will rupture it, its resonant frequency, the mirror influence function, applied voltage against mirror deflection, its initial aberration etc. As a single test cannot measure all the properties, different tests were conducted. They are listed below;

- A Finite Element Analysis of the mirror to find out its mechanical properties like strength, natural frequency of oscillation and mirror influence function
- A non contact type test with an in-house built LTP to measure the shapes of the mirror for different voltages applied to actuators. Measurement of linearity, hysteresis and three dimensional pictures of mirror surfaces generated for various voltage combinations.
- An interferometer test to measure its initial aberrations and voltages required to make the mirror flat
- LLLCD based wave-front sensor to characterize the mirrors in terms of Zernike polynomials for known wave-front errors. The following pages give details about these tests and characterization of the deformable mirror which is used for real-time control of the wave-front correction system

### **7.3.1 Finite element analysis of the membrane mirror.**

If the aberrations in the incoming wave-front are known, then it can be corrected by the tip-tilt and deformable mirror. The tip-tilt mirror has 3 piezoelectric actuators kept in a circle separated by  $120^\circ$ . The details about the control of the tip-tilt mirror is given in earlier section. The 37-actuator deformable mirror control is a complex problem. First, there are 37 channels of closed loop controls and all the channels should be controlled simultaneously. Using a control computer, one can aim at reducing the time interval between each channel update but it cannot be made zero. Hence, it requires high-speed hardware, and an efficient algorithm for control. As the deformable mirror itself has errors in de-energized state, it should be made flat first. When voltage is

applied to one actuator, not only the mirror surface above the actuator is affected but the entire surface of the mirror is getting affected. This kind of influence of one actuator in front of other actuators is to be determined. It is already explained that earlier attempt to experimentally measure the mirror influence function with the interferometer did not give consistent results for the reasons explained before. As the mirror influence function is an important parameter required for control of the deformable mirror, other ways of determining it was probed. One approach was to do a theoretical simulation of the mirror using Finite Element Analysis

As the adaptive mirror is very thin, one should know its mechanical strength. Applying voltage to the electrostatic actuators can locally deflect the membrane and local responses are superimposed to form the necessary optical figures like a flat surface, parabola or any arbitrary surface. A low-stress nitride membrane suspended on edges of a window forms the flexible mirror. The membrane is tensed, so its shape depends only on the boundary conditions. Released membrane is at least as plane as the surface of the substrate before etching.

For finite element analysis, membrane model can be used for statistical description. Thin plate model is not applicable to membranes with aspect ratio in the order of a few thousand.

### 7.3.1.1 Physical properties of membrane mirror

Deflection  $U(x,y)$  of a stretched membrane under an external load  $P(x,y)$  is given by the Poisson equation

$$\Delta U(x,y) = \frac{-P(x,y)}{T} \quad (7.1)$$

For electrostatic actuation  $P(x,y)$  is given by

$$P(x,y) = \varepsilon\varepsilon_0 \left( \frac{V(x,y)^2}{d(x,y,P)^2} \right) \quad (7.2)$$

$$T = \frac{Eh\delta^2}{2(1-\nu)} \quad (7.3)$$

Where  $\epsilon \in \epsilon_0$  is the dielectric constant of air,

$V(x, y)$  is potential distribution on the actuator,

$d(x, y)$  is distance between actuator and membrane

$E$  is the Young's modulus

$h$  is the thickness of membrane

$\nu$  is Poisson ratio of membrane material

$\delta$  is in plane membrane elongation due to stretching

Changes of membrane tension caused by membrane deflection are considered to be negligible.

$$\text{Frequency of first resonance } f_T = \frac{\alpha\sqrt{T}}{\rho h A} \quad (7.4)$$

$\alpha$  is a coefficient depending on the shape, for a circle  $\alpha = 4.261$ . The deformable mirror consists of a thin silicon nitride (Si N) layer coated with aluminum (Al) with the following parameters

$$\begin{array}{llll} \text{Si N} & d_1 = 0.6 * 10^{-7} \text{ m} & \delta_1 = 4 * 10^{-4} & E_1 = 4 * 10^{11} \text{ N / m}^2 & K_1 = 8 * 10^{-7} \text{ K}^{-1} \\ \text{Al} & d_2 = 0.1 * 10^{-7} \text{ m} & \delta_2 = 0 & E_2 = 0.7 * 10^{11} \text{ N / m}^2 & K_2 = 250 * 10^{-7} \text{ K}^{-1} \end{array}$$

37-channel membrane mirror consists of a 15 mm diameter circular membrane of thickness of 7 micron, of which 6 micron is silicon nitride and 1 micron is aluminum. This membrane is mounted in a PCB with spacer, on which 37 hexagons shaped actuators are etched on it. The center-to-center actuator distance is 1.75 mm while actuator structure is located within a 12 mm dia. circle under the mirror membrane. Each actuator is a hexagon of 1.5 mm size. The central actuator is surrounded by other actuators in three rings with 6, 13, 17 actuators. Voltage applied to each of these rings must be inversely proportional to the square of the average distance between the chosen actuator and the deformed membrane in order to achieve a uniform distribution of the membrane curvature. The deformation at a given point on the mirror surface depends on all

actuator signals. FEM analysis of the membrane response can be used to calculate membrane deformations for a given voltages on the actuators i.e. the mirror influence function. Linear approximation for membrane equation is adequate. Based on the influence function calculated with FEM model, a principle components analysis of the mirror is undertaken. A singular value decomposition of the mirror's influence matrix allows a least square inversion. This provides a simple way of calculating the actuator electrode voltages required to give least square correction.

$$\text{The simplified membrane equation is } \nabla^2 z(x, y) = \frac{-P(x, y)}{T} \quad (7.5)$$

Where  $z$  is deformation,  $P$  is electrostatic pressure and  $T$  is membrane tension.

At the edges the value of  $z$  is 0.  $P = \frac{\epsilon_0 V^2}{d^2}$ ,  $d$  is the distance between membrane and electrode and  $d^2 = (d_o + z)^2 \approx d_o^2$  is valid when  $z$  is small and the membrane equation reduces to a Poisson equation.

### 7.3.1.2 Control voltage matrix

If  $W$  is the mirror surface,  $e$  is the electrostatic pressure

$$W = A e \quad (7.6)$$

Where  $A$  is the influence matrix of the mirror. The actuator signal that gives a least square fit to a given wave  $W$  is

$$e = A^{-1} W \quad (7.7)$$

The aim of this FEM analysis is to find the mirror influence function and electrode control matrix for a given surface. The FEM program computes the displacements caused at the 37 locations of the actuator by the application of a unit force at each of the locations individually (74). Because of the nature of the membrane mirror, the pressure load acting in front of one actuator will deform the entire mirror. These 37 deformation values per unit value of pressure form the mirror influence function. Each of the 37 actuators are pressure loaded in turn one at a time and deformations per unit pressure is computed to give all the 37

columns of the influence function. The maximum amplitude the membrane gives for the same voltage for the central actuator and the other actuators distributed in the first, second and the third ring is shown in fig. 7.11. Even though the size of the actuators is given in the models, the foot prints of the actuators could not be seen in the in Fig. 7.11 but the LTP measurement in Fig. 7.10 clearly shows the foot print of the actuator.

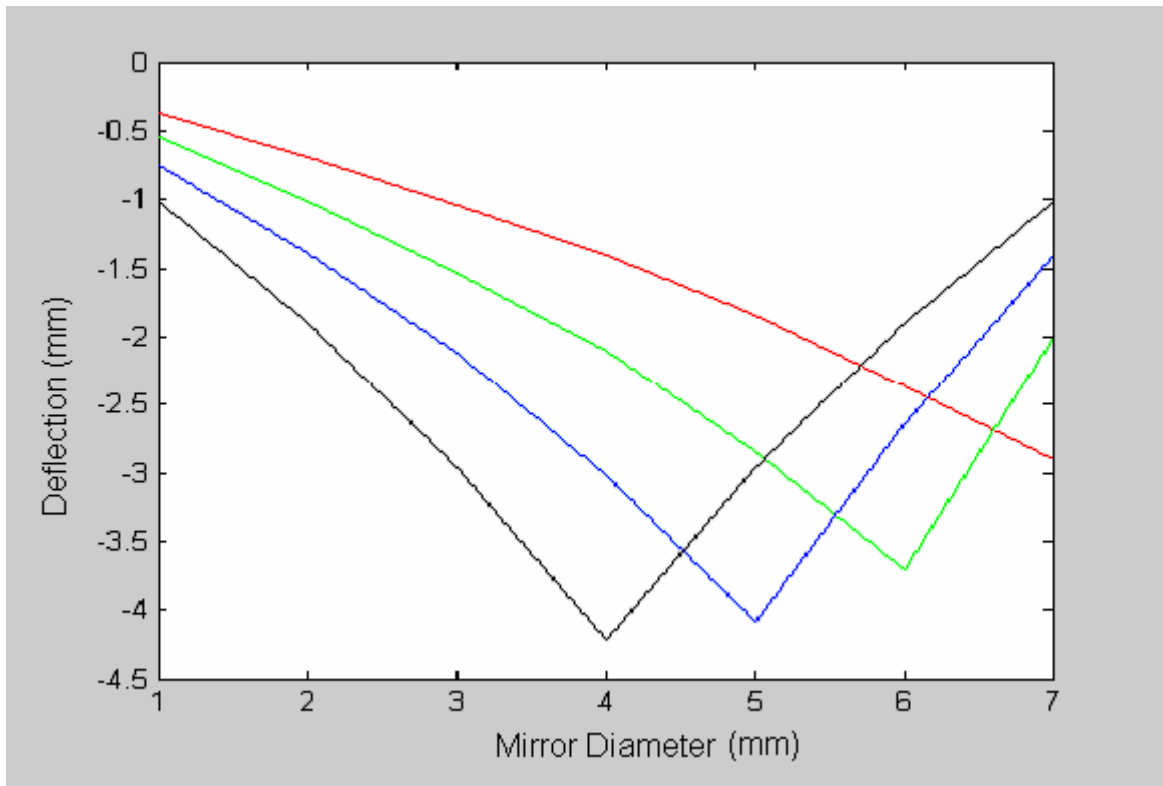


*Fig. 7.11 Actuator positions against relative deflection. In X axis, 4 corresponds to the central actuator position, 3 and 5 correspond to actuator in the first ring, 2 and 6 correspond to actuator in the second ring and 1 and 7 correspond to actuator in the third ring. Only deflection in right half is shown.*

The 3-D view generated from the Finite element data when all actuators are applied equal voltages is shown in fig. 7.12 and matches with LTP results.

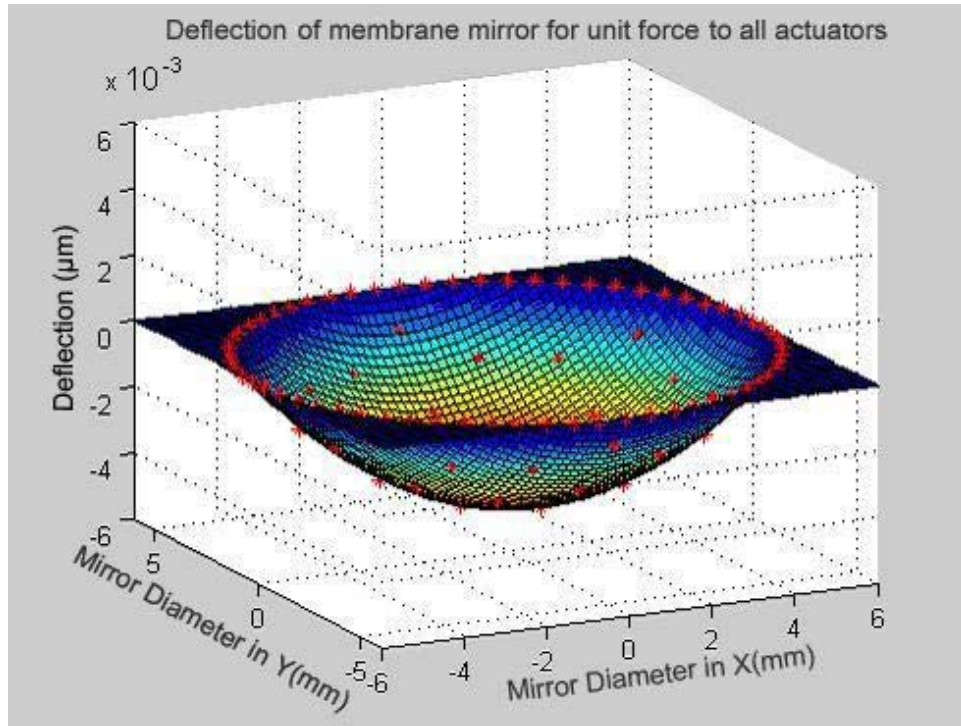


*Fig. 7.12 3-D view generated from FEM data. The graph shows the shape of the mirror when equal voltages are applied to all actuators*

One of the major inputs for accurate control is to measure how these mirrors function for a given set of control voltages. In other words, these two mirrors have to be calibrated using certain reliable and acceptable procedure. Though Interferometric methods offer a choice, it is found that the DMs produce hundreds of fringes when high volt is applied but the interferometer could not reduce data from more than 10 fringes. Saxena had developed a Long Trace Profilometer (48) to measure the parameters of unconventional optics. A Long Trace Profilometer (LTP), in this respect offers a more convenient choice for sufficiently large range and accuracy. The performance of the mirrors for varying control voltages is to be determined experimentally for accurate control. We have tested the tip-tilt mirror and the MEMS based deformable mirror with the in-house developed LTP. The following pages give detailed procedure of testing and a brief description about the LTP which was designed and developed primarily to

measure the profile of the long, non-circularly symmetric, grazing incidence optics. It suited quite well for the calibration of these adaptive optics mirrors.

### 7.3.2 Brief introduction to in-house developed Long Trace Profilometer (LTP)

The LTP belongs to the class of “slope measuring “ interferometer rather than the “height measuring “ interferometer. It measures the phase difference between two co-linear probe beams as they move across the surface. It is reasonably insensitive to vibrations which makes it suitable for use in normal laboratory or optical shop environments and becomes a specific choice for the metrology of the long flat and spheroidal mirrors, both during fabrication and post evaluation.

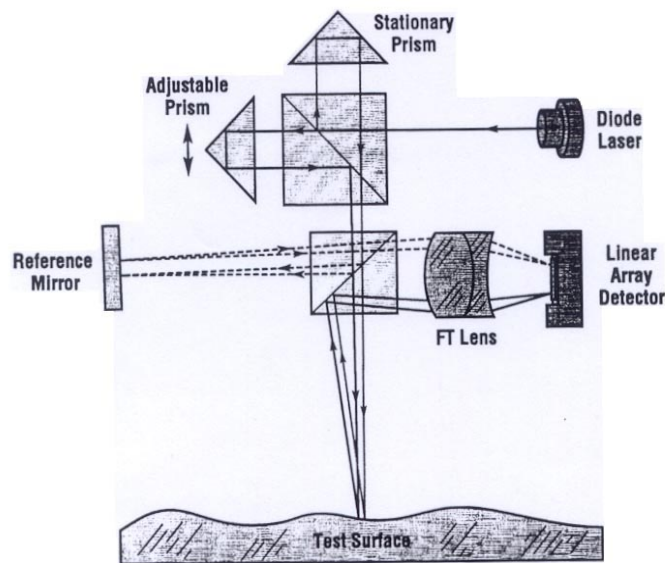


Fig. 7.2 Optical setup of typical LTP

**SCHEMATIC OF LTP USING POLARISING SHEARING INTERFEROMETER**

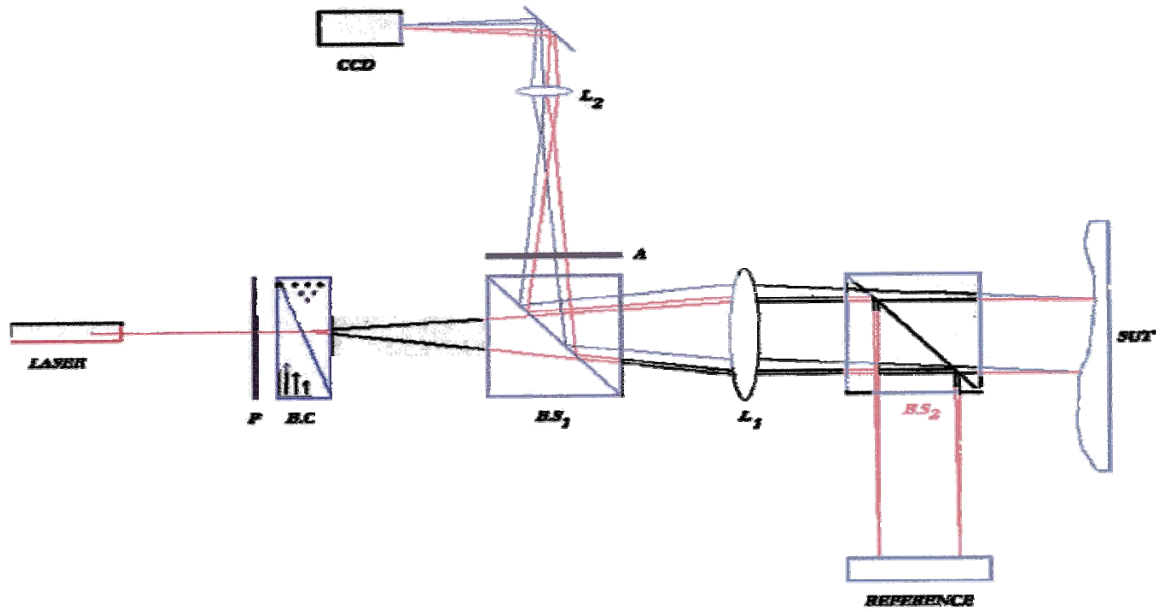


Fig. 7.3 Optical layout of the LTP using shearing interferometer principle.

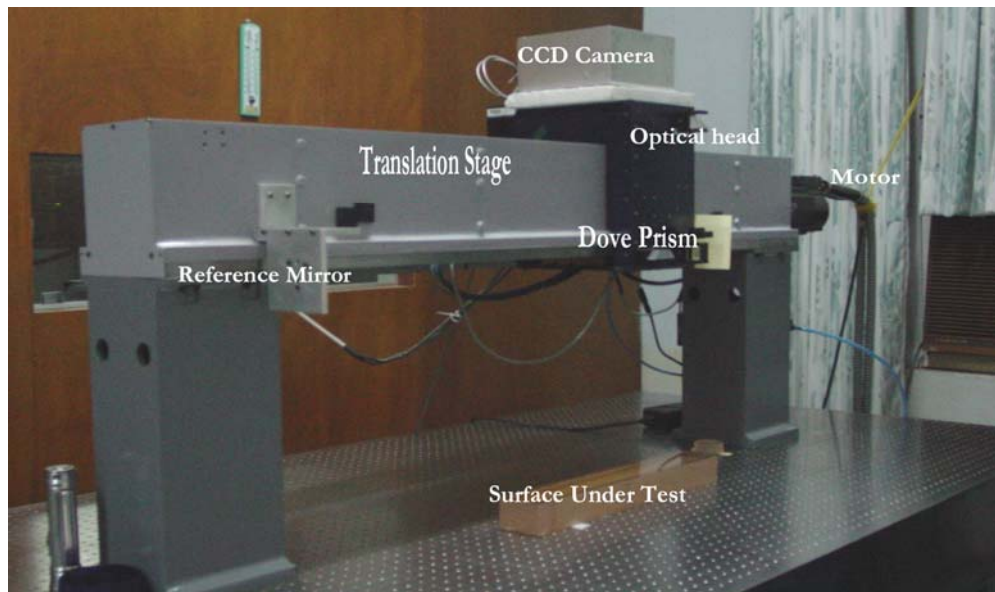


Fig. 7.4 Long Trace Profilometer setup in the laboratory

The LTP is basically designed and built for absolute figure measurement of large flats, spheres and aspherics up to about 1000 mm in size, particularly for strip mirrors. A typical LTP optical schematic is shown in fig. 7.2. The new system uses lateral Shearing Interferometry principle as shown in fig. 7.3.

This instrument is capable of measuring profiles of 900mm long mirrors with accuracy of tangent errors  $\leq 0.25$  arc sec. Fig. 7.4 shows the actual instrument. It basically consists of laser source, beam splitter, reflecting optics, shearing interferometer and the detector, which is a CCD camera. The instrument involves building of the optical head and mechanical translation stage including instrument computer control, data acquisition and reduction procedure. It is a highly sensitive instrument, which involves highly sophisticated optical and mechanical setup and precision control system.

The tip tilt mirror and the deformable mirror required for wavfront control was characterized by using LTP (73). The hysteresis noticed in these actuators can be eliminated by closed loop control with position sensors. We have tested the tip-tilt mirror performances using LTP and found it to respond to reasonably small correction required in A. O. system. Fig. 7.4 gives the performance actuators for an input signal varying from zero volts to ten volts and back to zero volts. The measurement accurately shows the hysteresis present in all the three actuators.

### **7.3.2.1 Test setup for membrane Deformable mirror with LTP**

The DM was placed under the measuring head of LTP shown in fig 7.4 with mirror surface on top. The Initial adjustments were done such that the laser beam passed through the central actuator. The deformable mirror and the actuator PCB have air gap between them. The PCB is attached to a 44 pin square pin grid array. The mirror is plugged into the 44 pin base. Two flat ribbon cables supply voltages to the actuators from the power amplifier boards.

There are 37 electrostatic actuators present in the adaptive mirror. Voltage up to 250 V D.C. can be given to each electrode. The amplifiers are distributed in

two PCBs. Adaptive mirror electrode structures are connected to a 44 pin square grid array IC base. The mirror assembly is plugged into the IC base. A well regulated variable power supply of 300 V, 1A is used to power the amplifiers. Zero to 3.7 V is produced by DACs for input control words of 0 to FF (hex). This voltage is amplified by 59 times by the amplifier. Hence, each actuator voltage can be varied from 0 to 210 V in increments of 0.85 giving smooth control. The mirror load is mainly capacitive; hence special care is taken to drive at high speeds.

### **7.3.3 Test results of MEMS based 37-channel membrane mirror with LTP.**

The deformation at a given point on the mirror surface depends on all actuator signals. In the OKO mirror, the center-to-center actuator distance is 1.75 mm while the actuator structure is located within a 12 mm dia. equivalent circle under the mirror membrane. Each actuator is a hexagon of 1.5 mm size. The central hexagon actuator is surrounded by other actuators in three hexagonal rings with 6, 13 and 17 actuators around a central actuator.

As the LTP can measure the profile only in a straight line, the mirror was placed under LTP such that the laser beam passes through the center of the mirror and the graphs shown is the profile of the mirror for a line passing through the diagonal. Voltages for all the 37 channels were produced by 37 DACs and the signals were then connected to high voltage amplifiers. The actuators can be given a maximum of 220 V. It is found that when the actuator voltages were off, the initial mirror surface was not flat (Fig. 7.6: 0 volt). When 25 V and 50 V were applied to all actuators, one can see the tendency of the mirror surface to become flat (Fig. 7.6: 25 V, 50 V). It is found by trial and error, that a voltage of 51.4 V applied to all actuators produces a flat surface. The voltages applied to actuators are increased in steps of 25 V and mirror profiles are measured and the data are shown in fig. 7.6 in different colours. From these curves, it can be seen that the useful area of the mirror to generate surfaces depending on the voltage is about 10 mm and the concave surface generated by the mirror

deepens as the voltage is increased. As the position of the actuators is approximately circularly symmetric with respect to the central actuator, the shape of the curves gives the mirror influence function. Fig. 7.8 shows the shape of the mirror when the central actuator (actuator 1) and actuators in the second and third rings (actuators 8 to 37) were given 50 V and the actuators in the first ring (actuators 2 to 7) were given 100 V, a small convex surface at the position of the first actuator can be seen. A 3-D view of this surface is shown in fig. 7.9. When the first actuator alone was given 50 V while rest of the actuators is given 100 V, one can see a flat surface at the position of the first actuator (Fig. 7.10). Perhaps, this may be the first time a direct measurement of the mirror surface was measured which has clearly shown the footprint of 1.75 mm size central actuator on the mirror surface. It can be seen that the position of the center actuator corresponds to 11 to 12 mm in the graph (Fig. 7.9). To find out whether there is any hysteresis present in the mirror, the experiment was repeated by reducing the voltage to the actuators in step of 25 V from 175 V. Fig. 7.7 shows the response of the mirror for 150 V applied in the forward and reverse direction and the two curves match very well showing that the mirror does not have any hysteresis. For 50 V the two curves did not match very well since at 50 V the mirror is not tensed enough to generate a flat surface, while a voltage of 51.4 V does which was confirmed independently by the null fringes generated in the interferometer. Table 7.1 lists the voltages given to the all actuators and corresponding figures.

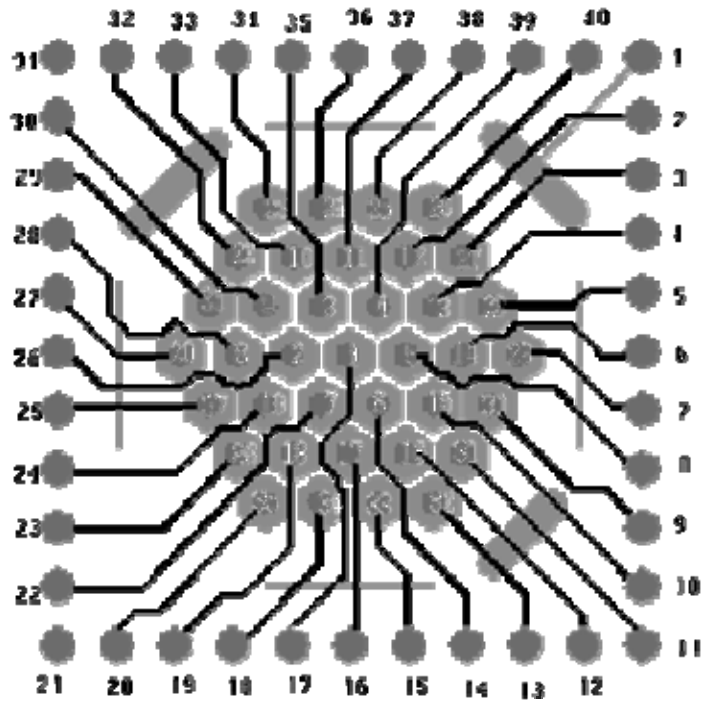


Fig. 7.5 37-channel OKO MMDM actuator layout (As in data sheet provided)

Sl. no	Actuator number	Voltage	Fig. No
1	All actuators	0	6 0 V
2	All actuators	25	6 25V
3	All actuator	50	6 50V
4	All actuators	75	6 75 V
5	All actuators	100	6 100 V
6	All actuators	125	6 125 V
7	All actuators	150	6 150 V
8	All actuators	175	6 175V
9	All actuators	50	7 50 V F
10	All actuators	50	7 50 VR
11	All actuators	150	7 50 V F
12	All actuators	150	7 150 V
13	Actuator1 Actuators 2 to 7 Actuators 8 to 37	50 100 50	8
14	Actuator1 Actuators 2 to 37	50 100	9

Table 7.1 Voltages applied to actuators of DM and the surfaces generated by DM

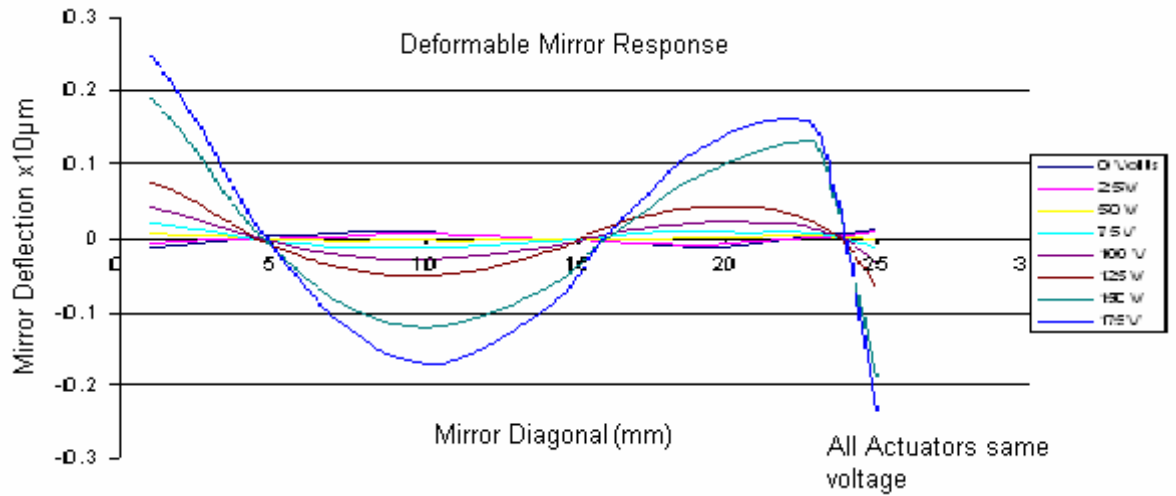


Fig. 7.6 Mirror surface profile as measured by LTP with same voltage to actuators

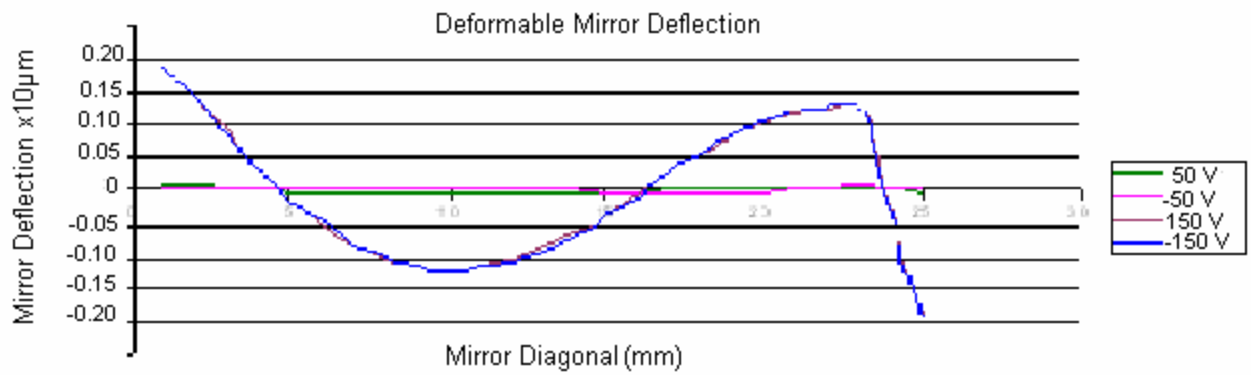
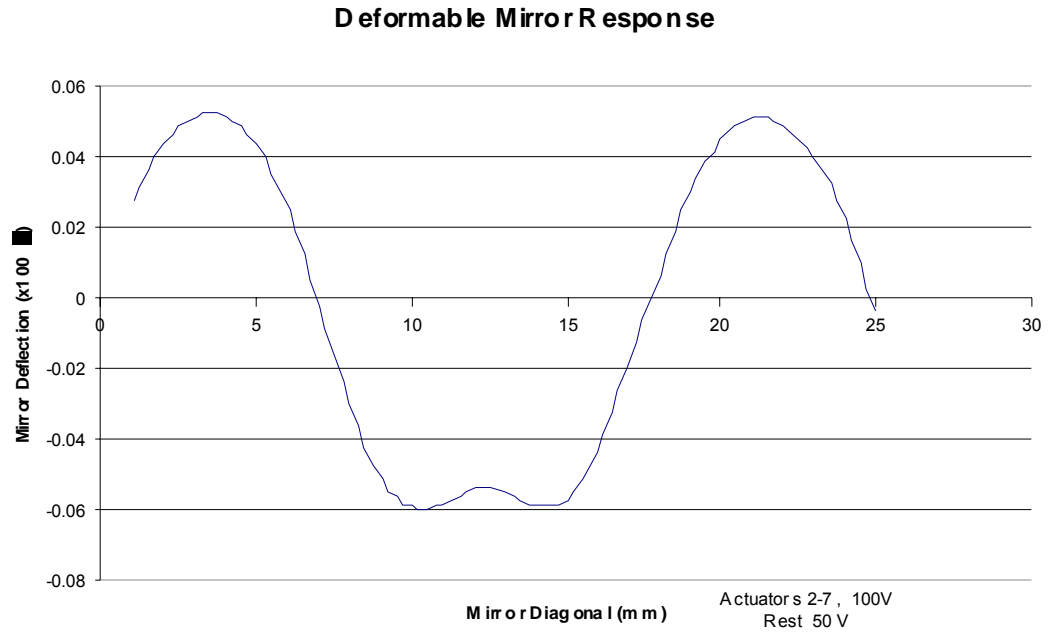


Fig. 7.7 Mirror profile for forward and reverse direction voltages: No hysteresis is seen



*Fig. 7.8 a convex surface profile is seen opposite to central actuator*



*Fig. 7.9 3-D slant view of adaptive mirror for the convex surface shown above*

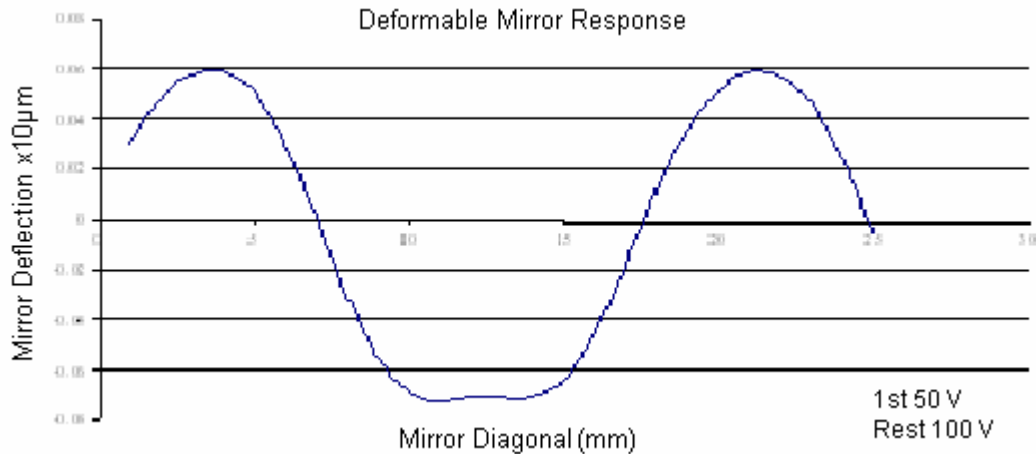


*Fig. 7.10 a flat surface is seen opposite to central actuator*

From the study of the behavior of the tip-tilt and deformable mirrors, it is clearly seen that LTP provides an accurate and suitable means of calibration of adaptive optics mirrors. The range and sensitivity are flexible, and the size of the optics is also not a constraint. Influence function can thus be experimentally determined for these mirrors with much ease. In conclusion, it is seen that the piezoelectric actuator is having hysteresis and a suitable measure is required to compensate it. As for the deformable mirror is concerned, it could be easily converted to a flat mirror with good accuracy by applying suitable voltages to the actuators. It is also seen that concave and convex surfaces of suitable curvature can be generated easily by applying appropriate control voltages to the actuators. The mirror can produce surfaces with smooth profiles only, which is different from what was shown by finite element analysis shown in fig 7.11.

### **7.3.4 Testing of deformable mirror using interferometer**

The membrane mirror was tested in the laboratory with the same set up used to test the piezoelectric mirror. It is found that when the actuator voltages were switched off, the initial mirror surface was not flat. By trial and error, voltages were applied to the actuators to get a flat surface by observing the null fringe in the interferometer.

To create other surfaces, the response of the mirror to the actuator voltages could not be found by the interferometer test method because the mirror produced complicated closely packed fringe patterns from which the interferometer could not produce valid data. Hence theoretical modeling of the mirror was made and the mirror influence function was found by finite element analysis. It is found from interferometry tests that applying 51.4 V to all the actuator gave null fringe, which correspond to a flat surface. Other surfaces could not be measured accurately as the fringes produced were very high.

## **7.4 Result and discussion of various test methods**

### LTP test

- The tip-tilt mirror has hysteresis even though hysteresis compensation circuits are present within drive amplifier. The Amplifier gives only 20 V maximum output instead of 120 V.
- Displacement against voltage for the tip tilt mirror for all the three actuators was found.
- The deformable mirror did not have any hysteresis
- Voltage applied to any actuator produced a very smooth mirror surface. which does not agree with the finite element analysis
- Applying equal voltage to all the actuator created a parabolic surface

### Interferometry test

- Interferometry gave reliable results in the neighbourhood of a flat surface. When large voltages in order of 100 V and more are applied, a large number of closely packed fringes are generated from which no reliable results could be obtained.
- As the DM has initial aberrations, voltage required to make it flat was easily found out by observing the null fringe and when 51.4 V was applied to all the actuators, the DM produced a flat surface

### Finite element analysis

- Pressure acting on one actuator cell is  $1.605 \times 10^{-5}$  gmf / mm<sup>2</sup> for 10 V

- When 100 V is applied to all actuator pressure generated is 1.605 Kgf / m<sup>2</sup>
- When 110 V is applied to all actuator pressure generated is 1.94 Kgf / m<sup>2</sup>
- The maximum deflection for 110 V is higher than the gap between mirror and the actuator. This result contradicts the specification provided by the manufacturer
- When equal voltage is applied to all actuators, the 3-D graph plotted from FEM data matches with LTP results
- When an individual actuator is applied with voltage, the mirror shape shows very sharp bends, where as LTP results show a smooth contour.
- A 37 by 37 matrix of mirror influence function was generated by FEM program. From this data singular value decomposition gave mirror influence function. This data is useful to find out the voltages to be applied to the DM for any arbitrary wave produced by turbulence
- Zernike polynomials could not be computed from any of the above test methods. For this, the Shack-Hartmann (SH) wave-front sensor made during this research work was used.

## Chapter 8

### Control aspects of tip-tilt and deformable mirrors

The three important steps for real-time closed loop wave front-error correction scheme are

- Digital image acquisition of a frame of in-coming wave-front within a few tens of milliseconds
- Compute the errors the in-coming wave-front and create the wave-front surface
- Create a conjugate wave-front surface using electronically controllable mirrors so that the errors in the in-coming wave-front are effectively cancelled.

These three steps are to be executed in sequence within a time frame before an appreciable change occurs in the image scene.

In the earlier chapters, the first two steps are dealt with in detail. The following chapters give details about the third step. This chapter gives the theoretical background and important concepts involved in mirror control.

#### 8.1 Important parameters for control

The Fried's parameter  $r_0$  is an important input to the design of AO system. As a rule of thumb, the number of actuators  $N$  required for high frequency compensation is given by  $N \sim \left(\frac{D}{r_0}\right)^2$  where  $D$  is the diameter of the telescope. The

required stroke is proportional to  $\lambda \left(\frac{D}{r_0}\right)^{\frac{5}{6}}$ . The required actuator response time

is proportional to the ratio  $\frac{r_0}{v}$  where  $v$  is the wind velocity, and it is of the order of

a few tens of milliseconds. The lowest mechanical resonant frequency of a deformable mirror has to be sufficiently higher than the sampling frequency to

introduce a required phase lag. The other problem is the coupling of the response for various actuators. The influence function is generally nearly axis symmetrical for circular mirrors and independent of actuator position. The influence function can be experimentally found by applying voltages to one actuator at a time and measuring the surface generated using suitable methods.

The incoming wave-front suffers distortion both in phase and amplitude; but the phase variation is the predominant one. Once the phase fluctuations are measured, they can be corrected by introducing additional path difference. The phase and the path difference are related by

$$\phi = \frac{2\pi\delta}{\lambda} \quad (8.1)$$

Where  $\delta$  is the variation of the optical path and is given by  $n * e$  where  $n$  is the refractive index of the medium (air) and  $e$ , the geometrical path. Geometrical path difference  $e$  can be introduced by deforming a mirror surface. Deformable mirrors provide short response times, large wavelength-independent optical path difference. Tilt in the wave-front will shift the position of the intensity in the focal plane. Other aberrations change the shape of the pattern and position of the maximum, but do not shift the centroid. Axially symmetric aberrations change the shape but will not alter the position of the maximum or centroid. The shift in the position can be corrected by a tip-tilt mirror platform and other errors can be corrected by a deformable mirror.

In the present work, two mirror systems for wave-front control were chosen, the tip-tilt mirror system based on piezoelectric actuator and a deformable mirror system based on Delft University (DU) continuous membrane mirror. Extensive calibration of these mirrors was carried out using an in house developed LTP and the interferometer as explained in chapter 7. Gleb Vdovin had shown that the DU DM can be used for tilt correction also (75), however, doing so will reduce the dynamic range for higher-order aberrations. It is also shown that the cycle time of tilt correction is different from that of the higher-order corrections. Hence, a two mirror correction system was chosen. The following section describe the different approaches used for these mirror controls.

## 8.2 Control algorithms for tip-tilt mirror

The three actuator tilt mirror platform was explained in some detail in section 4.8.3. Piezoelectric actuators can be applied with voltage range of -25 V to 250 V D.C. They are essentially capacitor load; hence driving them with high voltage amplifier is not very simple. As the piezoelectric material has hysteresis, strain gauge foils are pasted on them to have position feedback. But the measurements showed in section 7.5, that this feedback arrangement did not eliminate the hysteresis completely. Drive signal has to be generated by the wave-front computer. The first two Zernike polynomials computed by the wave-front computer gives the X tilt and Y tilts in the wave-front. Fig 6.2 shows the position of actuators, A, B and C, the lengths and the angles  $\alpha$  and  $\beta$  the two orthogonal axis tilts,  $\alpha$  being the tilt in the horizontal direction and ,  $\beta$  the vertical direction, the following relationship can be derived for vertical and horizontal tilts using the actuator lengths, A, B and C.

$$\alpha = \frac{[A - \frac{1}{2}(B + C)]}{a}. \quad (8.2)$$

$$\beta = \frac{[B - C]}{b}. \quad (8.3)$$

$$Z = \frac{[A + B + C]}{3}. \quad (8.4)$$

Equation 8.4 shows that for equal increase in lengths of all three actuators, the resulting tilt angle is zero. The lengths of the actuators A, B and C depend on the voltage applied to them and the relation between lengths and angles are given below:

$$A = -\frac{1}{3}\beta - \sqrt{\frac{3}{2}}\alpha \quad (8.5)$$

$$B = \frac{2}{3}\beta \quad (8.6)$$

$$C = -\frac{1}{3}\beta + \sqrt{\frac{3}{2}}\alpha \quad (8.7)$$

The actuator lengths are directly proportional to the D.C. voltage applied to them by the high voltage power amplifier. Unipolar, 8 bit DACs, were used for generation of control voltage. A brief discussion about the tilt mirror controller's behaviour analysis is given next.

In conventional control theory, the system can be described by a linear differential equations and the behaviour can be analyzed using linear control theory. Laplace transforms are normally used because it maps linear differential equations to linear algebraic expression. This transformation greatly simplifies the system analysis. For discrete systems, Z transforms are used.

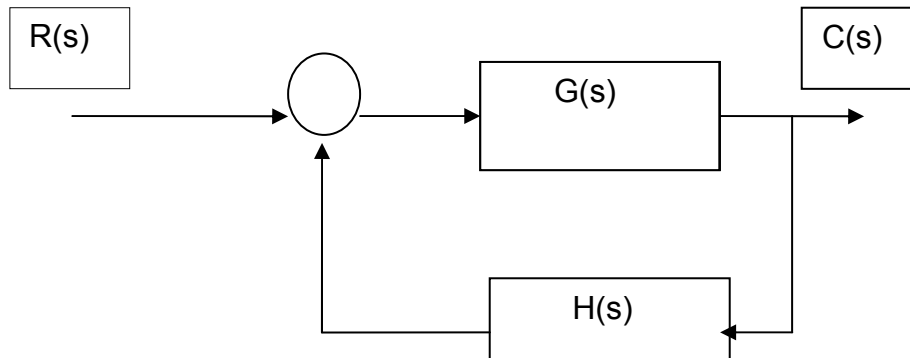


*Fig. 8.1 Standard negative feedback loop*

The tilt correction servo is linear if one neglects the small hysteresis noticed in them. A standard form of negative feedback control system is shown in fig. 8.1. Here, signals are represented in Laplace transform form and the devices, by their transfer functions. A negative feedback control system model for tilt correction servo was extensively studied by Theo ten Brummelaar in his thesis in the University of Sydney Stellar Interferometer (76). If the transfer functions of the gain  $g(s)$  and feedback  $H(s)$  are known, the performance of the entire system can be found. If  $B(s)$  is the transform of the feedback signal,  $E(s)$  is the transform of the error signal, then from conventional control theory, the transfer function is

$$T = \frac{G(s)H(s)}{1 + G(s)H(s)} \quad (8.8)$$

If the transfer functions of gain  $G(s)$  and feedback  $H(s)$  are known, the performance of the entire system can be found. For a real tilt mirror correction system, similar feedback loop circuits can be constructed. Fig. 8.2 shows the tilt correction system as a negative feedback loop. Fig. 8.2 uses the actual components of the tilt mirror system for analysis. Using transfer functions of individual components, linear models can be made. The tilt of the incoming beam is  $R(s)$ , the corrected output beam is  $E(s)$ . The computer system with its measurement of wave-front tilt is  $C(s)$ . The subtraction is done by the tilt mirror itself. There are two functions of primary interest. The first transfer function is for the ability of the mirror to track tilt of the beam.

$$T_{track}(s) = \frac{B(s)}{R(s)} \quad (8.9)$$

and with the blocks shown in fig. 8.2

$$T_{track}(s) = \frac{-G(s)H(s)}{1 + G(s)H(s)} \quad (8.10)$$

The second transfer function describes the ability of the system to measure the incoming beam tilt

$$T_{measure}(s) = \frac{C(s)}{R(s)} \quad (8.11)$$

and with the blocks shown,

$$T_{measure}(s) = \frac{KmG(s)}{1 + G(s)H(s)} \quad (8.12)$$

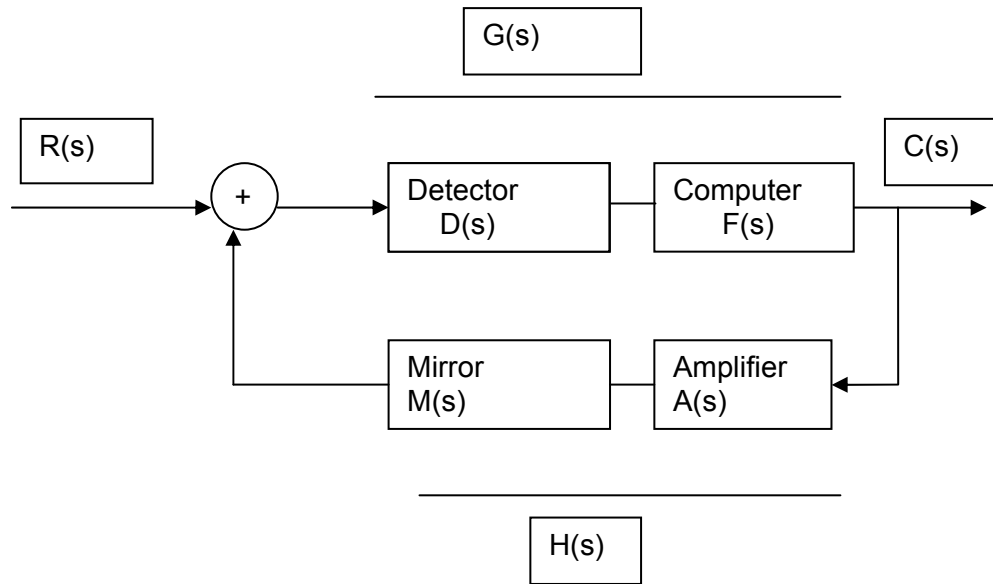


*Fig. 8.2 Tilt correction servo as negative feedback.  $R(s)$  is incoming tilted beam and  $E(s)$  is the corrected optical beam and computer measured tilt is  $C(s)$*

The above equations can be used to determine the usable servo bandwidth for tracking and measurement of beam tilt.

### 8.2.1 Electronic controller configuration

For closed loop image correction system, the wave-front sensor acquires one set of digital images of reference and aberrated images and computes the gradient calculations from the Shack-Hartmann sensor. It is then to be multiplied with the control matrix to generate actuator signals. For some of the AO implementation, dedicated, real-time, digital wave-front computer was built to satisfy the time requirements. Mainly, many digital signal processing (DSP) boards were used to take care of individual tasks like image capture, gradients computation and reconstruction, compensation and DM output. This part of hardware is the costliest of all and any reduction in DSP hardware will reduce the cost. The low cost option is integration of imager and electronic controller. If a powerful DSP core is built into CMOS imager, so that slope vectors are

computed in the CMOS imager, substantial data flow between imager and computation processors can be eliminated. The technology of CMOS imager fabrication allows this kind of integration of the DSP or equivalent processors thus offering single chip camera and controller.

Present general purpose PC speeds have increased substantially, with high throughput I/O buses. Current approach is to use the readily available high speed PCs with high throughput input / output PCI bus based controllers.

### **8.3 Control algorithms for membrane deformable mirror**

The details about 37 actuator deformable mirror and its main characteristics are already discussed in section 7.6. There are 37 degrees of freedom for the mirror control. The main characteristics of the DM are as follows:

- The mirror deflection is proportional to the square of the applied voltage and the mirror mechanical sensitivity is proportional to the applied voltage. To linearize the control, voltage applied to the mirror actuator should be proportional to the square root of the linear voltage calculated by the control system.
- Quantization of control voltages. 8 bit DAC provides 255 equidistant levels of control voltage per channel. This allows for an enormous number of the system degrees of freedom.

There are different control schemes developed by various research groups working in this area. A few schemes for control of adaptive mirrors are briefly explained by Roggemann et. al., (80).

For adaptive mirror control, two models of mirror controls are used.

- Linear control model
- Non-linear control model

In linear model, one has to map the wave-front sensor measurements to the control signals that result in the desired system performance. If the transformation is linear mapping, the control matrix  $M$  has the following form:

$$C = M S_m \quad (8.13)$$

Where  $C$  is a column vector of the control signals and  $S_m$  is a column vector of the measured sub-aperture slopes. In this approach, once slope values are known, and then mirror control signals can be computed using eqn. 8.13. Algorithms for the solutions of this type of formulation have already been discussed in section 4.4.1. In this scheme, information about the optical errors and their magnitudes present in the wave-front are not available. As the DM is tied at the edges, edge errors cannot be fully compensated. Mirrors that have zonal controls are better suited for this type of errors. The membrane's mechanical elasticity and the electrostatic forces between the membrane surface and the actuators determine the shape of the mirror. The deflection or the mirror shape is generally nonlinear with respect to the control voltages. Each actuator modulates the whole surface profile of the mirror, whereas in combination all channels couple together to form the overall modulation of the mirror surface shape within the fixed boundary. As discussed by Lijun Zhu et. al., (77), an exact analytical solution in which membrane and electrostatic equations are used for optimum control voltages is a nonlinear problem in a multidimensional control voltage space. The nature of the nonlinear response and the strong coupling of the control channels make it difficult for one to predict the required control voltages to obtain the desired mirror surface shapes. Nonlinear computation and control models are necessary to control the deformable mirrors. The nonlinear control schemes developed previously are:

- Neural network control using a multilayer feed-forward network structure and an error back propagation algorithm to train the network to map the nonlinear relationship between the mirror shapes and control voltages. This model was developed by Vdovin (78). This approach requires a very large set of training data samples covering all possible mirror surface patterns generated by varying control voltages applied to multiple actuators.
- The nonlinear computation model is based on using numerical methods for solving the membrane equations with nonlinear electrostatic actuator

characteristics. The mirror surface deformations are described by nonlinear partial differential equations and the actuator voltages are determined by solving these equations with numerical methods with known boundary condition (79).

- Lijun Zhu et. al., (77) developed a control algorithm to achieve optimum surface shapes based on the characteristics of experimentally measured mirror shape responses. Based on experimentally measured mirror shape responses with respect to control voltages, they have defined a control signal that is monotonic function of the control voltage and developed a quasi-linear mirror response model. Using this model, they have developed a control signal-updating algorithm by adaptively adjusting the control voltages of all electrodes by using an iterative process. It is shown that this adaptive algorithm could correct the shape of the mirror after about 20 iterations, each iteration taking 1 second to complete. The delay between image acquisition and control of the mirror is about 20 seconds and it is partly due to CCD read out time and the rest due the number of iterations done.

#### **8.4 Adopted control scheme for deformable mirror**

As explained in section 7.6, the deformable mirror shapes were measured in the laboratory using the LTP for different actuator voltage configurations. It is found from the experiment (Fig. 7.6) that the deformable mirror has inherent aberrations and it needs to be corrected first. The closed loop correction time required for control is about 20 milliseconds for best seeing conditions. The computation time of the nonlinear control algorithms discussed in section 8.7 is higher than the required time for closed loop control. This is because the correction is done iteratively and convergence can come after 20 or more iteration. Correction of static wave-front errors or wave-front errors changing slowly can adopt this approach.

The new approach to reduce the cycle time is to reduce the time required for computation assuming that the image acquisition time is already optimized to the extend possible. The control scheme being proposed now is a modification of Lijun Zhu's method. Instead of iteratively correcting the mirror shape, relationship between Zernike polynomial and control voltages are measured in a calibration setup. This requires a good wave-front generator which generates wave-front errors in terms of Zernike polynomial. The inability of the mirror to correct certain aberration has to be taken into account. Once the relationship between Zernike polynomial and actuator voltages are established, addition of voltages for any combination of Zernike polynomial can be found. Instead of solving mirror control equations each time, the table can be referred to get the voltages. The look-up table or control equations are to be created with the same set-up that will be used for final correction and this scheme is explained in the next chapter

## Chapter 9

### **Closed loop Wave-front corrections - Laboratory experiments and results**

Based on the characteristic studies of tip-tilt and membrane deformable mirror described in earlier chapters, a new approach for close loop image correction has been demonstrated. This chapter describes the laboratory experiment to establish a close loop wave front correction procedures. Adapting experimental calibration methods, closed loop corrections have been performed. Actual optical set-up, control electronics, software and algorithms developed have been described in detail. Results of a close loop corrections are presented.

#### **9.1 The experimental setup for calibration**

The total system conceived for calibration of control mirrors consists of the following sub-system.

- 1 Collimated beam generation using pin hole, fibre optic light source and optical beam reducers for beam size reduction
- 2 Wave-front Sensor
- 3 Wave-front error computation.
- 4 Tip – tilt error correction by tip-tilt mirror system
- 5 Low order wave-front error correction by adaptive mirror system

Before attempting to do closed loop error correction, the system is to be calibrated in terms of Zernike coefficient against control voltages required. The optical layout for the experimental setup created in the laboratory is shown in Fig. 9.1. In this figure, T is a cassegrain telescope of 30 cm aperture. FM is a flat mirror used for auto-collimation. BS1, BS2, BS3 and BS4 are beam splitters; L1, L2, L3 and L4 are achromatic lenses, TT is the tip-tilt mirror and DM is the deformable mirror. SH is the Shack-Hartmann lenslet array, CCD is CCD.

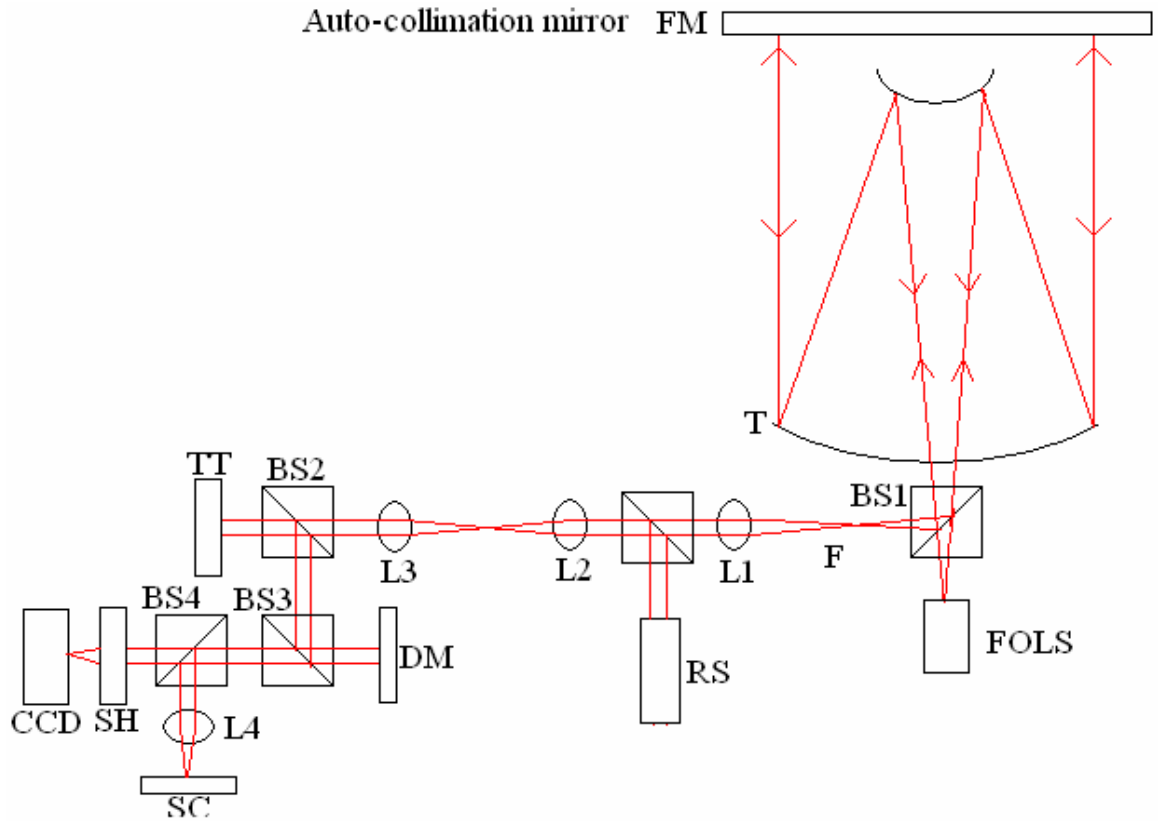


*Fig. 9.1 Optical layout of the experimental setup*

camera of the wave front sensor and SC is the science camera. RS is a reference source and FOLS is fibre optic light source with a pin hole. Normally, a parallel beam of light falling on the primary mirror is focused on the secondary mirror and gets reflected and gets focused at F. Parallel beam is generated by the secondary and primary mirror combination and the beam is reflected by the collimating flat mirror FM and gets focused back at F after being deflected by beam splitter BS1. L1 makes the beam parallel; L2 and L3 combination constitute a beam reduction unit.

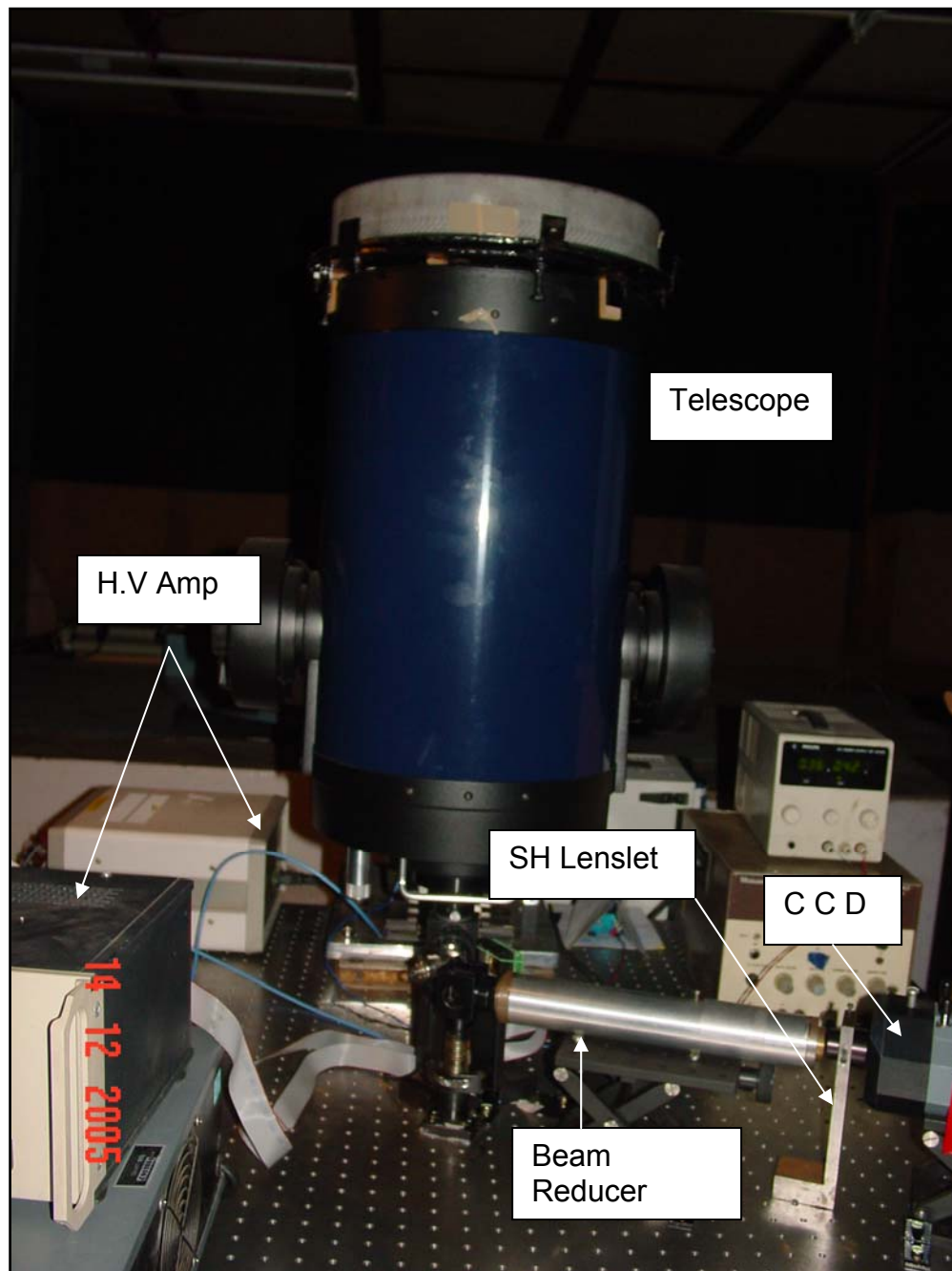


*Fig 9.2 Close-up view showing the telescope with other components used in the laboratory experiment. The long cylinder seen in front in line with CCD camera is the beam reduction unit. The lenslet array is at the end of beam reducer.*

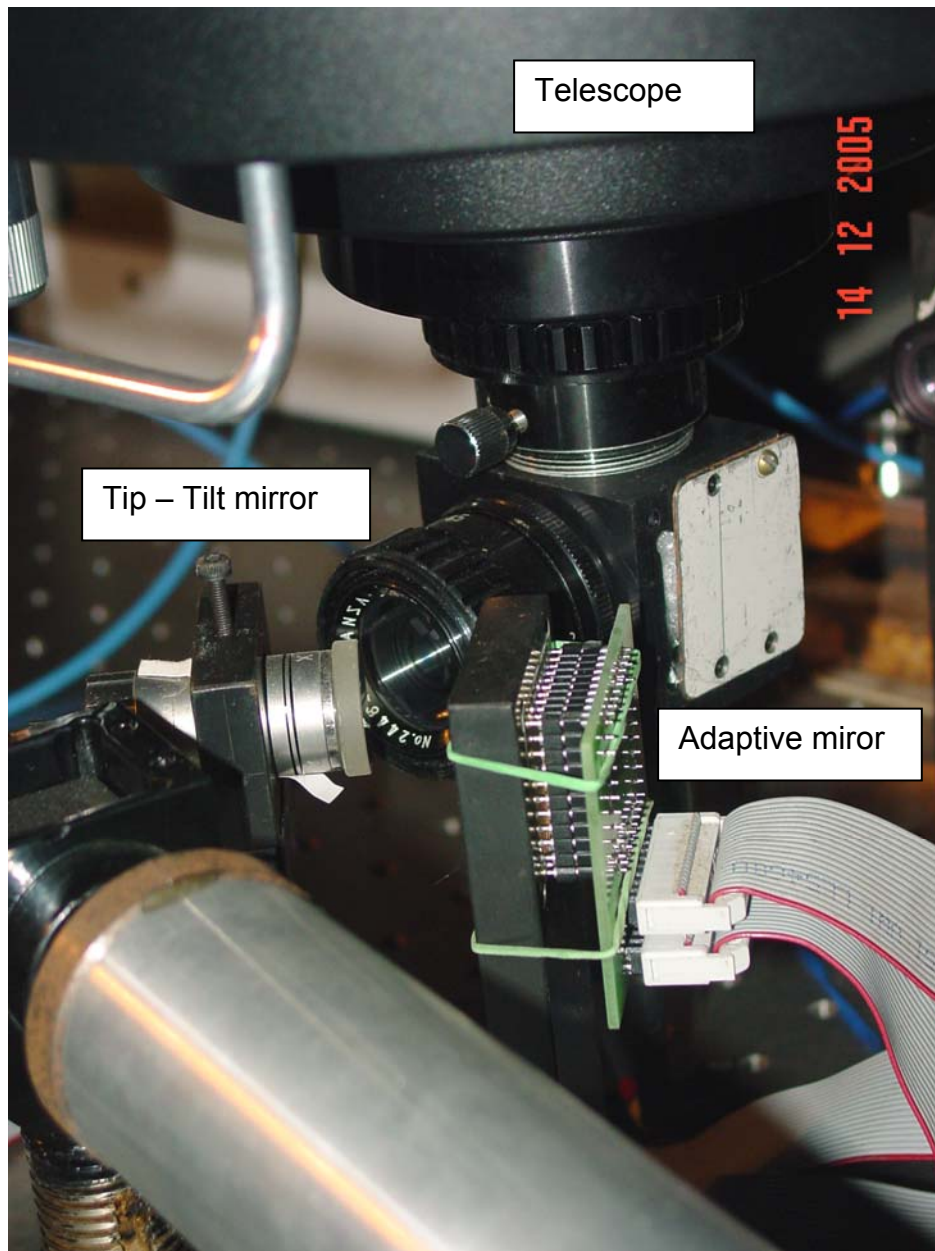


*Fig. 9.3 Picture of another view of the experimental setup showing tip-tilt mirror and adaptive mirror*

The beam is then reflected by the tip-tilt mirror TT, beam splitters BS2, BS3 and deformable mirror DM and passes through the Shack-Hartmann lenslet array SH and reaches the wave-front sensor camera CCD kept at the focus

point of lenslet array. The above configuration may have light loss but it does not introduce any aberration to the optical beam, hence calibration becomes easier. First, a reference Shack-Hartmann image is taken by allowing the beam from the reference source (RS) and then the aberrated image from telescope starting from FOLS is taken. Using these two images, the errors in the wave-front are computed. The tilts in the wave-front are corrected by the tip-tilt mirror and the high frequency errors are corrected by the deformable mirror.

The photo of the experimental setup are shown in fig. 9.2 and 9.3. The schematic of experimental setup with electronic sub-system for calibration and control of tip-tilt mirror and adaptive mirror is shown in fig. 9.4.

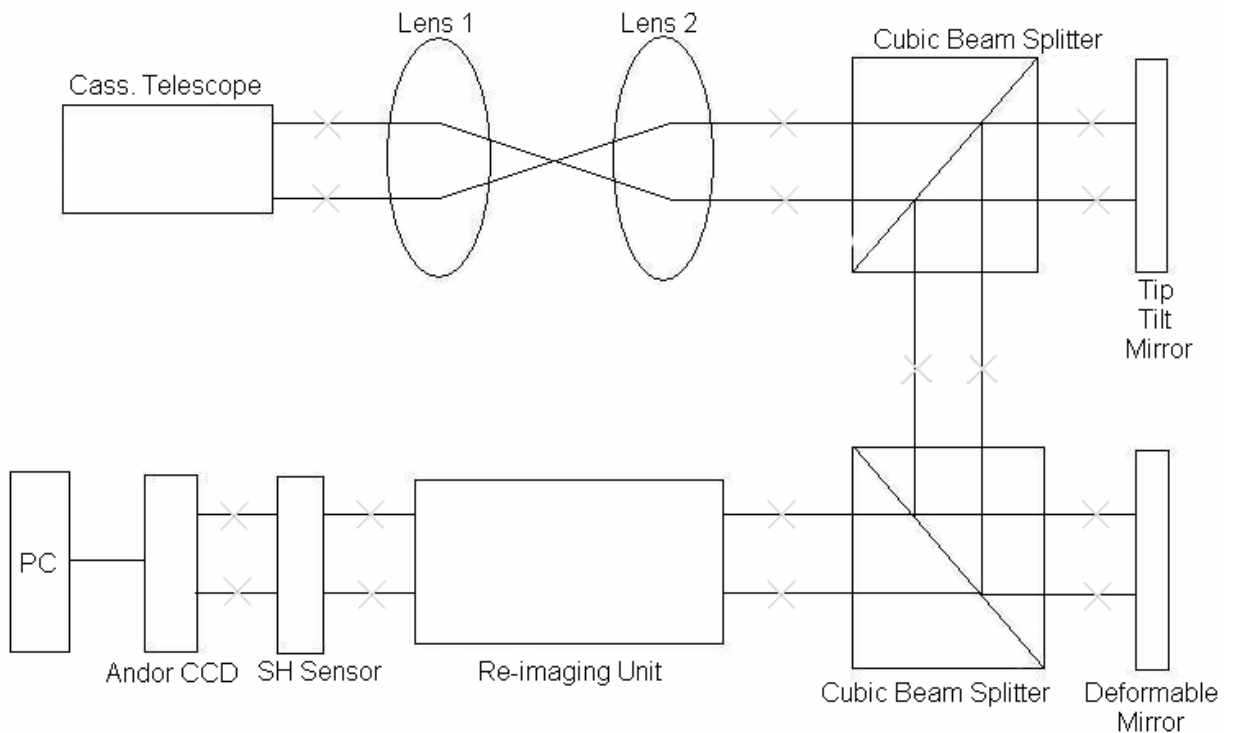


*Fig. 9.4 Experimental setup for calibration of tip-tilt and deformable mirrors*

The reference beam is generated by the laser source and beam expander. The beam then passes through lenses L1 and L2. The beam then reaches the tip-tilt mirror and the deformable mirror through beam splitters. The deformable mirror reflects the beam towards the Shack-Hartmann lenslet array. The imaging camera is kept at the focal distance of the lenslets,. In an unbiased mode, voltages applied to the actuators of the deformable mirror produce an electrostatic force, which attracts the mirror towards the actuators. The mirror surface cannot be moved up from the flat surface. Hence, an optical bias in the wave-front is created by using the lenses L1 and L2.

In normal telescope operation, the reflected beam from secondary mirror comes to focus at the cassegrain end where imaging camera like CCD is mounted to capture the images of the stars. In the real-time correction mode, the beam of light, after the cassegrain focus is made into a parallel beam and a portion of the beam is sent to a wave-front sensor for optical aberration measurement. The errors are found in terms of Zernike coefficient Z1 to Z14. Z1 and Z2 are used to correct the X and Y tilts in the wave-front using the tip-tilt mirror. Deformable mirror is used to correct the Z3 to Z14 error terms.

### **9.1.1 Details of electronic control**

Separate driver software was developed for the imaging camera in order to have the real time data acquisition capability. Other Interface card having 40 channels of Digital to analog converters generate the signal voltages required for TTM and DM.

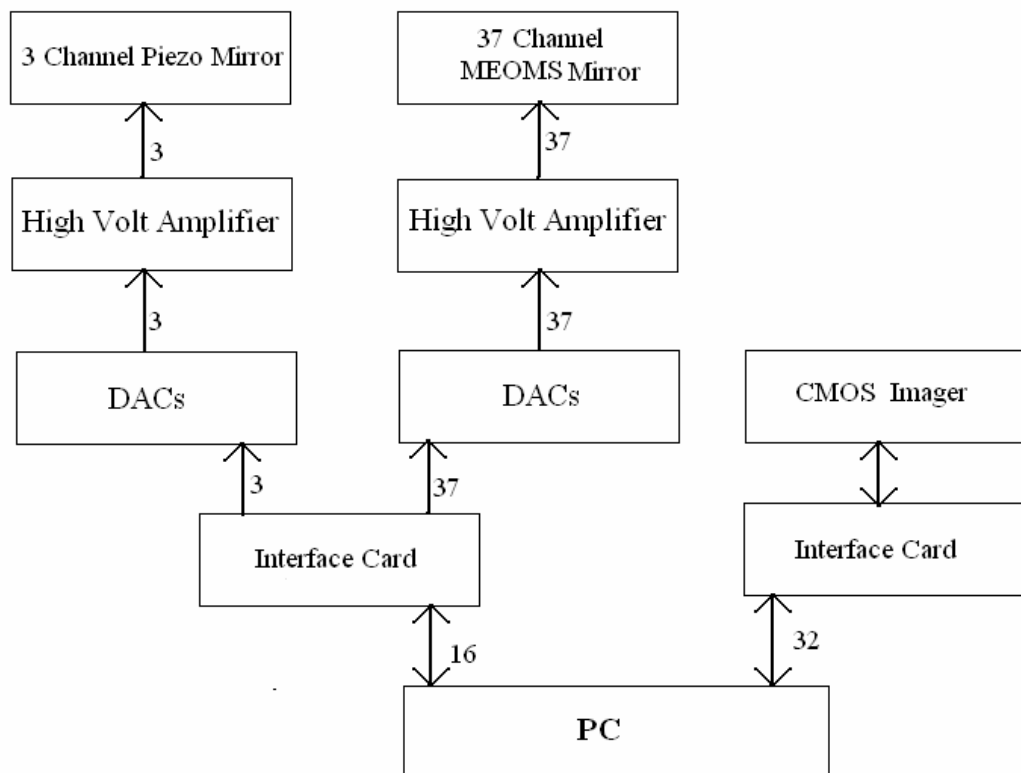


*Fig. 9.5 Schematic of electronic control of tip-tilt mirror, deformable mirror and wave-front sensor camera*

The signal voltages are amplified for tip-tilt mirror by a three channel power amplifier. Another set of 37 high voltage amplifiers are used for control of DM. A continuously variable, regulated, low ripple 300 V DC power supply is used to power the DM amplifiers. The PC based electronic control of the tip-tilt and deformable mirror is shown in fig. 9.5.

## 9.1.2 Software and algorithms

From a reference frame and an aberrated frame images, x centroids and y centroids are found. The next step is to find the differences of x centroids and y centroids of reference image and aberrated image. This difference value directly represents wave-front slope at each sub aperture in X and Y direction. From these slope values, one has to reconstruct the wave-front. For this, modal wave-front representation is chosen i.e., polynomial representation. The algorithm developed to reconstruct the wave-front is detailed below.

Step1: Grab the reference image from Shack-Hartmann sensor.

Step2: Calculate the centroid positions of focal spots of reference image.

Step3: Grab the aberrated image from Shack-Hartmann sensor.

Step4: Calculate the centroid positions of focal spots of the aberrated image.

Step5: Calculate the difference of the centroid positions of reference image and those of aberrated image. These differences represent average wave-front slope values at each sub aperture. Arrange these differences in a matrix [S].

Step6: Normalize the reference plane centroids such that all spots come inside the unit circle

Step7: Calculate derivative of Zernike polynomial, of required degree N, w.r.t. x and y, at M reference spots inside the unit circle. Arrange these values in a matrix Z of size 2xMxN.

Step8: Fit this matrix [Z] and slope value matrix [S] in to polynomial by least square fitting method, i.e.,

$$[Z][A] = [S] \quad (9.3)$$

Step9: Find the coefficients  $A_i$  of Zernike polynomial by matrix inversion, i.e.,

$$[A] = [Z]^{-1} [S]. \quad (9.4)$$

Step10: Reconstruct the wave-front using these coefficients and display wave-front.

The centroid of a sub aperture are calculated by identifying circular objects and finding their centroids. For object identification, one has the control parameters like radius and there is definite relation between the control parameter and noise. Usually, for Shack-Hartmann lenslet array, quad cell algorithm is used. But this approach needs precise alignment of CCD pixels to the lenslet positions. Here, centroiding with object identification is used. This has the following major advantage.

(i) The concept of sub aperture is not there, allowing the wide variation of lenslet image position in the CCD.

(ii) As only a small area covering the lenslet image position is used for computations, the accuracy of centroid calculation is high. The results given in table 5.1 for CMOS imager shows increasing tilts for increased voltage for tip-tilt mirror proving the correctness of the new method. Fig. 9.6 shows the lenslet images of an aberrated wave-front.

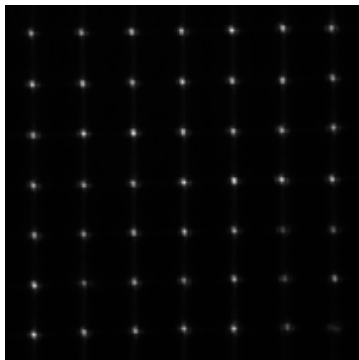


*Fig. 9.6 Image of 7x7 lenslet array with re-imaging optics. X and Y centroids of lenslet positions are computed from the location of the lenslet images.*

centx1 =

14.5000	39.2830	64.7846	89.5294	113.8500	138.9848	163.2273
13.7907	39.0000	63.8542	89.2222	113.7727	137.5455	162.0000
13.4872	38.9737	63.7727	88.0000	112.7727	137.2222	161.0000
13.4872	38.4681	63.2093	88.2222	112.2857	136.7222	160.2222
13.0000	37.4898	63.0000	87.5000	111.5435	135.7222	160.2273
12.0526	37.0606	61.9403	86.5254	111.2222	135.4167	159.3385
11.7727	36.0566	61.0000	86.2923	110.8163	135.5000	159.3696

centy1 =

14.0000	14.8462	14.7358	15.0147	15.7833	15.6364	15.3182
39.6047	40.0000	40.5417	40.2222	40.6818	40.1591	40.5000
64.8974	64.8947	65.6818	65.5000	65.6818	66.2222	66.5000
89.8974	90.4255	90.6744	91.2222	91.1852	91.2222	91.2857
115.4082	115.5000	115.5000	116.0000	116.3696	116.2778	116.3182
140.6418	140.5763	140.8772	140.9545	141.2222	141.9167	142.6000
165.7692	165.6818	166.3019	166.5000	166.2857	167.0000	166.8696

*Table 9.1 centX1 and centY1 are centroids computed at the lenslet location for an aberrated image.*

When the reference image is perfect, the centroid values of X (centx1) will be almost equal in each column. In the same way, the Y centroids (centy1) in each row should be almost equal. Some of the optical components are to be mounted in precision X, Y and Z movements so that the precise alignment of optical components can be easily done.

## 9.2 Determination of control voltages for tip-tilt mirror

For calibration of tip-tilt mirror, the deformable mirror is used as a reflecting mirror. Three DAC channels out of 40, available in the I/O interface card were used to produce control signals for the three actuators.

Actuator A			Actuator B		
A	Z1	Z2	B	Z1	Z2
10	-0.024	-0.0253	10	-0.014	-0.031
20	0.0809	0.0129	20	0.011	-0.060
40	0.09	-0.0075	40	-0.026	-0.122
60	0.166	0.0334	60	-0.062	-0.165
80	0.2398	0.0529	80	-0.140	-0.262
A0	0.2176	0.0843	A0	-0.106	-0.335
C0	0.2924	0.085	C0	-0.134	-0.401
E0	0.4112	0.0748	E0	-0.193	-0.474
FF	0.4751	0.0526	FF	-0.243	-0.562

Actuator C			
C (DAC input )	DAC Volt	Z1	Z2
10	0.237	-0.0268	-0.0218
20	0.468	-0.0316	0.0118
40	0.932	-0.0750	0.0664
60	1.395	-0.1026	0.1358
80	1.858	-0.1658	0.0237
A0	2.321	-0.1706	0.2951
C0	2.785	-0.2194	0.3755
E0	3.248	-0.2811	0.4711
FF	3.679	-0.3009	0.5343

Table 9.2 Zernike coefficients

The remaining 37 channels were used for adaptive mirror control. Piezoelectric amplifier with its preset gain, the output voltage goes up to 27 V. The output of the amplifier is connected to tip-tilt mirror system. Input word for DAC belonging to actuator 1 is changed from 0 to 255 in steps of 32 and the X and Y tilt as measured by the SH wave-front sensor is noted. The same procedure is repeated for actuators 2 and 3 and the tilt values are noted. between Zernike coefficients Z1 and Z2 and their corresponding actuator voltages.

Table 9.2 shows the relationship between input word and X, Y tilts for the three actuator, A, B and C are three piezoelectric actuators and the column under that are DAC input numbers in hexadecimal. Input number FF gives 3.679V from the DAC. It can be seen that Zernike coefficients show good variation for voltage applied to the three actuators. Z1a, Z2a; Z1b, Z2b; Z3a, Z3b are first two Zernike coefficients (Tilts) measured with S-H sensor for the control voltages applied to actuators A, B and C respectively. It is seen that for the actuator positions as shown in fig. 6.2, varying voltage to the actuator A alone gives tilt in Y only with X tilt almost constant. Varying voltage to actuator B gives tilts in both in X and Y with negative sign. Varying voltage for actuator C alone gives +X tilt and -Y tilt. With the focal length of the lenslet array taken into account, this calibration gives the relation

### **9.3 Determination of control voltages for membrane Deformable Mirror**

The micro-machined adaptive mirror has 37 actuators. Out of the 40 channels of DAC, 37 channels are connected to high voltage amplifiers of the deformable mirror. With the gain of 59, the output of high voltage amplifiers can go up to 218 V. As Zernike polynomials are being used to represent wave-front errors for calibration, testing and control, one should be able to generate known wave-fronts of aberrations by applying voltages to the actuator. For a plane wave-front, when equal voltages are given to all the actuators, the deformable mirror takes the shape of a parabola (75), which changes only the 4<sup>th</sup> Zernike term (Z4).

Hence, it is a very good test to validate the algorithms used for wave-front sensing and adaptive mirror control. .

The experimental setup used for calibration and testing of deformable mirror is shown in fig. 9.1. Here, only the deformable mirror voltages are varied, while the tip-tilt mirror voltages are kept at zero. The following steps give details of the adaptive mirror calibration.

Step 1: Using the computer, generate 0 V in all the 37 channels using the DAC card. After amplification the voltages reach the adaptive mirror actuators.

Step 2: Using the Shack-Hartmann camera, capture a picture of Shack Hartmann spots.

Step 3: Increase the voltage by DAC in steps and capture corresponding images.

Step 4: Calculate Zernike polynomials for each image.

Step 5: Note down the Zernike polynomial of interest for which input control voltages were generated.

Step 6: Plot a graph of the Zernike coefficient value Vs Voltage applied to the adaptive mirror.

Step 7: Find out an equation for the relationship and this formula can be used for computation of required voltage for the measured Zernike coefficient by the Shack-Hartmann sensor.

Following is the details of actual procedure adopted for control of DM. The pixels of this camera are not square but rectangular in shape. Hence the resultant image is also rectangular. This is made to square image by image processing and central 16 by 16 lenslet images are chosen for computations. The square image obtained after processing is shown in Fig 9.6. This image corresponds to the condition when zero volt is applied to all the actuators. Next, the DAC input number is increased by 10 (Hex) and the corresponding voltage produced by DAC is 0.237 V. The Shack-Hartmann lenslet array image is captured. Using image processing software, this image is converted into a square image and it is stored by the same procedure given above. This procedure is repeated till DAC number is FF (Hex). The first image where zero volt is applied to all actuator is taken as a reference image and images taken with

other set of constant voltages to all actuators are treated as aberrated images. Zernike polynomials are computed for the reference image and one aberrated image. Table 9.3 gives the computed coefficients of the Zernike polynomial obtained from the set of data for voltages applied in increasing order to all actuators. The software can compute Zernike coefficients upto any desired degree just by adding corresponding terms in the computation. The very low value of the coefficients for DAC voltage of 0.469V, which corresponds to 27.7V to all actuators, indicates DM is close to a flat surface. Similar results were obtained using LTP. Further increase of voltage produced appreciable change in Z4 value.

DAC V	Z1 Y tilt	Z2 X tilt	Z3 Astigmat	Z4 Defocus	Z5 Astig (90)
0.237	-0.0707	0.0775	0.0021	-0.0016	0.0045
0.469	-0.0699	0.0648	0.0060	0.00057	0.0044
0.932	-0.0912		0.0026	0.0085	0.0055
1.005				0.0131	
1.164				0.0191	
1.236				0.0205	
1.395				0.0281	
1.858				0.0531	
2.321				0.0816	
2.785				0.1257	
3.248				0.1277	
3.697				0.1301	

DAC V	Z6 Triang. Astig	Z7 3 <sup>rd</sup> coma	Z8 Y Coma	Z9 Astig
0.237	0.000037	0.0012	0.0021	0.0001
0.469	0.000259	0.0013	0.0016	-0.0011
0.932	0.0017	0.0008	0.0021	0.00001

*Table 9.3 First 9 Zernike coefficients (Z1 to Z9) for different DAC voltages. Empty cells values are close to zero.*

The calculation of Zernike coefficient in Table 9.3 have been obtained after optimizing the light level for the SH sensor and choosing appropriate range of voltage to the actuators of DM within the permissible limits worked out separately.

Following linear relationship between constant applied voltage to the actuators

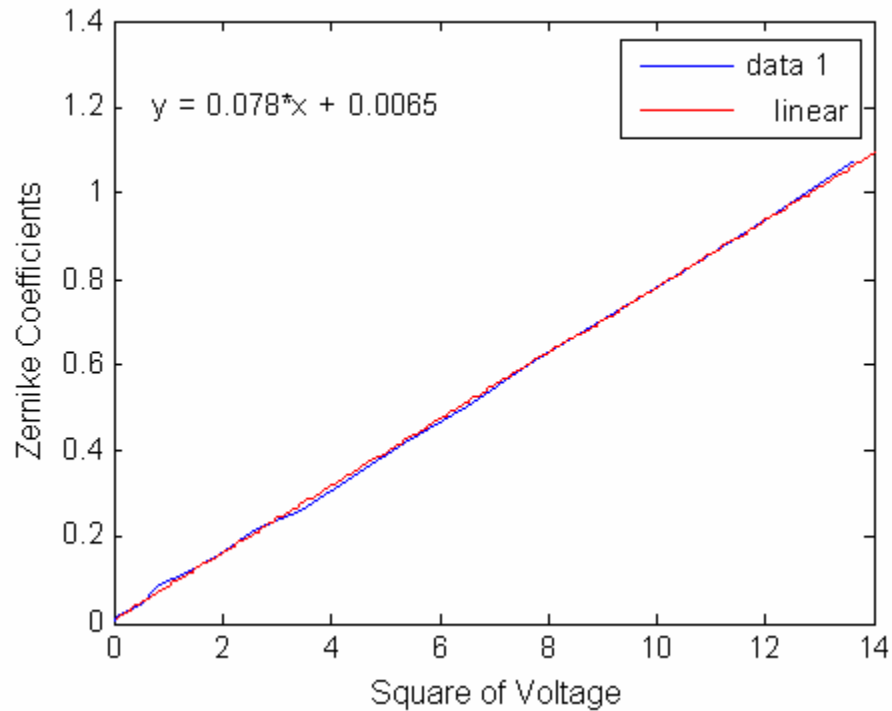


*Fig. 9.7 Relation between Z4 coefficient and square of the applied voltage.*

and variation of Z4 was used for close loop corrections  $Z4 = 0.078V^2 + 0.0065$

Figure 9.7 shows the validity of the equation.

#### **9.4 Tilt and Deformable Mirror correction results**

Using the calibration results so obtained from Table 9.2 and 9.3 a close loop correction for an aberrated image produced by the telescope system in autocollimation mode was carried out. Different stages of correction are shown in Fig.9.8 to Fig.9.12 in terms of their wavefront plot. Figure 9.13 shows the actual corrected image.

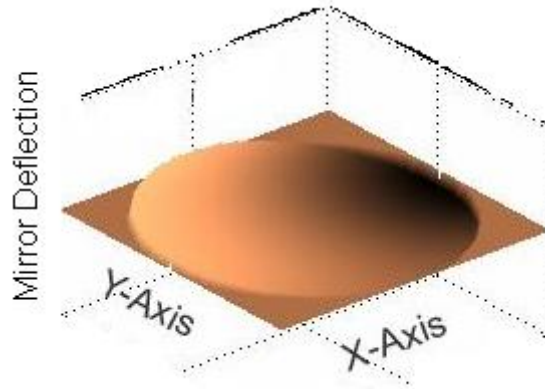


*Fig.9.8 3-D view showing aberrations as measured by Shack-Hartmann sensor.*

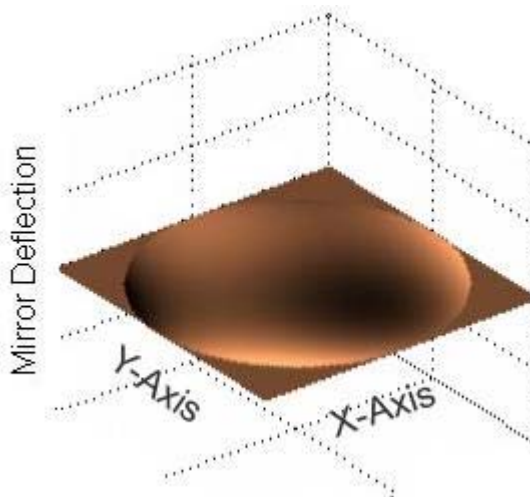


*Fig 9.9 3-D view of the surface after tip x and y tilt errors removed*

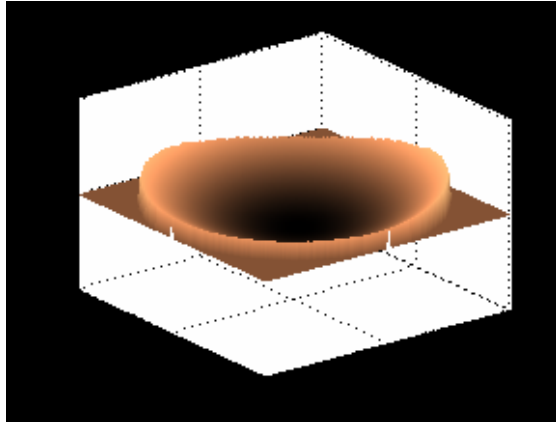


*Fig. 9.10 DM takes parabolic shape for equal voltage applies to actauators. 3-D Slant view of DM*

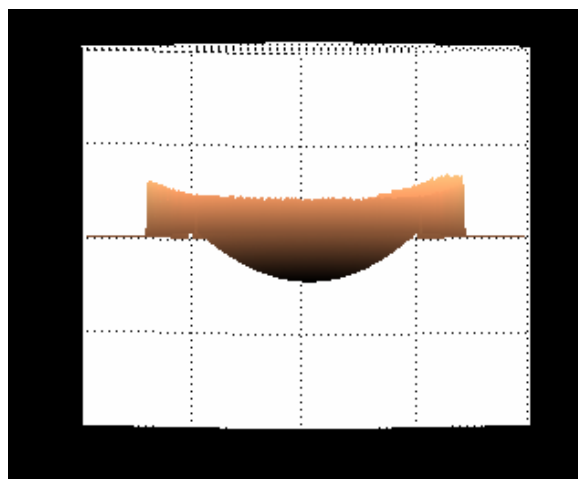


*Fig. 9.11 Shape of the mirror when 112 V is applied to all actuators of the mirror*

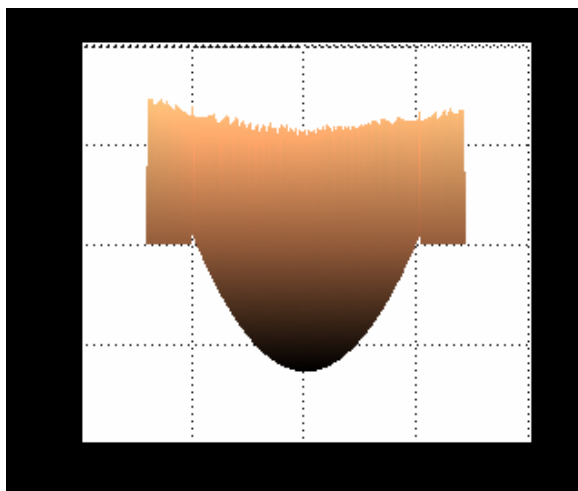


*Fig 9.12 Shape of the mirror for input voltage of 215 V is applied to all actuator of the mirror. Fig. 9.11 and 9.12 are in the front elevation of the 3-d view*

The first three zernike terms before and after correction are

	<b>Before correction</b>	<b>After correction</b>
Z1	0.3140	0.0473
Z2	0.5270	0.0454
Z3	0.0110	0.0132

*Table 9.4 First three zernike coefficients before and after correction*

Figs. 9.10, 9.11 and 9.12 show the control of deformable mirror Zernike coefficient Z4. The depth of focus can be achieved by varying voltages to the actuators from 112 V to 210 V. The incoming wave-front had tilt and defocus errors only, which can be easily generated by the optical components. The Shack-Hartmann wave-front camera has measured the wave-front and the correction was given based on the calibrations done earlier.

**Zernike coefficients for Z4, Z5 and Z6**

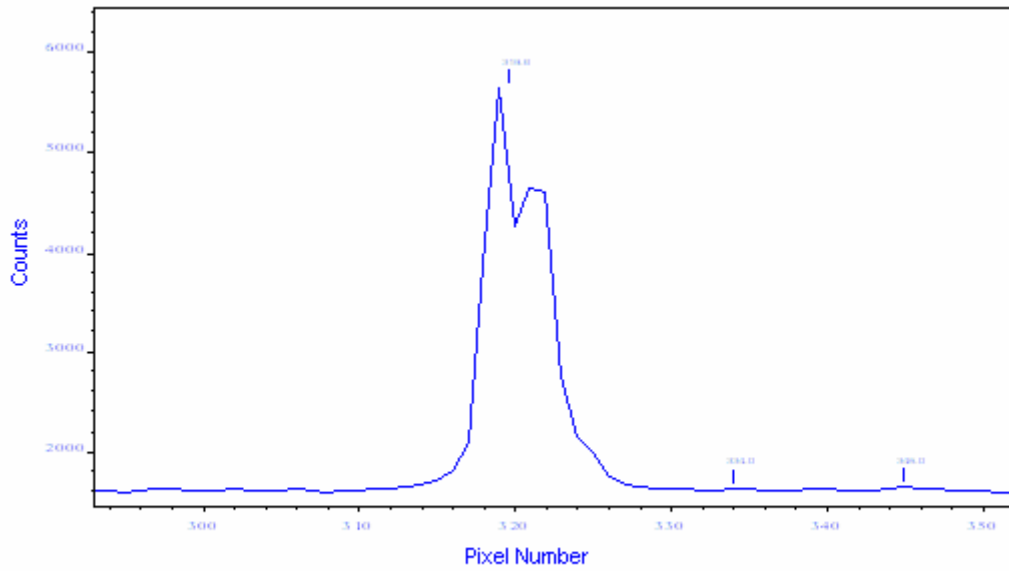
	<b>Before correction</b>	<b>After correction</b>
C4	-0.1407	-0.065
C5	-0.0028	-0.0008
C6	0.0097	0.0034

*Table 9.5 Zernike coefficients C4, C5 and C6 before and after correction*

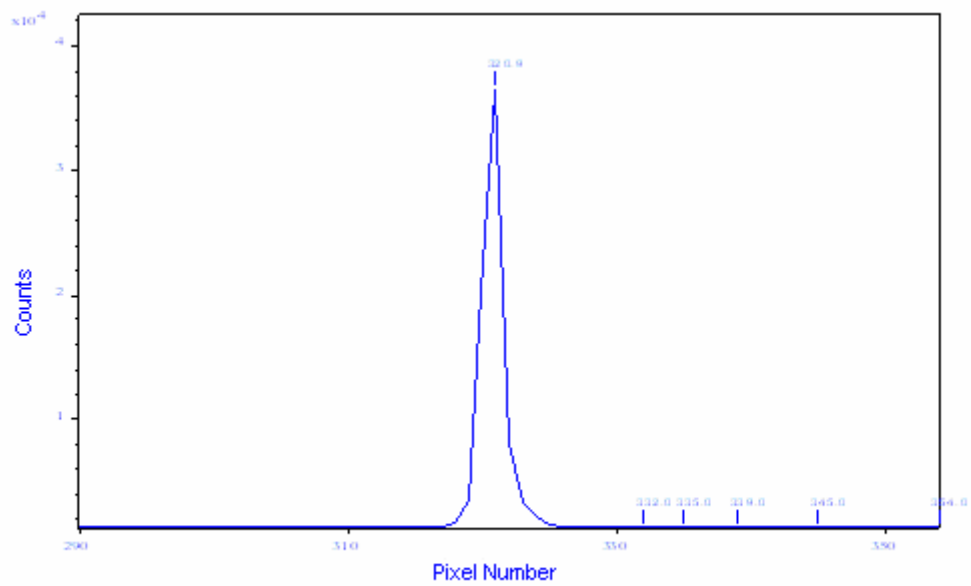
**9.10 Examples of corrections and image improvement**



*Fig. 9.13 Image captured by Andor CCD camera with 10 msec exposure time. Left: uncorrected image. Right: Corrected image (Twice magnified)*



(a)



(b)

*Fig. 9.14 Plot of horizontal cut across the image*  
*a): Uncorrected image      b): Corrected Image*

The maximum intensity for uncorrected image is 5610 counts. For corrected image it is 36500 counts. The Full Width at Half the Maximum (FWHM) for top image is 6.4 pixels and for the corrected image at the bottom, it is 3.5 pixels.

### 9.11 Discussion of the results

The Zernike coefficients before and after correction are listed in the table 9.3, it can be seen that the major error is in the Zernike coefficient 4 ( $z_4$ ). It is imperative from the table that the membrane deformable mirror is able to correct the errors very efficiently more so for circularly symmetric errors. Using this kind of calibration method and generating look-up tables and relationship between different coefficients and actuator voltage, the correction cycle can be highly speeded up to achieve fast close loop correction system.

At present, the errors in the wave-front were generated by changing system parameters in the collimator.

## Chapter 10

### Summary and Remarks

The main aim of the research work is to understand the contribution of atmospheric disturbance on astronomical imaging and devise a method to characterize it for a telescope location and develop low cost technological solutions (81) to take adaptive corrective action so that the effects of atmospheric disturbance can be eliminated to achieve close to diffraction limited imaging. Detailed theoretical study and laboratory experiments were conducted to achieve the said goal.

Survey of literature and our own investigation of atmospheric seeing show that normally seeing is in sub arc seconds range, which is otherwise marred by local atmospheric effects and system errors. The major contributor for seeing in the path of object and telescope is an atmospheric layer at about 8 to 10 Km. height and the seeing contribution from this layer is about 0.3 arc-second at visual wavelengths.

Atmospheric seeing is characterized by Fried's parameter  $r_0$ . A new approach has been demonstrated to measure  $r_0$  at visual wave length using speckle interferometry method at the Vainu Bappu Telescope (VBT), Kavalur. This approach has been adopted for the first time. The measured  $r_0$  value varied from 10 to 15 cm and no extreme variations are noticed outside this range. In the above range of  $r_0$ , seeing varies at short intervals of about 15 to 20 millisecond. Any correction system design need to take this factor into consideration.

An optical system design was carried out for wave-front error measurement and correction experiments for the VBT. Zeemax optical design package was used for this purpose. A simplified design has been worked out using fewer components keeping the cost factor to a minimum.

Most important and crucial requirement in terms of wave-front sensing and AO system design is a fast wave-front digital image acquisition, analysis and fast correction. Custom made CCDs with high frame rates are expensive and not

readily available. Therefore, use of CMOS imagers for the purpose has been investigated as a low cost solution. Because CMOS imagers are essentially single chip cameras, these are available at much lower cost than CCDs. The random access of pixels can be used to advantage, to read only the required area of the device. In the present work, suitable software and algorithm have been developed to acquire images at real time rate.

The only drawback noticed with this CMOS imager is the 8 bit analog to digital converters built into the CMOS imager which is found to be inadequate. Also, 15 % of the pixel only is light sensitive and remaining 85 % of the pixel area is occupied by the electronic circuits of the camera giving diffraction effects and corresponding noise. This noise cannot be removed by cooling the device. For these reasons, algorithms were developed to find out centroids, slopes and Zernike polynomial from noisy data thus making CMOS imager suitable for low cost application in wave-front sensing.

High frame rate CCDs are increasingly being used in wave-front sensing applications. Peltier cooled, Low light level CCD camera, with an integration time of 10 msec and 16 bit digitization was also used in the new wave-front sensor. For very faint light sources like stars, this camera gives appreciable signal at short integration time using electron multiplying technique. The software selection of the gain is highly useful to get required signal level with varying integration time.

In most wave-front sensing algorithms, Zernike polynomial computations are conventionally done in polar coordinates for wave-front error calculations. As the lenslet arrays are distributed in square grid form, computations performed in Cartesian coordinates for circular apertures resulted in saving of computation time. The maximum sub aperture tilt in the wave-front sensor is limited by the sub-aperture area of each lenslet. The new algorithm searches for circular or elliptical objects in the image formed by the lenslet array without any limitation of the sub aperture. Further, the accuracy of the centroid calculations and hence, the accuracy of wave-front error computation has significantly improved because

of only area containing the image formed by lenslet is used for centroid computation.

For wave-front correction, the tip-tilt and deformable mirrors are imperative requirements. Standard, available technology for the image motion correction using tip-tilt mirror forms a convenient choice. The Shack-Hartman wave-front sensor built for this purpose gave accurate results in measuring the wave-front tilts, and higher order aberrations like defocus, coma, etc. Tilts of micro radian range were measured using the calibration setup. Measurements show that the tip tilt mirror used in this work has hysteresis. Calibration setup has measured the hysteresis of the piezoelectric actuators and compensation is done by controlling the tilt mirror. Tilts of the incident wave-front were successfully measured and corrected using the calibration data.

Attempts were specially made to select a suitable deformable mirror for wave-front correction. As a low cost solution, micro electro mechanical system (MEMS) based membrane mirror available in the market was chosen for this study. The top of the membrane is coated with gold, to make it reflective and conductive. The 37 actuators are hexagonal patterns of about 1.75 mm size, etched on a printed circuit board (PCB), arranged within a circle of about 12 mm. The membrane mirror is mounted over the PCB with a spacer. Voltages are applied between the conductive top of the membrane and different actuator pattern. The electrostatic force formed between the mirror top and the actuator pulls the membrane mirror towards the PCB in the air gap between them. By controlling the magnitude of the voltages applied to the actuators, any desired mirror shapes can be created. There are 37 degrees of freedom for mirror control.

To understand the characteristics and behaviour of the mirror, finite element analysis (FEA) and a direct profile measurement using the in-house developed Long Trace Profilometer (LTP) were performed. FEA method was unable to provide any realistic performance characterization. Measurement through LTP was more accurate and resulted in true representation of the DM characteristics. The foot print of the actuator which is 1.75 mm is clearly seen on

the surface created on the mirror, hence correction of features less than this diameter may be difficult. It is observed that only smooth surfaces are generated by the mirror; hence it can be best suited for correcting lower order aberrations only.

The 37 actuator deformable mirror was also tested and calibrated with the newly built Shack-Hartmann wave-front sensor. The deformable mirror had certain aberrations when no voltages were applied to the actuators. It could be made flat by applying 51.4 V and 27.4V for two mirrors respectively used in the studies, to all actuators. This condition is equivalent to applying an electrical bias to the mirror. No hysteresis was observed in the mirror during increasing and decreasing of the voltages applied to the actuators. Calibration results showed that the mirror performance is well predictable and could be easily fitted to a theoretical formulation.

Though the optical design for the AO configuration for VBT was done for future implementation, a laboratory set up was built to test the applicability and the performance of the hardware and software developed in the present context. Most of the improvement in the image can be brought by correcting lower order (primary aberrations) errors.

A closed loop correction was tried out using the reported Lab-setup. Present experiment demonstrates the successful implementation of the new approach and system hardware and software. Its potential application into an actual telescope system need to be exploited.

In the present development, only limitation has been the closed loop cycle correction time which could be improved by incorporating high end processor hardware with parallel processing capability. This is a part of our future program.

All the development brought out through this work will be used to incorporate a closed loop real time adaptive optics system in our 2.34 M VBT at Kavalur.

## References

- 1 High Resolution imaging from the ground  
N. J. Woolf. Annual review of Astron. Astrophys. 1982, 20:367-98
- 2 Newton I 1730 Opticks Bk 1 Pt 1 Prop 8  
Reprinted, 1952, New York, Dover, 406 pp
- 3 The possibility of compensating astronomical seeing  
W. W. Babcock  
Publication of astronomical society of the Pacific, 1953, Oct, Vol. 65,  
No. 386, 229
- 4 Adaptive optics and ground-to-space laser communication  
Robert K. Tyson, Applied Optics, 1996, July, Vol. 35, No 19, 3641
- 5 Preliminary results of an Instrument for measuring the optical aberrations  
of the human eye  
Luis Alberto V. de Carvalho and Jarbas Caiado de Castro,  
Brazilian Journal of Physics, 2003, March, Vol. 33, No 1, 140
- 6 Adaptive mirror micro machined in silicon,  
G. V. Vdovin, Ph. D. Thesis, Delft University of technology, 1996,  
The Netherlands
- 7 Limiting resolution looking down through the atmosphere  
D. L. Fried, Journal of the optical society of America, 1966, October,  
Vol. 56, No. 10, 1380-1384
- 8 Stellar interferometry methods.  
Antoine Labeyrie, Annual Rev. Astro. Astrophys. 1978, 16: 77-102
- 9 Optical propagation and image formation through the turbulent  
atmosphere  
F. Roddier, Diffraction limited imaging with Very Large Telescopes  
D.M. Alloin and J.M. Mariotti (Editors), 1989, Kluwer Academic Publishers

- 10 Outer scale of turbulence appropriate to modeling refractive index structure profiles  
C. E. Coulman, J. Vernin, Y. Coqueugniot and J. L. Caccia  
Applied Optics, 1998, 27, 155 -160
- 11 Path length stability of synthetic aperture telescopes. The case of 25 cm. Cerga interferometer.  
J. M. Mariotti and G. P. Di Benedetto.  
Proceedings of International Astronomical union Colloquium 79,  
European Southern Observatory, 257-265
- 12 Atmospheric turbulence and the resolution limits of large ground-based telescopes  
T. Stewart McKechnie, Journal of Optical Society of America, 1992, November, Vol. 9, No 11, 1937
- 13 Atmospheric turbulence and the resolution limits of large ground-based telescopes - comment  
V.I. Tararski and V U. Zavorotny, Journal of Optical Society of America 1993, 11 November , A 2411, Vol. 10, No (A-7) 3, 2415
- 14 Image quality tip-tilt correction and shift and add infrared imaging  
J. C. Christu , Publication of the Astronomical Society of Pacific,  
1991, September, 103:1040 -1048
- 15 Atmospheric turbulence and the resolution limits of large ground-based telescopes: Reply to comment  
Stewart McKechnie, Journal of optical society of America,  
1993, November, Vol. 10, No. 11, 2415
- 16 Temporal Fluctuations of Atmospheric Seeing  
Rene Racine, Pub. Astron. Soc Pacific, 1996 , April ,108: 372-374,
- 17 Antarctic site testing - micro thermal measurements of surface-layer seeing at the South Pole  
R. D.Marks, J. Vernin, M. Azouit, et.al. Astronomy and Astrophysics Supp. Series, 1996, 118, 385-390
- 18 Micro thermal measurements of surface layer seeing at Devasthal site

- P. Pant, C. S. Stalin and Ram Sagar  
Astronomy and Astrophysics, 1998, No.12
- 19 Optical Seeing at La Palma Observatory  
J. Vernin and C. Munoz-Tunon, Astronomy and Astrophysics,  
1992, 257, 811-816,
- 20 Measurement of optical seeing on the high Antarctic plateau  
R. D. Marks, J. Vernin, et. al., Astronomy and astrophysics Suppl. Ser.  
1999, 134, 161 -172
- 21 Newcasting Astronomical Seeing: Towards an operation approach  
Fionn Murtagh, Alex Aussem and Marc Sarazin  
Pub. Astro. Soc. Pac. 1995, July, 107, 702-707
- 22 A. Aussem, Ph. D. Thesis, Universite' Paris V, Paris, France
- 23 Image motion as a measure of seeing quality  
H. M. Martin, Pub. Astron. Soc. Pacific. 1987, December, 99, 1360-1370.
- 24 Effects on seeing at the Anglo-Australian Telescope of Temperature  
Differences between Outside Air, Dome Air and Mirror  
P. R. Wood and S. G. Ryan  
Publication of Astronomical Society of Australia 1995, 12, 95-96
- 25 Image quality improvement at Vainu Bappu Telescope  
P. Shastri, An internal report, December 1998,  
Indian Institute of Astrophysics, Bangalore
- 26 Mirror, Dome and Natural seeing at CFHT  
Rene Racine, Derrick Salmon et.al, Pub. Astro. Soc. Pacific,  
1991, Sept. 103: 1020 -1032
- 27 Intensified CCD based remote guiding and Observation of speckles at  
Vainu Bappu Telescope  
V. Chinnappan, S. K. Saha, Faseehana,  
Kodaikanal Observatory Bulletin, 1991, 11, 87
- 28 Optical Resolution through a randomly inhomogeneous medium for very  
long and very short exposures  
D. L. Fried, Jour. Opt. Soc. Amer. 1966, Vol. 56, No.10, 1372

- 29 Performance evaluation of high-speed camera system for adaptive optics  
V. Chinnappan, A. K. Saxena, A. Sreenivasan  
Bull. Astro. Soc. India, 2002, 30, 815-817
- 30 Speckle Observations with a Photon Counting detector  
P. R. Wood Proc. Astro. Soc. Australia, 1985, 6(2), 120
- 31 Night time variations of Fried's parameter at VBT Kavalur  
S. K. Saha and V. Chinnappan,  
Bull. Astron. Soc. India, 1998, 26
- 32 Development of a speckle interferometer and the measurement of  
Fried's parameter  $r_0$  at the telescope site  
S. K. Saha, G. Sudheendra, A. Umesh Chandra, V. Chinnappan  
Experimental astronomy, 1999, 9, 39-49
- 33 WIYN Active Optics - A platform for AO  
A. D. Code and D. G. Sawyer, SPIE Conference, Hawaii, 1998
- 34 High-speed tilt mirror for image stabilization  
Jaime R. Taylor, Mathew S. Anderson and Patrick H. Bunton  
Applied Optics, 1999, January, Vol. 38, No.1, 219 -223
- 35 Electronics  
Trudy E. Bell, Senior editor, IEEE Spectrum, August 1995
- 36 Workshop on Extremely Large Telescopes,  
Backaskog, Sweden, 1999, June 1-2
- 37 Improving the throughput of telescope by adaptive optics methods  
V. Chinnappan, A. K. Saxena, A. Sreenivasan  
Bulletin of Astronomical Society of India, 1998, 26, 371-375
- 38 Adaptive optics: Neural Network wave-front sensing, reconstruction and  
prediction  
P.C. McGuire, D.G. Sandler, Michael Lloyd-Hart and Troy A. Rhoadarmer  
University of Arizona, USA, Reprint
- 39 Optical propagation and image formation through the turbulent  
atmosphere  
F. Roddier, Diffraction limited imaging with very large telescopes, 1989

- 33-52, Editors: D.M.Alloin and J.M.Mariotti, Kluwer Academic Publishers
- 40 Bandwidth specification for adaptive optics system  
D. Greenwood, Jour. Opt. Soc Amer. 1976, 66,193-206
- 41 Zernike polynomials and atmospheric turbulence  
Robert J. Noll, Jour. Opt. Soc. Amer., 1976, 66, 207
- 42 Optical shop testing,  
D. Malacara, 2<sup>nd</sup> edition , Wiley, New York ,1992, pp 461-466
- 43 Zernike annular polynomials and optical aberrations of system with  
annular pupils,  
V. M. Mahajan, Photo. News, 5, Engineering Lab Notes, 1994
- 44 History and principles of Shack-Hartmann wave-front sensing  
B. C. Platt, Ronald Shack. Journal of refractive surgery,  
2001, Vol.17, s573
- 45 Principles of adaptive optics  
Robert K Tyson, Academic Press, New York, 1991
- 46 Variation of Hartmann theme  
F. Roddier. Optical Engineering, October 1990, Vol. 29, 10, 1239
- 47 Theoretical fringe profiles with crossed Babinet compensators in testing  
concave aspheric surfaces.  
A. K. Saxena , J. P. Lancelot,  
Appl. Opt., 1982, 21, 4030
- 48 A new polarization shearing interferometer based Long Trace Profilometer  
A. K. Saxena, V. C. Sahani, R. Mukund and R. Ismail Jabilulah  
Second International workshop on metrology for X-ray optics,  
CSR, Grenoble, France (2004)
- 49 Wave-front sensing for adaptive optics.  
A. K. Saxena, J. P. Lancelot and V. Chinnappan.  
International conference on Optics and Opto-electronics  
Defense Research and Development Organization, Dehra-Dun, India  
December-1998

- 50 Adaptive optics development at Indian Institute of Astrophysics.  
A. K. Saxena, V. Chinnappan and A. Sreenivasan.  
International conference on optics and opto-electronics  
Defense Research and Development Organization,  
Dehra- Dun, India, December, 1998.
- 51 An Interferometric Hartmann wave-front analyser for the 6.5 m MMT  
S. C. West, S. Callahan, D. Fisher,  
MMTO Technical Report #37, University of Arizona, USA
- 52 Use of a neural network to control an adaptive optics system for an  
astronomical telescope  
D. G. Sandler T. K. Barrett, D. A. Palmer et.al,  
Nature, 1991, May, 330, Vol. 351 23
- 53 Sensitivity of a pyramidic wave-front sensor in closed loop adaptive optics  
R. Ragazzoni and J. Farinato (1999)  
Astronomy and Astrophysics 350: L23-L26
- 54 Design and development of Mosaic CCD controller  
B. Nagaraja Naidu  
Ph. D. Thesis, Indian Institute of Astrophysics, Bangalore, India
- 55 Optical limitations to cell size reduction in IT-CCD Image sensors  
Takashi Satoh, Nobuhiko, Mutoh, et.al.,  
IEEE transactions on electron devices, 1997, October, Vol. 44, No.10,  
1599-1603
- 56 Laboratory adaptive optics system for testing the wave-front sensor for  
new MMT,  
T. A. Rhoadarmer, P. C. McGuire, J. M. Hughes, et, al.,  
University of Arizona, USA
- 57 Cold finger type liquid nitrogen cooled CCD cryostat for astronomical  
telescopes.  
S. Jacob, S. Kasturirangan, R. Karunanidhi, R. Srinivasan, V. Chinnappan  
and G. Srinivasulu, Journal of Instrument Society of India, 1995

- 58 Smart CMOS Image Sensor Arrays  
Michael Schanz, Werner Brockhherde, Ralf Hauschild  
IEEE transactions on electron devices, 1997, Oct, Vol. 44, No. 10, 1699
- 59 CMOS image sensors: Electronic camera on a chip  
Eric R fossum. IEEE transactions on electron devices,  
1997, Vol. 44, No 10, 1689 -1698
- 60 Performance evaluation of high-speed camera system for adaptive optics.  
V. Chinnappan, A. K. Saxena, A. Sreenivasan  
Bull. Astr. Soc. India, 2002, 30, 815
- 61 A CCD based curvature wave-front sensor for adaptive optics in  
astronomy  
Reinhold Josef Dorn, Ph.D. Thesis, 2001  
Ruperto-Carola university of Heidelberg, Germany
- 62 A simple low-order adaptive optics system for near-infrared applications  
Francois Roddier, Malcolm Northcott and J. Elan G. Raves  
Pub. Astron. Soc. Of Pacific, 1991, Jan, 130-149
- 63 Fuga 15 D data sheet, C-Cam Technologies, Netherlands
- 64 Real-time distributed processing in the Mt. Wilson 100-inch Hooker  
telescope adaptive optics system  
T. G. Schneider  
<http://www.mtwilson.edu/~tgs/papers/rtdist/rtdist1.html>
- 65 Private communication, Roper Scientific, USA
- 66 Design and implementation of CMOS imager based Wave-front Sensor for  
adaptive optics.  
V. Chinnappan, A. K. Saxena, A. Sreenivasan.  
Astronomical Society of India meeting,  
Thiruvananthapuram, Kerala, February 2003.
- 67 Andor CCD user's Manual, Andor technology Ltd. U.K.
- 68 High-precision analysis of a lateral shearing interferogram by use of the  
integration method and polynomials  
Seiichi Okuda, Takashi Nomura, Kazuhide Kamiya, et, al.,

- Applied Optics, 2000, October, Vol. 39, No. 28
- 69 Low-cost Bimorph Mirrors in Adaptive Optics  
Edric Mark Ellis, Ph.D. Thesis, 1999, University of London, UK
- 70 Development of micro electro mechanical deformable mirrors for phase modulation of light  
Raji Krishnamurthy Mali, Thomas G. Bifano, Newsman Vandelli and M. N. Horenstein  
Optical Engineering, 1997, October, 36(2), 542-548, 1731
- 71 Adaptive optic correction using micro electro mechanical deformable mirrors  
Julie A. Perreault, Thomas G. Bifano, B. Martin Levine and Mark N. Horenstein, Optical Engineering, 2002, March, 41(3), 561-566,
- 72 37 – channel micromachined deformable mirror system: technical passport, OKO Technologies, Reinier de Graafweg, 2625 D J Delft, The Netherlands
- 73 Characterization of adaptive optics mirrors using long trace profilometer  
A. K. Saxena, V. Chinnappan and Ismail Jabilullah  
Asian journal of physics, 2004, Vol. 13, no 3&4, 205-214
- 74 Report - Finite Element Analysis of Flexible Mirror  
Central Manufacturing Technology Institute, Bangalore-22
- 75 Optimization-based operation of micro machined deformable mirrors  
Gleb Vdovin, SPIE Conference on Adaptive Optics Systems Technologies, Kona, Hawaii, March 1998.
- 76 Taking the twinkle out of the stars: An adaptive wave-front tilt correction servo and preliminary seeing study for SUSI  
Theo ten Brummelarr. Ph.D. Thesis, University of Sydney, Australia
- 77 Adaptive control of a micromachined continuous-membrane deformable mirror for aberration compensation  
Lijun Zhu, Pang-Chen Sun, Dirk-Uwe Bartsch, et., al.  
Applied Optics, 1999, January, Vol. 38, No. 1, 168
- 78 Model of an adaptive optical system controlled by a neural network

- G. Vdovin, *Optical Engineering*, 1997, 36, 1354 – 1360.
- 79 Computation of static shapes and voltages for micromachined deformable mirrors with nonlinear electrostatic actuators  
P. K. C. Wang and F. Y. Hadaegh  
*Jour. Microelectromech. System*, 1996, 5, 205 - 220
- 80 Improving the resolution of ground-based telescopes  
M.C. Roggemann, B. M. Welsh, R. Q. Fugate  
*Review of Modern Physics*, 1997, April, Vol. 69, No. 2
- 81 Low cost adaptive optics for astronomical applications  
V. Chinnappan, A. K. Saxena, A. Sreenivasan  
*Proceedings of SPIE*, 2001, Vol. 4417, 563
- 82 An Interferometric Hartmann wavefront analyzer for the 6.5 m MMT and the first results for collimation and figure correction  
S. C. West, S. Callahan, D. Fisher, *MMTO Technical Report #37*,  
University of Arizona, USA

## Appendix A

### Flow Chart of the program

The program does the following major tasks

- Get the PCI address of CMOS imager controller
- Set up the registers of PCI card
- Zero 1 to 40 channels of DACs to 0 volts in the digital interface card
- Get the region of interest parameter for the image to be acquired, ADC delay etc from user
- Set up memory buffer for image
- Get no. of Zernike coefficients to be found, no of lenslet images
- Read an image
- Identify objects of interest like circular, square with control parameters
- Compute x and y centroids of identified objects in reference image
- Read aberrated image
- Identify objects of interest like circular, square with control parameters
- Compute x and y centroids of identified objects in the aberrated image
- Calculate the difference in centroid of x and y which represent slope values
- Arrange them into matrix form
- Arrange 2 dim matrix of slope values into a column vector
- Normalize to a unit circle and mask out the outside edges
- Calculate Zernike monomial matrix which contains derivative values of each monomial at reference points
- Calculate Zernike coefficients to the required nos with least square polynomial fit
- Calculate RMS error in polynomial fit

- Calculate wavefront phase data from Zernike polynomials
  - Mask it to unit circle
  - Display the wave-front
  - Check Zernike coefficients 1 and 2 are above threshold value, If less skip the next two steps
  - Compute Actuator DAC voltages and the required DAC nos from calibration data
  - Output the DAC values
  - Check Zernike coefficients  $z_3$  to  $Z_n$  for threshold, If less, goto last step
  - Calculate dac volt and dac nos from calibrated values
  - Output the voltage
  - Goto grab the image and repeat.
- 
- Flow chart for some important functions are given below

